



University of Innsbruck
Institute for Astro- and Particle Physics

MHD simulations of colliding stellar winds in binary systems

Master's Thesis in Astrophysics

Anna Ogorzałek

Submitted to the
Faculty of Mathematics, Computer Science and Physics
in Partial Fulfillment of the Requirements for the Degree of
Magister / Magistra der Naturwissenschaften

Supervisor:
Dr Ralf Kissmann

Innsbruck, August 2014

Abstract: Massive binary systems are sources of non-thermal radiation and possibly even γ -rays. This high energy emission originates in the region between the two stars, where their powerful winds collide. This region possess extreme physical conditions that have been the subject of multiple studies including hydrodynamical and particle acceleration simulations. There is little known about the magnetic field at the collision region. It is an important factor, since it produces the non-thermal synchrotron emission, as well as influences the particle acceleration. In this work we use 3D magnetohydrodynamical simulations in order to study the magnetic field properties in the collision region, in particular its strength and the geometry (the angle between the field lines and the shock normal). We prescribe a dipolar magnetic field for both stars and perform a parameter study of its strength and geometry. We conclude that for the studied range of dipol strengths ($\sim 100\text{G}$) no influence on the collision region is found, as it retains its shape and shocks compression ratios. The magnetospheres do not cross the contact discontinuity, and the respective sides of the collision region depend only on the stellar fields. However, this means that prescribing a single field strength over the whole collision region might not be sensible. We also find that changing the geometry of the stellar surface fields changes the quasi-parallel/perpendicular structure of the shocks as well as introduces even more complicated structure of the magnetic field strength in the collision region. Our simulations hint that the stronger magnetic fields than we were able to use can have a large effect on the properties of the collision region, especially its geometry.

Contents

| | |
|---|-----------|
| Introduction | 1 |
| 1 Stellar winds | 3 |
| 1.1 Solar wind | 3 |
| 1.2 The Parker wind model | 4 |
| 1.3 Line-driven winds | 8 |
| 1.3.1 A few simple estimates | 8 |
| 1.3.2 The CAK approximation | 13 |
| 2 Massive stars | 21 |
| 2.1 Physical properties | 21 |
| 2.2 Magnetic fields | 23 |
| 2.2.1 Observational evidence | 23 |
| 2.2.2 Magnetic fields, rotation and the winds | 24 |
| 3 Colliding Wind Binaries | 31 |
| 3.1 Wind collision region structure | 31 |
| 3.2 Observations of colliding winds | 34 |
| 3.3 Hydrodynamical models | 37 |
| 3.4 Shocks and particle acceleration | 37 |
| 4 Modeling | 43 |
| 4.1 The code | 43 |
| 4.2 The setup | 45 |
| 5 Results - single simulations | 49 |
| 5.1 Simulations of a single massive star | 49 |
| 5.2 An exemplary simulation of the CWB system | 54 |
| 5.3 Analysis of the collision region | 54 |
| 6 Results - a parameter study | 71 |
| 6.1 Variation of the magnetic field strength | 71 |
| 6.2 Variation of the field geometry | 72 |
| 6.3 High magnetic fields | 75 |
| 7 Conclusions | 85 |
| 7.1 Future work | 86 |

Acknowledgments

87

Bibliography

89

Introduction

The binary systems composed of massive stars (O, B, WR) are the subject of many studies focusing on their non-thermal emission and possible particle acceleration (e.g. [Pittard & Dougherty, 2006](#)). They produce strong plasma outflows that collide with each other, creating a region of extreme physical properties contained within two shock surfaces, which is believed to be the source of the observed high energy emission. Many hydrodynamical simulations have been employed to explain the non-thermal radiation and to study the particle acceleration taking place in the shocks of the collision region (e.g. [Pittard, 2009](#); [Reitberger et al., 2014b](#)).

The magnetic field is an important component of the colliding wind binaries, especially with regard to the high energy processes. Firstly, it is essential in the production of the observed synchrotron radiation and synchrotron losses of high energy electrons. Secondly, it influences the particle acceleration capabilities of the two shock surfaces. Current studies of particle accelerations in these systems use very simplified magnetic field strength in the collision region, usually following [Eichler & Usov \(1993\)](#). They also do not take into account possible variations in the angle between the shock normal and the magnetic field, which is one of the parameters governing the efficiency particle acceleration.

In this work we present our attempt at full, magnetohydrodynamical simulations of such systems. We want to better describe the magnetic field's properties in the collision region and understand its influence on the whole system and the possible effects on particle acceleration. To that end we employ the 3D MHD code CRONOS and study the parameter space of the field strength and its orientation with respect to the collision region.

The work is organized in the following order:

- ∞ Chapter 1 lays out the basic theory of stellar winds, with emphasis on the physical processes that are responsible for the acceleration of the winds in the colliding wind binaries.
- ∞ Chapter 2 summarizes the basic physical properties of the massive stars and the current state of knowledge on their magnetic fields, commenting on theory as well as observations and modeling.
- ∞ Chapter 3 describes in detail the binary systems we are interested in, in particular the structure of the wind collision region, the observations and simulations of colliding winds. It also gives a short outlook on the particle acceleration capabilities of the collision region shocks and their possible dependence on the magnetic field orientation.
- ∞ Chapter 4 introduces the numerical scheme we employ in our study and details the way in which we prescribe the setup of our simulations.

- ∞ Chapter 5 presents results of a few single simulations that give an insight to the properties of the simulated systems and the physical quantities that can be derived, outlining our line of reasoning and analysis used.
- ∞ Chapter 6 presents a parameter study of varying magnetic field strengths and geometries.
- ∞ Chapter 7 summarizes briefly the most important results and gives an outlook on possible future work.

Let us remark that all values and equations are expressed in SI units unless specified otherwise. The values for specific magnetic inductions are expressed in Gauss units following common astrophysical convention. Bold symbols in equations denote vector quantities.

Stellar winds

Stellar wind is a phenomenon common to all main sequence stars, which differs depending on their type. It is a continuous outflow of mass that can lead to losses of about half the stellar mass in the case of the hot, massive stars or have little to no influence over star's evolution as it does for the low mass main sequence stars. Apart from mass, the wind can carry out angular momentum, frozen-in magnetic field and kinetic energy that it deposits in the interstellar medium. Measuring wind properties such as the mass-loss rate and the terminal velocity is helpful in distinguishing between different stellar evolutionary scenarios, as they yield different predictions for the winds. As one would expect, the basis for the theory of the driving mechanisms and stellar wind properties was brought about by studies of the solar wind in all accessible spectral regions. Here we shall discuss the basic mechanisms of pressure- and line-driven winds that are relevant to our study.

1.1 Solar wind

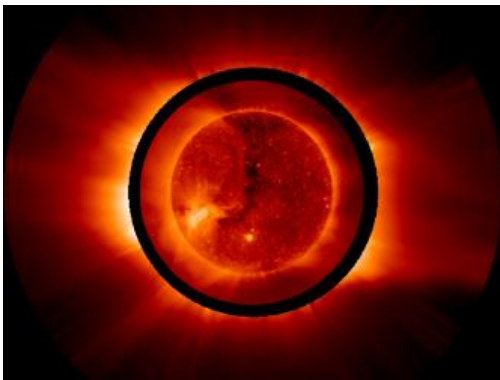


Figure 1.1: Solar wind as seen in the UV light emitted by ionized oxygen (outer region) and ionized iron (inner region). *Image credit: SOHO.*

It used to be believed that the space between planets and the Sun was empty. The first insight to the presence of some charged particle flow came from the aurora observations. In the 1950s scientists started to consider the presence of ionized gas in interplanetary space in order to explain the observations of ion tails of comets (Biermann et al., 1967). The first comprehensive solar wind model was proposed by Parker (1958) and is further discussed in section 1.2.

The current state of knowledge about the solar wind comes from in site observations made aboard spacecrafts. The wind plasma consists mostly of protons and electrons, and a few α particles; the respective abundances change in time

with solar activity. It has a temperature of the order of 10^5 K and velocities up to 2000 km/s, making it supersonic.

Observations put strong constraints on the possible wind model. It has to be able to accelerate the coronal gas from very small velocities near the Sun up to supersonic values at Earth's orbit, as well as reproduce the measured values of large density drop and slow decrease in temperature at the same time.

1.2 The Parker wind model

Now we will give an overview of the Parker's wind model. Therefore let us now consider a macroscopic fluid description of the gas in the wind. It consists of protons and electrons that are coupled with each other and have approximately the same velocity ($v_e = v_p = v$), meaning there are no currents in the wind. The same goes for temperature ($T_e = T_p = T$). As mentioned before, the temperature changes very slowly, hence it shall be considered constant. The plasma has no reason to carry any macroscopic charges, so the particle number densities are equal as well ($n_e = n_p = n$). We consider the steady state, spherically symmetric case which is fulfilled to a good approximation. This allows us to use spherical coordinates and assume that all quantities are functions of just the radius r . We are choosing the Lagrangian approach and follow a gas volume on which forces act via the equation of motion (Newton's law):

$$\frac{Dv}{Dt} = -\frac{GM}{r^2} - \frac{1}{\rho} \frac{dp}{dr}, \quad (1.1)$$

where v is the fluid velocity, M the mass of the star (Sun), p the thermal pressure and ρ the gas mass density. $\frac{D}{Dt} = \frac{\partial}{\partial t} + v\nabla_r$ stands for the convective derivative that accounts for acceleration caused by the change of the flow field in both time and space. The forces that are acting on a gas volume are the gravity from the star and the pressure gradient, we ignore the viscous forces and assume that the rotation of the star does not influence the wind. Note that in principle this is a vector equation that was reduced to a scalar one by our assumption of the spherical symmetry and the choice of coordinates ($\mathbf{v} = (v_r = v, 0, 0)$). The velocity field does not change in time (we are looking for steady state solutions; $\frac{\partial}{\partial t} = 0$), and in spherical coordinates the r -component of the gradient operator takes form of a simple radial derivative. Combined, this gives us the equation:

$$v \frac{dv}{dr} = -\frac{GM}{r^2} - \frac{1}{\rho} \frac{dp}{dr}. \quad (1.2)$$

We further assume the ideal gas law for the pressure: $p = p_e + p_p = 2nkT$ and express the mass density via the number density: $\varrho = (m_p + m_e)n = m_H n$ (m_H being the hydrogen mass), thus obtaining:

$$v \frac{dv}{dr} = -\frac{GM}{r^2} - \frac{2kT}{m_H} \frac{1}{n} \frac{dn}{dr}. \quad (1.3)$$

There are no additional sources or sinks of particles, hence we can apply the mass conservation equation, meaning that the mass loss rate through a spherical surface of radius r is constant (as well as the number of particles crossing through that surface):

$$\dot{M} = 4\pi r^2 \varrho v = \text{const} \Leftrightarrow r^2 n v = \text{const}. \quad (1.4)$$

Taking the derivative with respect to r we get a relation between the number density and the velocity:

$$\frac{1}{v} \frac{dv}{dr} + \frac{2}{r} = -\frac{1}{n} \frac{dn}{dr} \quad (1.5)$$

that we can use to eliminate n from equation (1.3) and obtain:

$$\frac{1}{v} \frac{dv}{dr} \left(1 - \frac{v^2}{v_c^2}\right) = \frac{2}{r} \left(\frac{r_c}{r} - 1\right). \quad (1.6)$$

Here we introduced the constants so that $v_c^2 = \frac{2kT}{m_H}$ and $r_c = \frac{GMm_H}{4kT}$, where v_c corresponds to the sound speed of the gas.

This differential equation can be solved by variable separation and integration. It is convenient to introduce a new variable $k = v^2$, $dk = 2v dv$. After performing the integration from some point r_0 to r (and $v^2(r_0)$ to $v^2(r)$ respectively) we arrive at:

$$\ln(v^2) - \left(\frac{v}{v_c}\right)^2 = -4 \left(\frac{r_c}{r} + \ln(r)\right) + C(r_0). \quad (1.7)$$

In order to solve this equation we need some additional constraints about the function $v(r)$ and choosing the integration start point r_0 . Lets look closely at the differential form in (1.6). A reasonable choice of r_0 would be a point somewhere close to the solar surface. For solar parameters this means that $r_0 < r_c$ (as $r_{c\odot} \sim 6R_{\odot}$) and the right side of equation (1.6) being positive for $r \in (r_0, r_c)$, negative for $r > r_c$ and zero for $r = r_c$, which requires the left side to vanish at that point as well. It can be achieved by either $v(r_c)$ going to infinity (which is not physically feasible, hence we discard this case), (a) velocity having an extremum at $r = r_c$ (meaning $\frac{dv}{dr} = 0$) or (b) $v(r_c) = v_c$ (making the expression in parenthesis zero). We shall neglect the case in which conditions (a) and (b) happen at the same time, since it gives a solution that is not a function (does not

prescribe unambiguous values), and focus on these two cases separately.

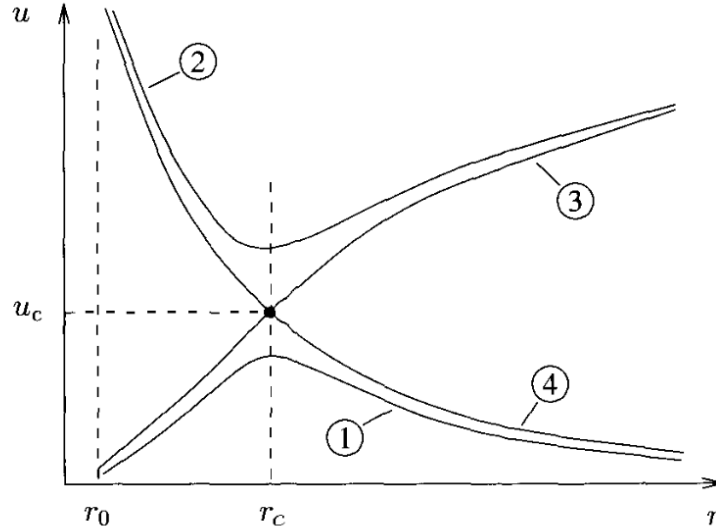


Figure 1.2: Family of solutions of the velocity profile ($v(r)$) for the Parker wind model. For a detailed description please refer to the text. Source: [Prölss & Bird \(2004\)](#).

Condition (a) implies that the expression in parenthesis $(1 - \frac{v^2}{v_c^2})$ is always negative or positive, since the right side of the equation has only one point in which it changes sign and it corresponds to the derivative of v changing the sign on the left side, which forces v to be always greater or always smaller than v_c . This gives us two solutions: (1) $v < v_c$, and slope of v going from positive ($r \in (r_0, r_c)$) to negative ($r > r_c$) and a maximum $v(r_c) < v_c$; (2) $v > v_c$, slope changing from negative to positive and a minimum $v(r_c) > v_c$. Respective curves are depicted in Fig. 1.2.

Case (b), $v(r_c) = v_c$, allows no change in the slope of the velocity profile, constraining velocities to be either greater than v_c , then decreasing and finally being smaller after passing the critical point r_c , or the opposite way. We end up with two monotonic solutions, where the velocity profile is always increasing (3) or always decreasing (4), as further depicted in Fig. 1.2.

As discussed in section 1.1, observations require the solar wind to have almost zero velocities close to the Sun and large ones far from it. We shall then limit ourselves to the class of solutions number (3), since it is the only one fulfilling these requirements. With the additional constraint of $v(r_c) = v_c$ we can now determine the integration constant from equation 1.7 and arrive at the final

form of the velocity function:

$$\frac{v^2}{v_c^2} - 2 \ln\left(\frac{v}{v_c}\right) = 4 \ln\left(\frac{r}{r_c}\right) + 4 \frac{r_c}{r} - 3. \quad (1.8)$$

This allows us to form a problem as:

$$f(v) - g(r) = 0 \quad (1.9)$$

meaning that we can choose r , calculate the value of $g(r)$ and find the zero of the resulting function to obtain the respective value of v . One must be careful, since such a method yields two zeros at the time, relating to the families (3) and (4), and the choice of the correct one depends on r with respect to r_c . The numerical solution of this equation has been performed by us using the bisection method for different temperatures (on which r_c and v_c depend) and can be seen in Fig. 1.3. Such a solution for temperatures of around 2mln K is in agreement with the near-Earth measurements of the solar wind.

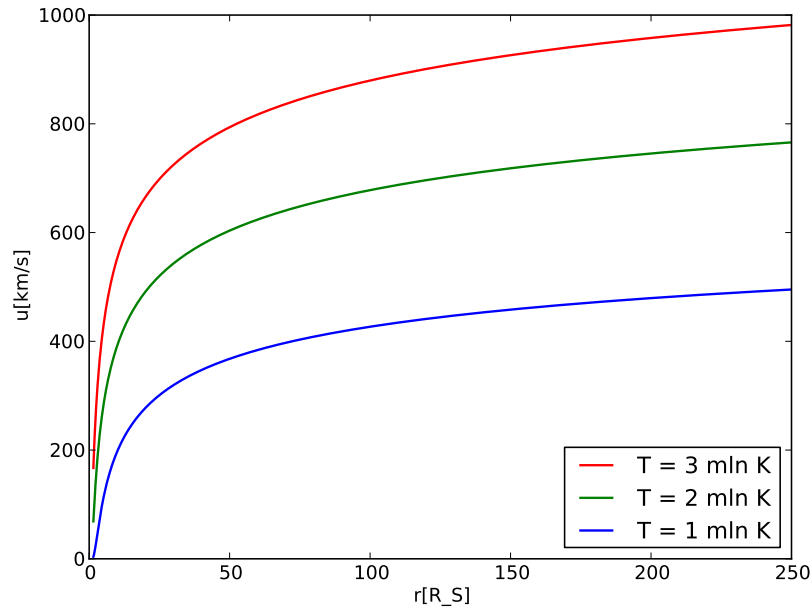


Figure 1.3: Numerical solutions for the isothermal Parker wind calculated for different temperatures.

This concludes our discussion of the basic, pressure-driven, isothermal winds that we use later as a test cases for our simulations.

1.3 Line-driven winds

There are many other mechanisms that can power stellar winds (e.g. wave driven winds, dust driven winds), but we shall now discuss the one that is relevant in the massive, early-type stars. These hot stars emit a lot of energetic, UV radiation. Their atmospheres are rich in ions that produce lines with large opacities, making it very easy for photons to be absorbed by ions and to be scattered by electrons. Being absorbed and re-emitted, photons will transfer part of their momentum to the ions, which then can distribute it to other wind particles. A given ion can absorb a photon at some very specific frequency, but thanks to the Doppler effect due to the radial velocity change in the wind, the ion will at different radii be able to absorb photons from different emitted frequencies that it will see as redshifted. This combined with large luminosities of these stars makes such process a very efficient at wind-driving.

1.3.1 A few simple estimates

Firstly, let's look closely on how the photons can transfer their momentum and energy to the wind for a single ion, as depicted in Fig. 1.4. An atom or an ion absorbs a photon of frequency ν , which is then re-emitted. The absorber of mass m has the initial velocity v in the radial direction (a valid assumption, since this will be the dominant velocity component) and is moving outward of the star, just as the photon. Momentum conservation can in this case be expressed as follows:

$$mv + \frac{h\nu}{c} = mv', \quad (1.10)$$

where v' is the absorber's velocity after the absorption. Note that there is no need for a vector equation since during absorption all velocities are in the

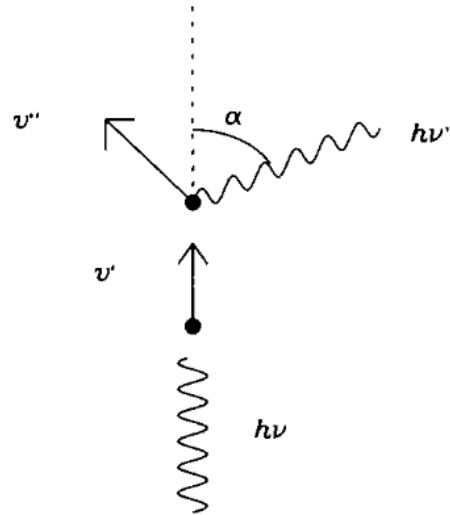


Figure 1.4: Scheme of the system for photon absorption and re-emittance.

common, radial direction. The velocity gain can then be written as :

$$\Delta v = \frac{h\nu}{mc}. \quad (1.11)$$

Then the photons gets re-emitted with a frequency ν' and at an angle α with respect to the radial direction. The momentum conservation in radial direction will then be:

$$m\nu' = m\nu'' + \frac{h\nu'}{c} \cos \alpha, \quad (1.12)$$

where ν'' is the final velocity of the absorber. Now we need to consider that in its rest-frame, the absorber can only absorb photons of frequency ν_0 . In the star's rest frame (with respect to which we measure the velocities), the frequencies will then be appropriately redshifted:

$$\nu = \nu_0 \left(1 + \frac{v}{c}\right), \quad \nu' = \nu_0 \left(1 + \frac{v'}{c}\right). \quad (1.13)$$

Combining equations (1.10), (1.12) and (1.13) we can express the final absorber's radial velocity as:

$$\nu'' = \nu + \frac{h\nu_0}{mc} \left(1 + \frac{v}{c}\right) (1 - \cos \alpha) - \frac{1}{c} \left(\frac{h\nu_0}{mc}\right)^2 \left(1 + \frac{v}{c}\right) \cos \alpha. \quad (1.14)$$

In the non-relativistic case of $v \ll c$ and $h\nu_0 \ll mc$ (which is confirmed observationally) we can calculate the resulting velocity gain as:

$$\Delta v = \frac{h\nu_0}{mc} (1 - \cos \alpha). \quad (1.15)$$

This result is consistent with intuition. If the photon is scattered in the same direction ($\alpha = 0$), there is no velocity gain, and the momentum transfer is largest if the photon is scattered backwards with $\alpha = 180^\circ$ then being equal to $2\frac{h\nu_0}{mc}$. There is no favored direction for the re-emission allowing us to simply integrate over a sphere and arrive at the final, averaged result:

$$\langle \Delta p \rangle = \langle m \Delta v \rangle = \frac{h\nu_0}{c}. \quad (1.16)$$

We see that this is the same result as in the case of pure absorption (equation (1.11)). If the radiation field was isotropic, this would mean that on average there would be no effective momentum transfer to the gas. Thus, we can then ignore all external isotropic radiation fields (provided still being in the non-relativistic regime).

Not only the momentum, but also the energy is transferred from photons to the wind particles.

This energy is used to overcome the potential well of the star and goes into the kinetic and thermal energy of the wind. This energy loss however reduces the star's luminosity only by a very small factor.

As one could expect, only some of the composite particles of the wind can be accelerated by this process (mostly ions of C, N, O, Ne, Si, P, S and Fe, since their transition frequencies correspond to the maximum of stellar flux). There are additional particles in the wind, mostly protons, electrons and helium ions, that have to somehow get this momentum as well in order for the flow to be steady. This happens by an interactions of the absorbers with the other particles via electric forces and is therefore called the Coulomb coupling. We note that in case of the solar wind and Sun-like stars, the Coulomb collisions are quite rare and would not provide an efficient momentum transfer, as it requires much higher densities than are present in the winds of early-type stars.

Let us now look at one specific line of the rest-frame frequency ν_0 . As an approximation the star emits a continuum with a flux $F(\nu)$ at the stellar surface. The wind's velocity is nearly zero at the stellar surface and goes to its maximal, terminal velocity v_∞ at infinity. We assume the wind to be optically thick for the line (making this an efficient driving mechanism in the first place), which implies that practically all the photons of frequency ν_0 will be absorbed close to the star, and all photons of the Doppler shifted frequency $\nu_0(1 + v_\infty/c)$ will be absorbed at the outer layers of the wind where it reaches the terminal velocity. Since the velocity profile is a monotonically increasing function, v will take all the values between 0 and v_∞ along the wind meaning that the absorbing ion will be able to absorb all the frequencies between ν_0 and $\nu_0(1 + v_\infty/c)$ (as it will see it as ν_0 in its rest frame). This is shown schematically in Fig. 1.5.

The energy transferred to the wind per unit time is then:

$$L_{abs} = \int_{\nu_0}^{\nu_0(1+v_\infty/c)} 4\pi R^2 F(\nu) d\nu, \quad (1.17)$$

where R is the radius of the star. This can easily be translated to the momentum gain per unit time (as it is photons loss):

$$\frac{p_{abs}}{\Delta t} = \frac{L_{abs}}{c}. \quad (1.18)$$

The existence of maximal a velocity means that the wind cannot carry out more momentum than $\dot{M}v_\infty$, which has to be then equal to the expression (1.18). The width of the absorbed frequency range is $\Delta\nu = \nu_0 \frac{v_\infty}{c}$, so in the non-relativistic regime it will be quite thin (as $v_\infty \ll c$). In that case we can assume the flux to be constant over that range and make the approximation of the

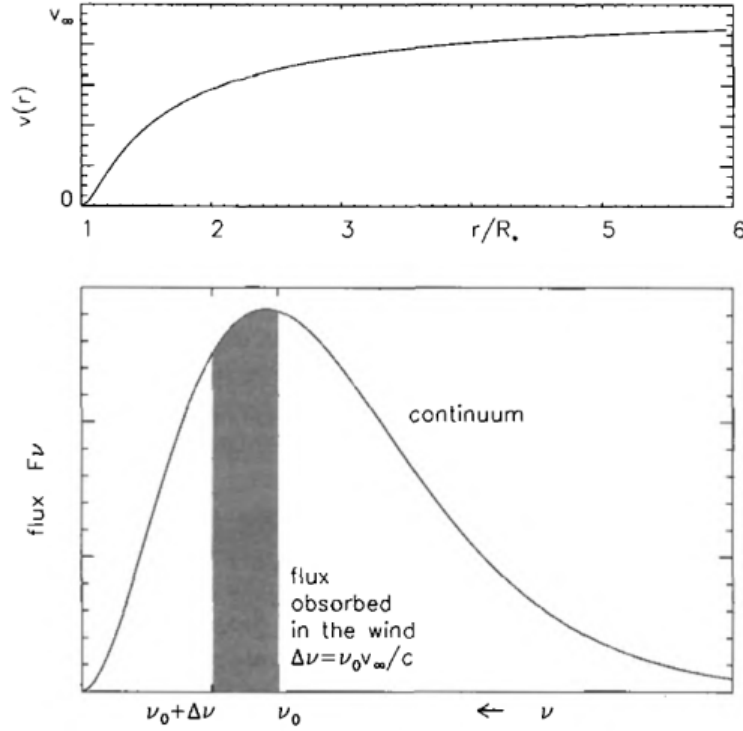


Figure 1.5: The upper graph shows a velocity profile $v(r)$ going from 0 at the stellar surface to its maximal value of v_∞ far from it. The bottom figure depicts which part of the continuum stellar emission can be absorbed by a given ion with the line transition of frequency ν_0 thanks to the Doppler effect. This line is close to emission maximum, making it possible to transfer large quantities of energy. Figure source: [Lamers & Cassinelli \(1999\)](#).

momentum transferred from the radiation to the wind by a single spectral line as:

$$\dot{M}v_\infty = \int_{\nu_0}^{\nu_0(1+v_\infty/c)} \frac{4\pi R^2}{c} F(\nu) d\nu \simeq \frac{4\pi R^2}{c} F(\nu_0) \nu_0 \frac{v_\infty}{c}. \quad (1.19)$$

Both sides of this equation contain v_∞ , so we arrive at an expression for the mass loss rate \dot{M} . This can be understood intuitively : if we increase the terminal velocity by some factor, the absorbed frequency range (which depends linearly on v_∞) will broaden by the same factor as will the momentum taken from the radiation. The wind's momentum is proportional to v_∞ as well, so the momentum transferred per unit mass will remain exactly the same.

Now we can use equation (1.19) to estimate the mass loss rate produced by one line. Assuming

the continuum radiation to be a blackbody with a temperature T_{eff} and that the line is near its peak ($\nu_0 \simeq \nu_{max}$), we can estimate for Planck function $\nu_0 F(\nu_0) \simeq 0.6\sigma T_{eff}^4$, where σ is the Stefan–Boltzmann constant, which allows us, using the equation (1.19) to express the mass loss rate as:

$$\dot{M} \simeq 0.6 \frac{L}{c^2} \simeq \frac{L}{c^2}, \quad (1.20)$$

where L is the total luminosity. This calculation has been done for one line, so if we have N lines the total mass loss becomes:

$$\dot{M} \simeq N_{eff} \frac{L}{c^2}, \quad (1.21)$$

where N_{eff} will be the effective number of lines contributing weighted over their transition frequencies with respect to the star's flux. Note that we are assuming that respective frequency ranges do not overlap. The typical massive stars have luminosities of the order of $10^5 - 10^6 L_\odot$ and mass loss rates of the orders of $10^{-6} - 10^{-5} \frac{M_\odot}{yr}$, which could be reproduced by a presence of 150–1500 strong lines in the stellar wind.

We should acknowledge that this approximation is subject to the assumption that the photon does not get absorbed again after being re-emitted (first scattering approximation).

One can discuss the limiting case when all the radiation momentum is transferred to the wind, meaning that the absorbed energy per time unit is the total star luminosity, $L_{abs} = L$. Then from equation (1.18) it follows:

$$\dot{M} v_\infty = \frac{L}{c}, \quad (1.22)$$

giving the upper limit for our approximation of the line-driven stellar winds. We can derive some properties of the wind studying it's actual rate of momentum gain versus the maximum possible rate (making use of equation (1.21)):

$$\frac{\dot{M} v_\infty}{\dot{M}_{max} v_\infty} = \dot{M} v_\infty \cdot \frac{c}{L} \simeq N_{eff} \frac{v_\infty}{c}. \quad (1.23)$$

If the wind with maximal momentum transfer was triggered by the existence of one line only, its terminal velocity would have to be equal to the speed of light. That is understandable, since then the Doppler effect would have to be able to allow for the absorption of the whole frequency range. For a greater line number they would have to divide the range of frequencies among each other, and then the terminal velocity would be $v_\infty \simeq \frac{c}{N_{eff}}$. Note that usually it's the terminal velocity v_∞ that we can measure from observations, so by reversing this argument it can give us the effective number of lines needed for sustaining the outflow, $N_{eff}^{max} \simeq \frac{c}{v_\infty}$. Of course the actual number of lines can and will be greater, since their frequency ranges overlap and also since the momentum

is usually not transferred with the optimal efficiency. In fact the O and B stars usually operate at 20% – 60% efficiency rate. The most massive stars, Wolf-Rayet type, can actually exceed this limit.

One can also wonder how efficient this mechanism is at gaining energy from radiation. For the massive stars it is very little in comparison with their luminosities, several orders of magnitude smaller than the previously discussed momentum transfer. This means that the dominant component of the driving mechanism is the momentum transfer.

1.3.2 The CAK approximation

Let us come back to the general equation of motion first mentioned in (1.2). At first we considered only the pressure and gravitational force. Now the radiation pressure will add a component to this equation in the form of acceleration g_{rad} :

$$\frac{Dv}{Dt} = v \frac{dv}{dr} = -\frac{GM}{r^2} - \frac{1}{\rho} \frac{dp}{dr} + g_{rad}. \quad (1.24)$$

This force can be obtained if we sum up contributions from all possible lines, each one having a range of optical depths. The acceleration for a given line will depend on its opacity at the specific distance and appropriate flux at that point, which depends on the intensity at the stellar surface and absorption in between the star and the point being considered. To solve this for a general case one must apply radiative transfer equations. The problem can be simplified by using the so called Sobolev approximation, which assumes that the interaction region of the photon and the wind is infinitely narrow and allows to use delta function as the line's profile function. This approximation uses a quantity called Sobolev's optical depth τ^S that depends on the line's frequency, absorption coefficient, position of absorption, local wind velocity and density. This makes absorption a local process that depends only on the local wind conditions and does not require the knowledge of physical properties' wider profiles. We shall not discuss this approximation in detail, but the reader can be referred to the Fig. 1.6 that explains the idea visually. With this in mind the acceleration due to a line transition will depend on the local optical depth τ_ν and the local flux, which will now depend only on the intensity I_ν . Even after this approximation, the summation over all possible lines is a daunting task as it requires calculation of their ionization and excitation levels for all present elements. If one additionally assumes that the wind density is low enough for the ions not to get excited, therefore allowing the use of ground state transitions only, one is left with the order of 10^5 lines. Many of these lines can also overlap in terms of the frequency ranges, since they are not distributed uniformly.

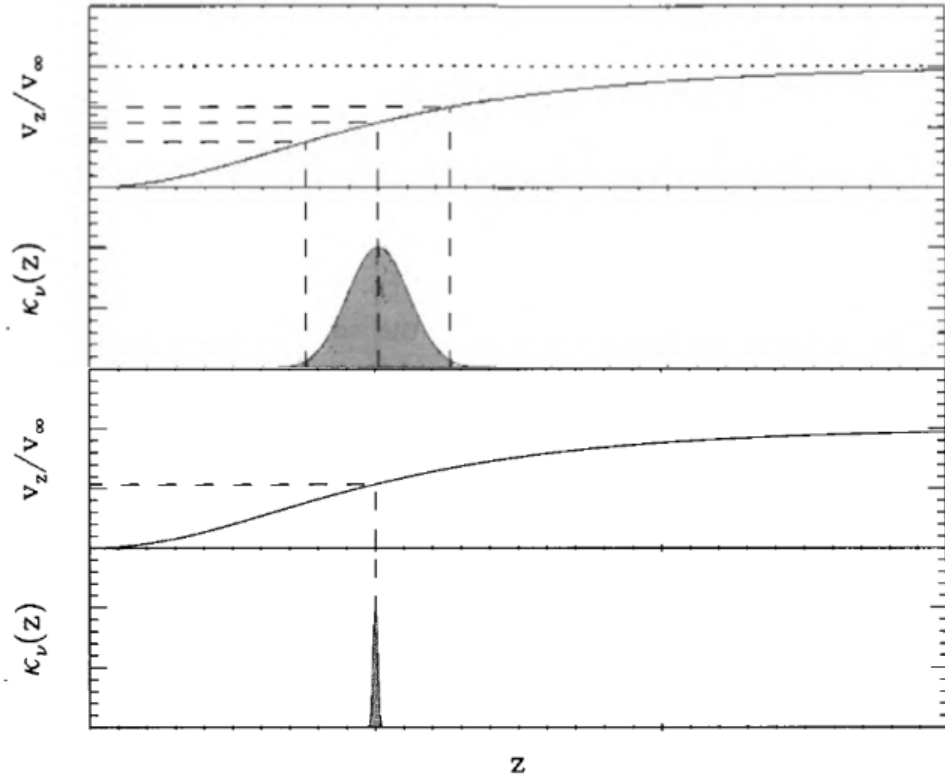


Figure 1.6: The two upper panels show the line of sight velocity v_z and the absorption coefficient κ_ν that depends on the line's profile. One can see that the absorption takes place over a wide range of velocities, implying a wide range of radii and physical conditions. The two bottom panels show the same situation with the Sobolev's approximation - a narrow line profile that makes the process a local one. Reproduced from: [Lamers & Cassinelli \(1999\)](#).

The effect of performing the summation over all lines has been parameterized in a simple way by [Castor, Abbott, & Klein \(1975\)](#), as follows.

The acceleration due to radiation pressure can be decomposed into the radiative acceleration due to continuum opacity by electron scattering (g_e) and the previously discussed acceleration due to the lines (g_{lin}). The acceleration caused by all the lines can be expressed by the electron acceleration g_e , with some reference electron scattering opacity σ_e^{ref} , multiplied by a factor $M(t)$ called the 'force multiplier':

$$g_{lin} = g_e^{ref} M(t), \quad g_e^{ref} = \frac{\sigma_e^{ref} F}{c} = \frac{\sigma_e^{ref} L}{4\pi r^2 c}, \quad (1.25)$$

where L is the stellar luminosity. $M(t)$ is a function of a dimensionless optical depth parameter of the following form:

$$t \equiv \sigma_e^{ref} \rho v_{th} \left(\frac{dv}{dr} \right)^{-1}, \quad v_{th} = \sqrt{\frac{2k_B T_{eff}}{m_H}}, \quad (1.26)$$

where v_{th} is the mean thermal velocity of the protons in the wind of the same temperature as the star and k_B is the Boltzman constant. We can see that $M(t)$ depends on the chemical composition, the ionization and excitation in the wind, which further depend on T_{eff} and the ratio of electron number density n_e , and the geometrical dilution function $W(r)$ since the photoionization depends on the flux at distance r which is proportional to $W(r)$, and recombination depends on the electron number density.

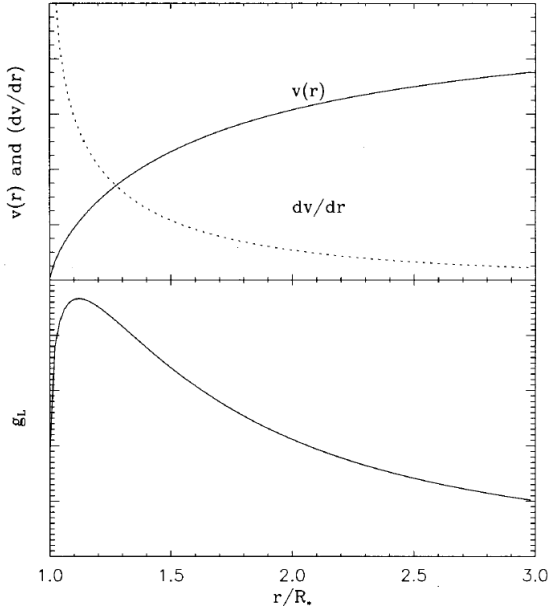


Figure 1.7: The upper figure shows a typical stellar wind profile and its derivative, while the bottom one depicts respective acceleration due to the line absorption in the wind as a function of distance from the star. Figure source: [Lamers & Cassinelli \(1999\)](#).

acceleration increases strongly close to the star, reaches a maximum and then slowly decreases.

The $M(t)$ function is derived from different stellar models and the effective temperatures and can be approximated as a power law. It turns out that the mentioned ratio $n_e/W(r)$ can also be approximated as a power law allowing to express $M(t)$ by a function of parameters k , α and δ (the force multiplier parameters):

$$M(t) = kt^{-\alpha} \left(10^{-11} \frac{n_e}{W} \right)^\delta. \quad (1.27)$$

Values of these parameters for a given T_{eff} can be found in the literature. Parameter α usually takes values between 0.45 and 0.65, meaning that both optically thin and thick lines contribute to the acceleration. The usual literature value of σ_e^{ref} is $0.325 \text{ cm}^2/\text{g}$.

Combining equations (1.25) and (1.27), we can write the radiative line acceleration as:

$$g_{lin} = \frac{\sigma_e^{ref} L}{4\pi r^2 c} kt^{-\alpha} \left(10^{-11} \frac{n_e}{W} \right)^\delta. \quad (1.28)$$

Fig. 1.7 shows the line acceleration for a typical wind velocity function. We can see that the

We also note that the force multiplier factor should be adjusted for specific metal abundances in the winds.

The acceleration from the electron scattering has the form of:

$$g_e = \frac{\sigma_e L}{4\pi r^2 c} = \frac{GM}{r^2} \Gamma_e, \quad \Gamma_e = \frac{\sigma_e L}{4\pi c GM}. \quad (1.29)$$

The electron opacity depends on the chemical composition of the wind and shall be assumed constant (which makes Γ_e constant as well). We can then introduce an effective mass and combine the electron scattering acceleration and the gravitational acceleration together in the form of GM_{eff}/r^2 , where:

$$M_{eff} = M(1 - \Gamma_e). \quad (1.30)$$

Using the assumption of an isothermal, perfect gas as we did in section 1.2, we can derive the pressure gradient as:

$$\frac{1}{\rho} \frac{dp}{dr} = -\frac{v_c^2}{v} \frac{dv}{dr} - \frac{2v_c^2}{r}, \quad (1.31)$$

where v_c is the soundspeed. That allows us to write the general equation of motion with the radiation pressure acceleration term (1.24) as:

$$v \frac{dv}{dr} = -\frac{GM_{eff}}{r^2} + \frac{v_c^2}{v} \frac{dv}{dr} + \frac{2v_c^2}{r} + g_{lin}, \quad (1.32)$$

where we can use the g_{lin} from equation (1.28) and after some rearrangements arrive at:

$$\left(1 - \frac{v_c^2}{v^2}\right) v r^2 \frac{dv}{dr} = -GM_{eff} + 2v_c^2 r + C \cdot \left(v r^2 \frac{dv}{dr}\right)^\alpha. \quad (1.33)$$

Here we included all constants in C :

$$C = \frac{\sigma_e^{ref} L k}{4\pi c} \cdot \left(\frac{\sigma_e^{ref} v_{th} \dot{M}}{4\pi}\right)^{-\alpha} \cdot \left(\frac{10^{-11} n_e}{W}\right)^\delta. \quad (1.34)$$

One could argue that the values of the n_e/W ratio are not constant throughout the wind, but since the δ parameter is usually very small (~ 0.1), keeping it constant will only have a small effect on the solution.

Equation (1.33) is a nonlinear differential equation (due to the α exponent). As in the previous case of the Parker wind, we are looking for a monotonically increasing velocity function, so the right side of the equation has to vanish when $v = v_c$. To study the possible solutions, let us

rearrange the terms as follows:

$$\left(1 - \frac{v_c^2}{v^2}\right) v r^2 \frac{dv}{dr} + (GM_{eff} - 2v_c^2 r) - C \cdot \left(v r^2 \frac{dv}{dr}\right)^\alpha = 0. \quad (1.35)$$

We can see that the expression $(GM_{eff} - 2v_c^2 r)$ is the equivalent of the condition for r_c in Parker's solution, so we will call it the Parker point $r_P = \frac{GM_{eff}}{2v_c^2}$. There are four kinds of solutions shown in Fig. 1.8 that start from the stellar surface, and four that start from infinity. Together they exhaust all the possible solution types.

Solution (a) starts with a velocity smaller than the speed of sound v_c and does not exceed it. It enters the forbidden region B at the Parker point r_P . Case (b) starts also at subsonic velocities and transits to the supersonic ones, but then reaches the point r_P where it fails, since the remaining terms do not cancel out (term $v r^2 \frac{dv}{dr}$ is nonzero). Curve (c) has the same problem, even though it touches upon the forbidden region A . Solution (d) starts at small velocities and reaches the supersonic ones and then enters the forbidden region since the Parker term $GM_{eff} - 2v_c^2 r$ is too big. Then we move on to the functions that are calculated from $r = \infty$ backwards. (e) starts supersonically at infinity and with too high velocity enters region A . Solution (f) starts supersonically, touches upon the region A and fails the transition to subsonic velocities. Case (g) also fails at the supersonic transition. Finally curve (h) starts supersonically and enters the forbidden region B at the sonic point.

This very simplified analysis gives us the idea that only the combination of curves of type (c) and (f) can produce a type of solution that would satisfy physical (and observational) conditions. The critical point is where both solutions meet with the same velocity gradient. This kind of function gives a unique value for the mass loss rate and the terminal velocity of the wind.

Here we conclude our brief discussion of the line-driven stellar winds. It has to be noted that all of this was done for a single scattering approximation (meaning that a photon scatters only once). In reality, especially for very massive, dense stellar winds like in Wolf Rayet stars one should really consider the multiple scattering case, as otherwise the momentum transfer can be underestimated up to a factor of 6. For the O and B stars, the underestimation is only by a factor of about 2.

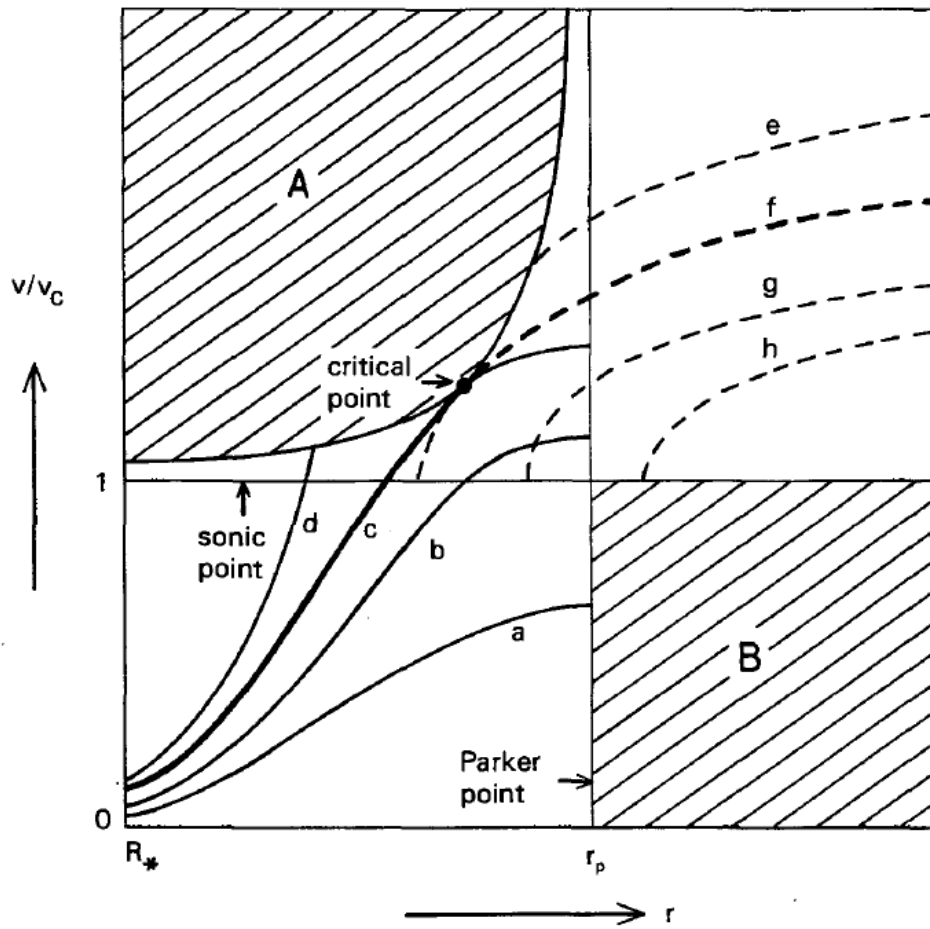


Figure 1.8: Solution of the momentum equation with the radiation pressure acceleration term. Please refer to text for a thorough discussion. The point marked as 1 on the velocity axis marks transition to supersonic velocities. Regions *A* and *B* are forbidden (not part of the solution). Figure source: [Lamers & Cassinelli \(1999\)](#).



Figure 1.9: Massive stellar wind from the Wolf-Rayet 124 known as nebula M1-67. Image credit: HST, APOD.

Massive stars

There is a plethora of types of binary stellar systems in the Universe. We focus our attention on the case where both of the components are massive stars capable of producing strong, massive stellar winds, as the magnetic fields of such systems are the focus on our study. In this chapter, we first comment on what we mean by a 'massive star', and then, we discuss the properties of their magnetic fields.

2.1 Physical properties

Massive stars are not very numerous, but they are certainly important astronomical objects. During their short lives, with their strong outflows and high luminosities, they enrich the interstellar medium with particles and photons energetic enough to ionize it. They explode as supernovae spreading heavy elements around the galaxies or turn into compact objects and possibly gamma-ray bursts. Therefore it is crucial to understand them and their evolution better than we do now.

Stellar mass is an important parameter in stellar classification, since it is related to their lifetime and evolutionary path. The term 'massive star' is usually applied to any main sequence object with a mass greater than 8 solar masses. Those kinds of objects will usually have short lives that will end violently in supernova explosions. Stars are also classified according to their so called spectral types in a sequence based approximately on the line widths, and as was later realized, their temperature. The first and hottest two types in this sequence are O and B, constituting the majority of binaries that fulfill our criteria. They are called early-type stars, owing this naming scheme to a now-invalidated stellar evolution theory, according to which stars become cooler with age, going from O to M types, as they would if they used mass for energy and as a result experienced a drop in luminosity as well as temperature. Therefore the hottest stars of O and B types would be the starting points of such evolutionary scheme, giving them to this day the "early-type" name. Their characteristic color is blue-white and they have strong absorption lines in their spectra with very bright continua. General properties can be seen in Fig. (2.1) depicting the so called Hertzsprung-Russell diagram with main sequence stars, where the early type stars occupy

Table 2.1: Ranges of typical physical properties of O and B spectral type stars. Source: [Carroll & Ostlie \(1996\)](#).

| Quantity: | $T_e[10^4 K]$ | $L[10^5 L_\odot]$ | $R[R_\odot]$ | $M[M_\odot]$ |
|-----------|---------------|-------------------|--------------|--------------|
| Range: | 1 – 4 | 1.5 – 11 | 2-60 | 8-70 |

the upper left corner. This means that these are the biggest, hottest and most luminous of stars. Typical physical parameter ranges are presented in Table 2.1.

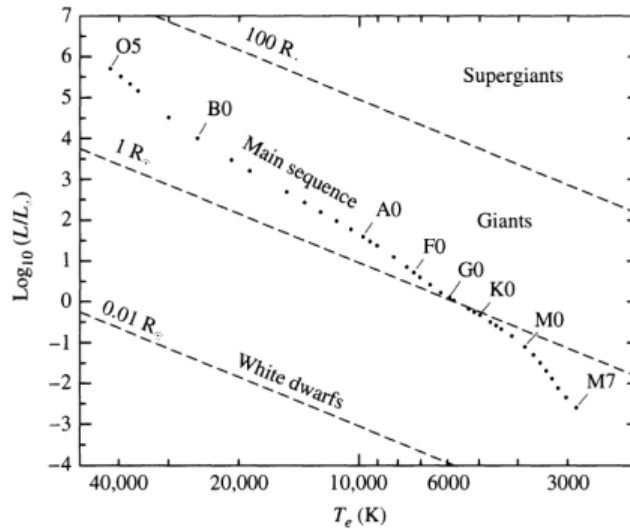


Figure 2.1: The Hertzsprung-Russell diagram shows the main properties of different spectral types. We see that O and B types occupy the upper left corner, making them the biggest, hottest and most luminous main-sequence stars. Figure source: [Carroll & Ostlie \(1996\)](#).

At some point of their evolution before exploding as a supernova, the O type stars exhibit a period of violent wind outflow, observationally known under the broad term of a Wolf-Rayet star. These objects exhibit very broad and strong emission rather than absorption lines. Their effective temperatures can be as high as $2.5-10 \cdot 10^4 K$ and they have unusually high mass loss rates of the order of $10^{-5} M_\odot/\text{yr}$, meaning they have very strong stellar winds (making them interesting objects in our study). What is more they do not require high progenitor masses. Their peculiar spectra are explained by the star having lost all of its hydrogen envelope allowing the elements synthesized by the nuclear core reactions to reach the surface. In some cases even the underlying

layer of dredged-up products of the CNO cycle is blown away. If the star does not go out of hydrostatic equilibrium during that phase, even deeper lying layers can be blown away, leaving the O from the triple-alpha core reactions. Their life (as their progenitor was an O star) will end in a supernova explosion. An example of this kind was depicted in the previous chapter (Fig. 1.9).

We note that the properties described above, especially high temperatures and large luminosities, provide a suitable environment for efficient line driven stellar winds (described in detail in section 1.3). It has to be acknowledged that in case of the Wolf-Rayet stars the single scattering assumption employed in our treatment is actually rather unrealistic. Multiple scattering enhances wind momentum, which would explain higher mass loss rates for these objects. Unfortunately such process requires much more sophisticated treatment (Monte Carlo methods), which we are not able to introduce at this time. Since the resulting underestimation is not by a large factor, we choose to neglect it.

2.2 Magnetic fields

There are some spectral properties of massive stars that are still not perfectly understood, such as UV variability or X-ray emission, that could perhaps be explained by magnetic field's presence. Here we summarize the observational evidence for the existence of such fields, ranges of their strengths and current theories with respect their influence on the stellar winds.

In his paper about the solar wind, [Parker \(1958\)](#) has discussed the general effect of the wind on the solar dipole magnetic field. He concluded, that the plasma outflow will carry away the field lines making the field radial (ignoring the rotation of the Sun). One may expect that this will happen for rather weak magnetic field (as $B_{\odot} \sim 1G$), but there can be a case where the magnetic field greatly influences plasma's properties. The idea was further explored and extended to the case of other stars by [Weber & Davis \(1967\)](#), where they noted the existence of different regimes of wind/magnetic field domination. Even such early works as those two showed that the magnetic field plays a role in the structure and properties of the stellar winds. Now we shall try to see its effects on massive stars and their winds.

2.2.1 Observational evidence

The early-type stars have a completely different internal structure than the smaller stars in which the dynamo is believed to be responsible for the magnetic fields. Some of the intermediate-mass stars have measured magnetic fields that are either stronger than $B_p \sim 300G$ or virtually non-existent ([Aurière et al., 2007](#)). There is also no notable connection between the physical

stellar properties and the respective magnetic fields (e.g. [Donati & Landstreet, 2009](#)). Currently it is believed that those magnetic fields are the remnants left by the large scale Galactic field, that might have been strengthened by an inner dynamo in the early stages of star's evolution ([Moss, 2001](#)).

There is no complete theory describing the origin of the magnetic fields in massive stars. It seems that the majority of those massive stars having a detectable magnetic field are the extension of the intermediate-mass stars described above and the scenario of the fossil Galactic fields could be also extended to them. The Magnetism in Massive Stars (MiMeS) project has set out to survey massive stars in search for their magnetic fields ([Grunhut & Wade, 2013](#)). They have observed ~ 550 stars among which ~ 65 have yielded statistically significant magnetic fields. Among the sample 8% of B type stars and 6% of O type stars have showed detectable magnetic fields. All these showed organized fields with a significant, if not dominant, dipole component. The measured values were in the range of a few hundreds up to $20kG$. The survey concluded that the O and B stars have similar fields to those of the intermediate-mass stars, not showing correlations with physical parameters.

Wolf-Rayet stars should also possess some magnetic field, as they often evolve to highly magnetized objects such as neutron stars. Recently a search among 11 Wolf-Rayet stars has been conducted ([de la Chevrotière et al., 2014](#)) using wind measurements, where only 3 confirmed detections have been made (of fields of 80G, 130G and 200G). The study placed a conservative, upper limit on the field B_{wind} of 500G and set a typical value on the order of 10-100G in the polar regions.

2.2.2 Magnetic fields, rotation and the winds

As confirmed by observations (discussed in the previous section), the dominant component of the magnetic field in early-type stars is the dipole.

We shall now describe the model by [Usov & Melrose \(1992\)](#), as it is a base for more recent models and is the one commonly used for magnetic field estimates in the literature on colliding wind binaries (enabling a direct comparison in the following sections). They divide the magnetosphere in two regions, one where the magnetic field traps the wind particles which then co-rotate with the star, and the other where the rest of the gas is free to flow outwards radially dragging the field along. This can be seen in [Fig. \(2.2\)](#). By equating the ram pressure to the magnetic stress tensor typical component (expressed in CGS units):

$$\rho v^2 = \frac{B^2}{4\pi}, \quad (2.1)$$

we can calculate the point r_A where this happens, and where the magnetic field stops dominating over the plasma flow.

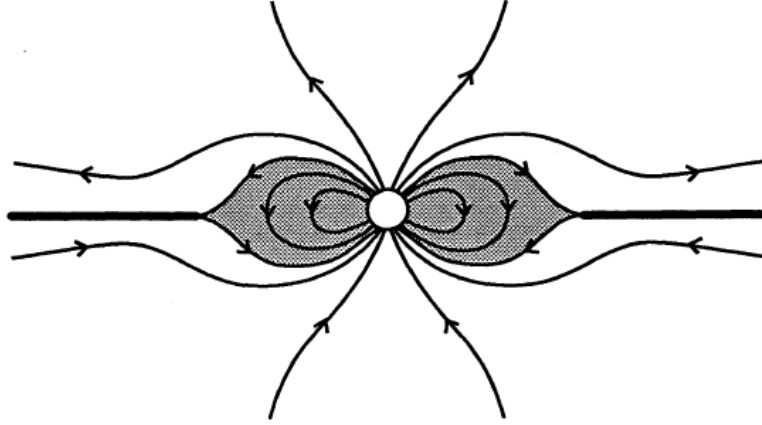


Figure 2.2: Topology of the magnetic field and a plasma outflow. Thick lines note the current sheet, the shaded area the region in which the field confines the plasma. Far from the star the wind drags the field along and both become radial. Figure source: [Usov & Melrose \(1992\)](#).

The wind's velocity profile can, in a very simple manner, be approximated as:

$$v(r) = v_\infty \left(1 - \frac{R}{r}\right), \quad (2.2)$$

where, as before, R is the stellar radius and v_∞ the wind's terminal velocity. It is then assumed that for $r < r_A$ the field keeps its dipolar structure and becomes radial outside of it. Outside this radius we will have perfect mass conservation meaning:

$$\dot{M} = 4\pi r^2 \rho v. \quad (2.3)$$

Then combining equations 2.1, 2.2 and 2.3 we can be write:

$$\left(1 - \frac{R}{r_A}\right) = \frac{B^2 R^2}{\dot{M} v_\infty} \left(\frac{R}{r_A}\right)^4 = \xi \left(\frac{R}{r_A}\right)^4, \quad \xi = \frac{B^2 R^2}{\dot{M} v_\infty} \quad (2.4)$$

Massive stars are known to have rotation velocities at the stellar surface of around 10-20% of their winds' terminal velocities. This introduces a toroidal magnetic field component, that will impose additional field regime:

$$B_\phi \simeq B \frac{v_{rot}}{v_\infty} \frac{r}{R}, \quad (2.5)$$

which becomes important at $r_{tor} = R \frac{v_\infty}{v_{rot}}$, as first stated by [Weber & Davis \(1967\)](#). Combining all of the above we can estimate the magnetic field strength as:

$$B(r) \simeq B_0 \times \begin{cases} \left(\frac{R}{r}\right)^3 & r \in \langle R, r_A \rangle, \\ \frac{R^3}{r_A^2} & r \in \langle r_A, r_{tor} \rangle, \\ \frac{v_{rot}}{v_\infty} \frac{R^2}{r_A r} & r \in \langle r_{tor}, \infty \rangle, \end{cases} \quad (2.6)$$

where B_0 is the field on the stellar surface in the equatorial plane.

As seen in Fig. (2.2), a current sheet forms in the radial regime where the opposite field lines meet. [Usov & Melrose \(1992\)](#) suggest that in principle magnetic reconnection occurs there and one could expect the energy to go to the gas heating or particle kinetic energy, increasing the temperature up to $10^7 K$, leading to X-ray emission.

A more advanced model is proposed by [ud-Doula & Owocki \(2002\)](#) and [Ud-Doula et al. \(2008\)](#). They introduce a magnetic field confinement parameter $\eta(r, \theta)$ that describes the ratio between the energy densities of the magnetic field and the kinetic energy of the wind (in CGS units):

$$\eta(r, \theta) \equiv \frac{B^2}{8\pi} \cdot \frac{2}{\rho v^2}. \quad (2.7)$$

The velocity profile can again be approximated by equation 2.2. Assuming the magnetic field to be a dipole, it can be described as:

$$B_0^2(\theta) = B_*^2 \left(\cos^2 \theta + \sin^2 \frac{\theta}{4} \right), \quad (2.8)$$

$$B(r) = B_0 \left(\frac{R}{r} \right)^3. \quad (2.9)$$

The confinement parameter in the equatorial plane ($\theta = \frac{\pi}{2}$, $r = R$), where the field the most strongly competing element against the radial outflow, is then:

$$\eta\left(\frac{\pi}{2}, r\right) = \frac{B_0^2\left(\frac{\pi}{2}\right)R^2}{\dot{M}v_\infty}. \quad (2.10)$$

For solar values one obtains $\eta_\odot \simeq 40$, which implies the field confining the solar coronal expansion corresponding to the observed magnetic loops.

From this discussion we can define the Alfvén radius R_A as the radius where the magnetic field

loses its domination over the flow by:

$$\eta(R_A) \equiv 1. \quad (2.11)$$

Their model predicts increased density in the magnetic loops and in the slowly expanding equatorial thin disk, that produces shocks and heats up the gas so that it is capable of emitting X-ray radiation.

ud-Doula & Owocki (2002) have performed 2D numerical simulations to test how the confinement parameter at the stellar equator $\eta_{eq} \equiv \eta(\frac{\pi}{2}, R)$ influences the field topology. They found that the equatorial $\eta_{eq} < 1$ characterizes an open, radial field dragged out by plasma. But the magnetic field can still influence the flow by increasing the density and reducing the velocity in the equatorial plane. For $\eta_{eq} > 1$ they find a local confinement and open topology at large radii. Inside the loops the plasma flows to their tops creating shocks capable of producing X-rays. In the open field regime they find a thin, dense, slowly outflowing disk at the magnetic equator. An increase in the terminal speed in polar directions has also been observed.

ud-Doula et al. (2013) have applied this scheme to 3D modeling of a real magnetic O star θ^1 Ori C ($\eta_{eq} \simeq 14$) and showed that they match high-resolution Chandra X-ray observations and correctly predict the temperature and luminosity of the emitting plasma. The topology of the simulated magnetic field is shown in Fig. (2.3).

Going further, one must analyze how the rotation is affecting the wind. For this, a rotational parameter W is introduced:

$$W \equiv \frac{v_{rot}}{v_{orb}}, \quad (2.12)$$

where $v_{orb} = \sqrt{GM/R}$ is the orbital velocity at the stellar surface. For the non-magnetic stars the angular momentum conservation forces the azimuthal velocity components to decline fast, hence they do not influence the wind on larger scales.

In the case of strongly magnetized stars the field can introduce torques on the wind particles allowing even for a nearly rigid rotation with a radially increasing azimuthal velocity:

$$v_{\phi}(r) = v_{rot} \frac{r}{R}, \quad r < R_A. \quad (2.13)$$

The azimuthal velocity component introduces a centrifugal force that will be equal at some point to the gravitational force (lets call it the "Kepler radius" R_K):

$$\frac{v_{\phi}^2(R_K)}{R_K} = \frac{GM}{R_K^2}. \quad (2.14)$$

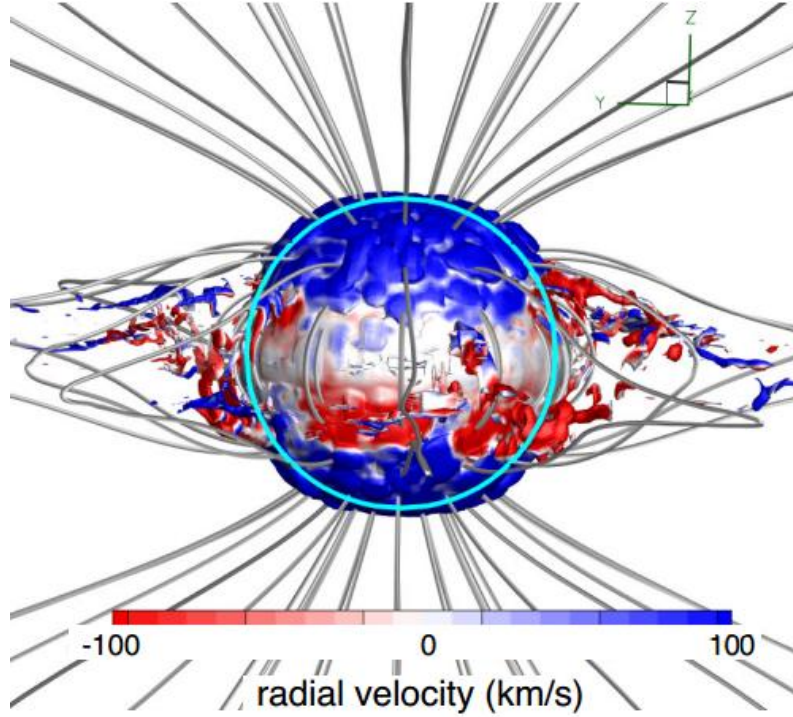


Figure 2.3: MHD simulations of the wind of the star θ^1 Ori C. Surface for constant density near the stellar surface. Colors describe plasma velocity. In the polar region we see radial outflow, while in the equatorial plane the plasma falls back on the surface. Figure source: [ud-Doula et al. \(2013\)](#).

Using the previous notation R_K can be written as:

$$R_K = W^{-2/3} R. \quad (2.15)$$

Particles that are at $r < R_K$ will tend to fall back on the stellar surface, while those further away will be able to escape the gravity pull (unless kept in by the magnetic field). Particles trapped in the loops will accumulate due to the centrifugal force acting on them and will become a part of the rigidly rotating magnetosphere. After some time though plasma will get sufficiently dense to break the loop and open the magnetic field. The possible scenarios can be divided based on the relation between R_A and R_K . For models where $R_A < R_K$ a very weak confinement is observed, with only small influence in the equatorial density. When $R_A \simeq R_K$ models show a complicated interplay between the in-fall and breaking out of the loops. The rigid rotation of trapped material is seen when $R_A > R_K$, where the magnetic field is capable to overcome the centrifugal

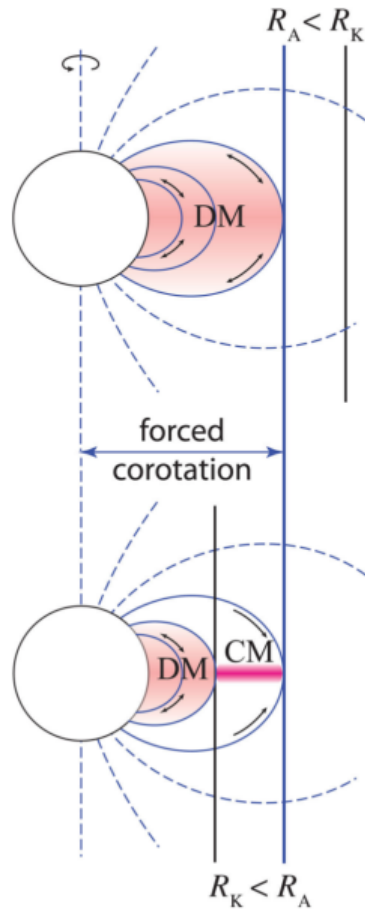


Figure 2.4: Comparison of regimes related to R_A and R_K . The upper sketch depicts the case of slow rotation, where $R_K > R_A$. The centrifugal force acting on the trapped plasma is too small to help it escape, so the particles fall back onto the star. This happens on dynamical timescales making this a dynamical magnetosphere (DM). The bottom figure illustrates more rapid rotation, where $R_K < R_A$. The region in-between the two radii is where the centrifugal force is counteracted by magnetic loop's pressure forcing the plasma to rotate with the star as a centrifugal magnetosphere (CM). Figure source: [Petit et al. \(2013\)](#).

force. These regimes are depicted and further commented in Fig. (2.4). One should note that all of these scenarios are highly dynamical, especially close to the stellar surface.

The model described above is far more detailed than the early works of [Usov & Melrose \(1992\)](#) and models the magnetosphere much more thoroughly. We conclude that the magnetic field plays an important role in massive stars and can substantially change wind properties, hence influencing the wind collision region that is under investigation. It must be noted though that at this stage there are no reasons to suspect strong magnetic fields being present more often in colliding wind binary components than in the general population of massive stars. Therefore not in all of them the field will have high influence over the collision region.

Colliding Wind Binaries

Now let us consider binary systems composed of two massive stars with powerful winds, orbiting each other. If the distance is large enough for the weaker wind not to be suppressed by the ram pressure of the stronger one, the winds can interact and a double-shock structure is created. Below we will discuss schematic theoretical description, observational evidence and briefly summarize current modeling efforts.

3.1 Wind collision region structure

Here we shall follow the early works of [Eichler & Usov \(1993\)](#) and [Stevens et al. \(1992\)](#), which are still a main theoretical reference for WCRs' (wind collision regions) structure and properties. They concentrate on a binary made of an OB star and a Wolf-Rayet star. As discussed in the previous chapter, we know that the WR stars have significantly larger mass loss rates and stronger winds. Hence this component will dominate and will be called the primary. Both outflows will propagate radially until they collide. In principle, as discussed in section 2.2.2, strong magnetic fields and star's rotation might add non-radial components that might make the collision region structure different than the one described below (we see a hint of that in our simulations, please refer to the results in section 6.3), though in this principal discussion their influence is neglected. The outflows are approximately isothermal and assumed to be dominated by the kinetic energy. In this case the position of the collision region depends on the ratio of momenta carried by the wind particles η (note that this is a different η from the magnetic one in the previous chapter. We keep the original authors' notation):

$$\eta = \frac{\dot{M}_{OB} v_{\infty}^{OB}}{\dot{M}_{WR} v_{\infty}^{WR}}, \quad (3.1)$$

given by the mass loss rates and terminal velocities of both stellar winds.

The collision region will form where both kinetic pressures are equal. For an orbital separation

D the respective distances of both stars to the collision region can then be computed to be:

$$r_{WR} = D \frac{1}{1 + \sqrt{\eta}}, \quad r_{OB} = D \frac{\sqrt{\eta}}{1 + \sqrt{\eta}}. \quad (3.2)$$

The collision region will form closer to the star with the weaker wind, which most likely will mean the star with smaller mass loss rate, since the terminal velocities are usually comparable. It consists of two shock fronts and a contact surface in the middle. This is visualized in Fig. (3.1).

The stellar wind plasma near the collision region will have approximately the same temperatures as the stars' photospheres (usually of the order of $10^4 K$) and they will have supersonic velocities of $\sim 10^6 m/s$. The plasma within the WCR will move away from the line connecting the two stars, as it is pushed away by the temperature gradient and the momentum retained after being slowed down by the shock transition. Near the axis of the system within the collision region the drop in velocity will make the plasma subsonic again, but far away from the axis where the winds collide at some angle, the flow will remain supersonic (the further away from the center, the closer to the wind's speed), as the shocks will become weaker. The shocked particles are heated up to $10^6 - 10^8 K$, at which temperatures they can emit thermal X-rays.

The approximation of the magnetic field in the collision region follows the one presented in section 2.2.2 (in the first part) in equation 2.6, first employed by Eichler & Usov (1993). Using these equation they estimate the magnetic field strength in the collision region to be of the order of 1-10G. Following equation 2.6 they conclude that far away from the WR star at the shock S_1 the toroidal magnetic field component will be dominant. Then the angle between the shock normal vector \mathbf{n} (a normalized vector perpendicular to the shock's surface) and the magnetic field B should be more than 45° , making shock S_1 quasi-perpendicular. For the orientation of the magnetic field at the shock S_2 different regimes are expected. If the distance to the WCR from the OB star (distance based on kinetic considerations only) is smaller than its Alfvénic radius r_A , then the wind from the WR star will interact with the OB star's magnetosphere (hence the field orientation is hard to determine). This could happen for close binaries with small orbital periods. The shock S_2 might fall between r_A and r_{tor} , where the radial field component is dominant. Then, close to the line connecting the two stars the shock will be quasi-parallel and then further away it will turn to be quasi-perpendicular. For $r_{OB} > r_{tor}$ the case is similar as for the S_1 shock, making S_2 a quasi-perpendicular shock everywhere.

The above discussion about the magnetic field structure followed Eichler & Usov (1993). We would like to note that, as described in the second part of section 2.2.2, using magnetized massive star wind simulations that considered stellar rotation Ud-Doula et al. (2008) concluded that the rotation affects magnetic field topology only close to the stellar surface rather than, as

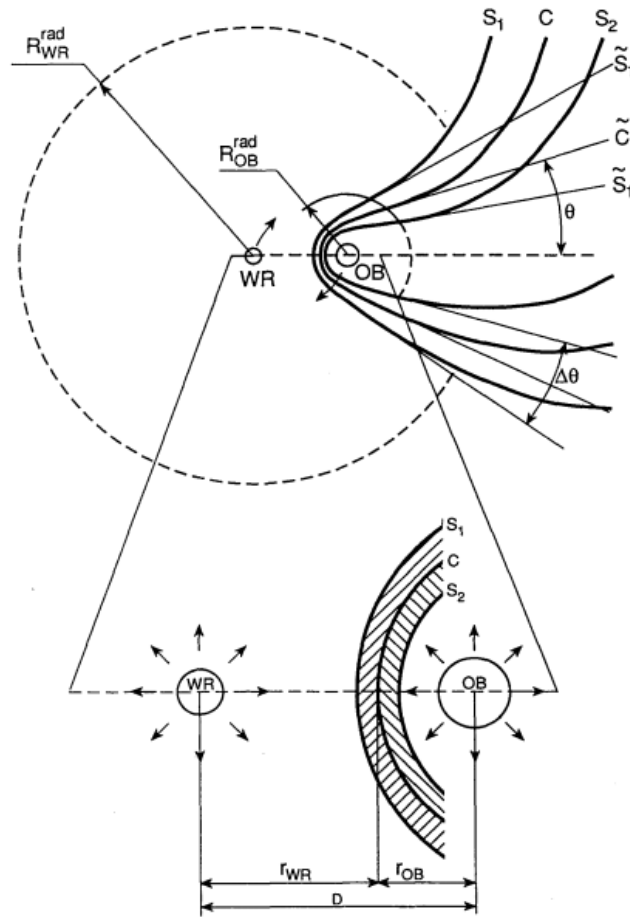


Figure 3.1: Structure of a wind collision region. S_1 and S_2 mark the shocks and C the contact discontinuity. \tilde{S}_1 , \tilde{S}_2 and \tilde{C} are conic surfaces that would form if the stars were not in motion (they would spread up to the point where the winds would interact with the interstellar medium). The actual surfaces are disrupted by the orbital motion and are asymptotic to the conic ones only very close to the stars (as these regions form first). The stars' orbital velocities are marked by arrows. The bottom panel shows the inner region in more detail. At larger distances the surfaces S_1 , S_2 and C will have spiral forms. Figure source: [Eichler & Usov \(1993\)](#).

in equation 2.6, at the largest scales, where they find radial field dragged by the plasma outflow instead.

Apart from the mentioned thermal X-rays, the wind collision region can in principle be observed in highly energetic non-thermal radiation in the form of synchrotron radiation of particles

accelerated at the shocks and then interacting with the magnetic field . The strong shocks in the colliding stellar winds can therefore be an efficient particle accelerators.

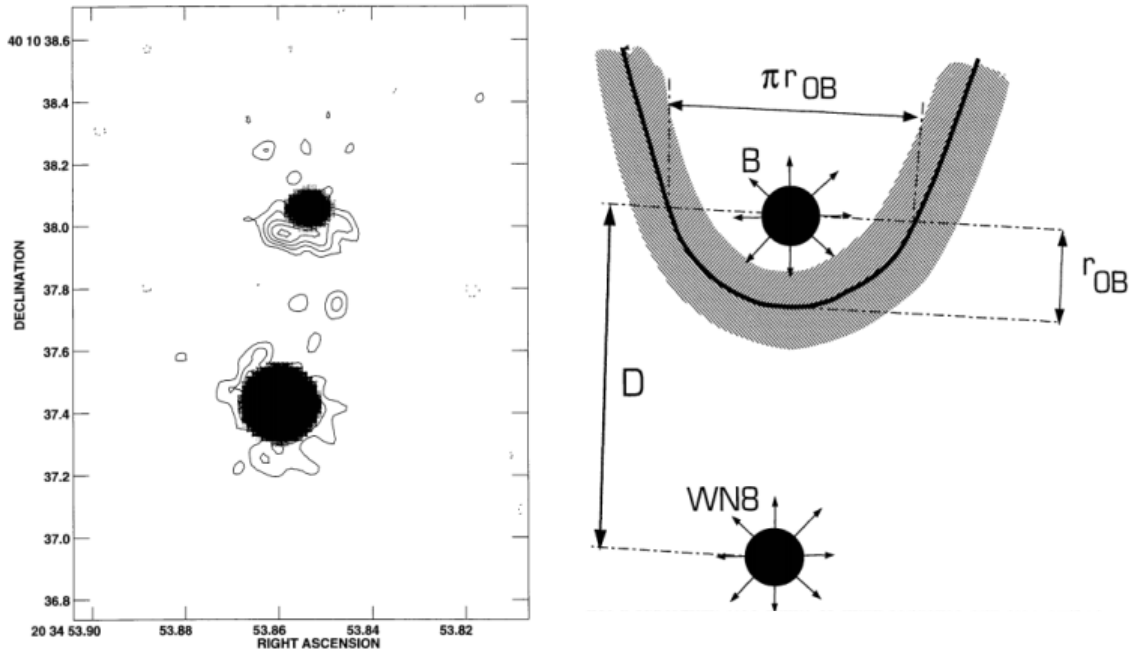


Figure 3.2: Left: radio image of WR 147 (contours) with the peak position of the thermal emission, which is believed to be the stellar wind of the WR star (the bottom one). The upper component corresponds to a non-thermal emission region that is in the location of the wind momentum balance. The right figure is a sketch of the system. Figure source: Williams, Dougherty, Davis, van der Hucht, Bode, & Setia Gunawan (1997).

3.2 Observations of colliding winds

Typical spectra from massive stars with winds contain continuum and free-free emission excess from the photoionized wind, both of brightness temperature of the order of $10^4 K$. Some stars have been noted to have different properties, that could be associated with brightness temperatures of $10^6 - 10^7 K$ and typical non-thermal power-law spectra of synchrotron emission, which would require the presence of relativistic electrons. These spectra would also show temporal variability (e.g. Abbott et al., 1984).

Later [van der Hucht et al. \(1992\)](#) connected the occurrence of non-thermal emission in some of the Wolf-Rayet stars with the fact that they were components of binary systems and proposed that such spectral component could actually come from the interaction of the stellar winds. These observational evidence has resulted in the model by [Eichler & Usov \(1993\)](#) (described in previous section).

The first observational confirmation of these models was achieved by [Williams et al. \(1997\)](#), who were able to spatially resolve the WR 147 system that consists of a Wolf-Rayet star and an O star, depicted in Fig. (3.2). Currently most of the Wolf-Rayet stars with non-thermal spectral component have been found to reside in binary systems ([Dougherty & Williams, 2000](#)). The disadvantage of the WR 147 system is that it has a very long orbital period (order of hundreds of years), thus other predicted CWB properties cannot be observed. For closer studies a system of shorter orbital period and highly eccentric orbit should be used. These conditions are met by WR 140, which is a binary of a Wolf-Rayet star and an O star. It has become a textbook example of a CWB. It exhibits temporal variability in the near-IR, radio and X-rays regimes ([Williams et al., 1990](#)). The distance between the stars varies approximately between 2AU and 30AU. Similar behavior is recurrent over consecutive orbits (the system's period is 7.9 years), meaning that the particle acceleration mechanisms are governed by orbital parameters. Observations of this system are presented in Fig. (3.3)

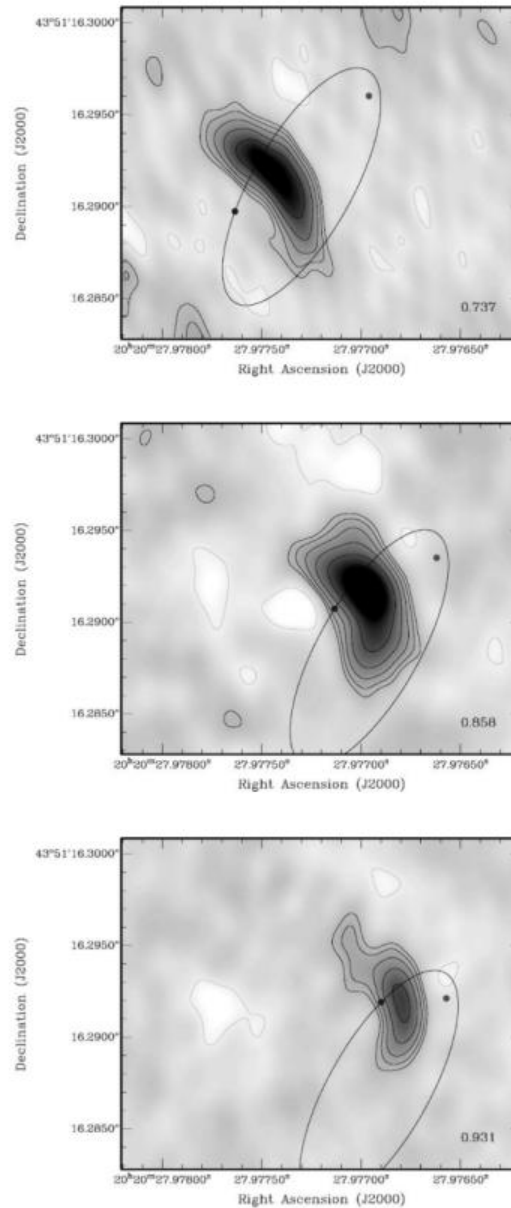


Figure 3.3: Radio observations of WR 140 at different orbital phases with overplotted orbit. The WR star is to the right. One can see the changing structure of the wind collision region. Figure source: [Dougherty et al. \(2005\)](#).

with an explanatory scheme shown in Fig. (3.4).

More binary systems with colliding winds capable of accelerating particles (so called PACWB – particle accelerating colliding-wind binaries) have been observed. [De Becker & Raucq \(2013\)](#) give a comprehensive list of 43 such objects with measured orbital and physical properties as well as detection in radio, X-rays and possibly γ -rays (for now only one system has been detected in this band). They explore the parameter space of observed binaries concluding that particle acceleration should be a common phenomenon among CWBs (especially since many systems' non-thermal radiation might be below current observational thresholds).

We see that there is a strong observational evidence confirming the theory of colliding wind binaries and their capabilities of accelerating particles. It should also be acknowledge that recently observation of strong, organized magnetic fields in the colliding-wind binary system HD 47129 has been reported by [Grunhut et al. \(2013\)](#), which is a system consisting of two O type stars. The measured polar strength of the secondary component is $2850 \pm 500\text{G}$, and the derived upper limit of the primary's surface field is 230G . In addition, the secondary is the most rapidly rotating massive star currently known. They find that the magnetic fields have a simple, almost perfectly dipolar structures. It is also noted by the authors that due to the small orbital distance, this system might not be a classical CWB, as its properties can be explained otherwise.

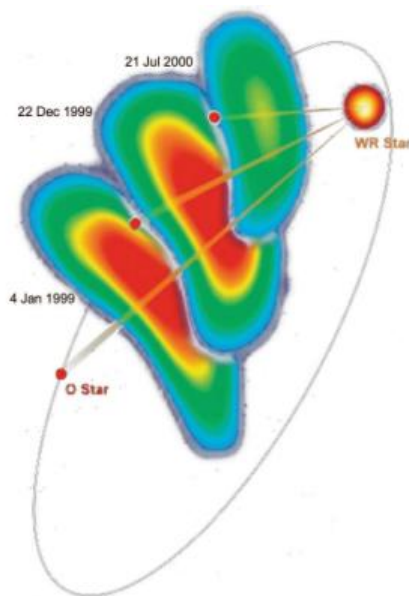


Figure 3.4: Composition of observations of WR 140 seen in Fig. (3.3) demonstrating the changes in the structure of the wind collision region as the orbital motion of stars progresses. Figure source: [Dougherty \(2010\)](#).

3.3 Hydrodynamical models

In order to understand the wind structure of CWBs a number of numerical simulations has been performed. They solve the hydrodynamical equations and usually incorporate gravity, the line-driving force and radiative cooling. That give the following set of equations:

$$\frac{\partial \varrho}{\partial t} + \nabla \cdot (\varrho \mathbf{v}) = 0, \quad (3.3a)$$

$$\frac{\partial \varrho \mathbf{v}}{\partial t} + \nabla \cdot (\varrho \mathbf{v} \mathbf{v} + p) = \varrho \mathbf{f}, \quad (3.3b)$$

$$\frac{\partial \varrho \varepsilon}{\partial t} + \nabla \cdot [(\varrho \varepsilon + p) \mathbf{v}] = \left(\frac{\varrho}{m_H} \right)^2 \Lambda(T) + \varrho \mathbf{f} \cdot \mathbf{v}, \quad (3.3c)$$

where we follow the notation from previous chapters. Here ε is the total specific energy, that is expressed as:

$$\varepsilon = \frac{\mathbf{v}^2}{2} + \frac{e}{\varrho}, \quad e = \frac{p}{\gamma - 1}, \quad (3.4)$$

where e is the internal energy density that can be related to the thermal pressure via ideal gas equation of state with the adiabatic factor γ . $\Lambda(T)$ is the radiative cooling term that is often used in tabulated form. \mathbf{f} stands for the force per unit mass and here consists of gravity and the radiation acceleration.

Additionally such codes employ a separate ray-tracing method that solves the radiative transfer equations producing synthetic X-ray spectra and light curves enabling direct comparison with observations (e.g. [Pittard & Dougherty, 2006](#)).

Since a number of such schemes exist, we will address a particular one. [Parkin & Gosset \(2011\)](#) perform modeling of a massive WR+O binary WR 22. Their simulation shows a colliding-wind region for all orbital phases, although it is disrupted by the dominant WR wind when the two components are at their closest. Their artificial X-ray spectra do not match well to the observations. They conclude that the stellar and the wind parameters derived from observations might not be good enough to properly reproduce the spectra. Sample density and temperature maps can be seen in Fig. (3.5).

3.4 Shocks and particle acceleration

Particles in an ordinary gas transfer energy and momentum by colliding with each other and directly interacting. Shocks in astrophysical plasmas are very different. Plasmas in the Universe are mostly collisionless, which means that the Coulomb interactions are so seldom that they are

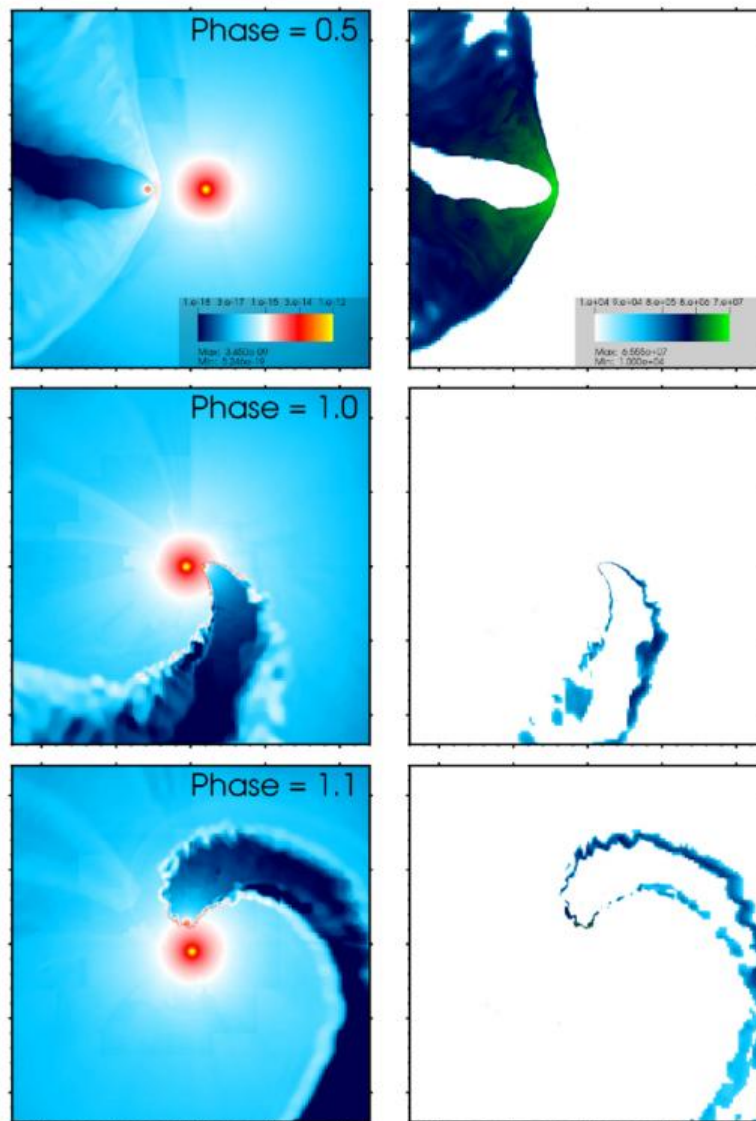


Figure 3.5: Density (left) and temperature (right) maps in the orbital plane for different orbital phases of a massive WR+O binary WR 22. Figure source: [Parkin & Gosset \(2011\)](#).

negligible. Instead the particles can interact indirectly via plasma waves. Hence the magnetic and electric fields are involved in all sorts of different interactions with plasma particles. Let us now look closer at one of these, shocks, in particular those forming in the collision region of wind-colliding binaries.

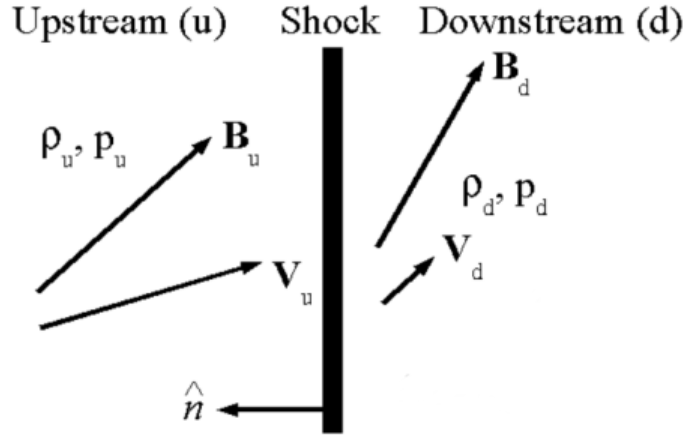


Figure 3.6: Geometry of a shock in its reference frame. Particles are crossing from the upstream to the downstream side. Respective physical quantities are noted together with \hat{n} , the shock normal.

A shock is a form of discontinuity, where the basic physical quantities describing the plasma change very rapidly. A canonical way of describing such system is by introducing a stationary shock and a flow of particles passing through it. The flow that has not crossed the shock yet is called upstream, and the one that has - downstream. The shock normal is a unitary, direction vector normal to the shock surface in the direction of the upstream flow. A sketch of this system is presented in Fig. (3.6).

The stationary shock jump conditions express the relation between upstream and downstream plasma properties (known as Rankine–Hugoniot conditions). They result from the conservation of mass, momentum and energy and follow the MHD equations. The conserved quantities are expressed in equations 3.5-3.10. Please note that a standard convention is used where $[X]$ denotes the difference of the upstream and downstream values of quantity X : $[X] = X_u - X_d$, and that the subscripts n and t relate to the components normal and tangential to the shock normal respectively.

$$[\rho v_n] = 0 \quad (3.5)$$

$$\left[\rho v_n^2 + p + \frac{B^2}{2\mu_0} \right] = 0 \quad (3.6)$$

$$\left[\rho v_n v_t - \frac{B_n B_t}{\mu_0} \right] = 0 \quad (3.7)$$

$$\left[\rho v_n \left(\frac{v^2}{2} + \frac{\gamma}{\gamma - 1} \frac{p}{\rho} \right) + v_n \frac{B^2}{\mu_0} - \frac{B_n}{\mu_0} \mathbf{v} \cdot \mathbf{B} \right] = 0 \quad (3.8)$$

$$[B_n] = 0 \quad (3.9)$$

$$[v_n \mathbf{B}_t - B_n v_t] = 0 \quad (3.10)$$

We shall not go into detail of deriving the above equations, but let us draw some conclusions. For instance, 3.5 tells us that if the shock slows down the flow, then the downstream density will increase. Equations 3.6 and 3.7 result from the conservation of the normal and tangential momenta respectively. Equation 3.8 is the conservation of energy under the assumption of adiabaticity (γ being the adiabatic constant), where the first two terms represent the kinetic energy of the flow and its internal energy. The last two terms correspond to electromagnetic energy flux in the ideal MHD case (meaning, among other things, no macroscopic electric fields). 3.9 follows the condition of the magnetic field being divergence free, and 3.10 results from the Faraday law.

The above set of equations can describe not only shocks but also MHD discontinuities, such as contact, tangential or rotational discontinuities. In fact, in the wind collision region we do have a contact discontinuity, where the two winds meet after crossing their respective shocks. Such case follows Rankine–Hugoniot equations and the following additional condition:

$$\text{Contact discontinuity: } v_u = 0, \quad \mathbf{B}_n \neq 0. \quad (3.11)$$

This means that density the jump is arbitrary, but all other physical quantities are continuous across the discontinuity. Such solution is not a shock though because it has zero upstream velocity, and shocks require flow through their surface. Shocks can now be divided depending on the orientation of the magnetic field with respect to the shock normal:

$$\text{Parallel shock: } \mathbf{B}_t = 0. \quad (3.12a)$$

$$\text{Perpendicular shock: } \mathbf{B}_n = 0. \quad (3.12b)$$

$$\text{Oblique shock: } \mathbf{B}_n \neq 0, \mathbf{B}_t \neq 0. \quad (3.12c)$$

The angle between the shock normal and the magnetic field is called θ_{Bn} , with $\theta_{Bn} = \angle(\hat{\mathbf{n}}, \mathbf{B})$. If it is greater than 45° (but smaller than 90°), the shock is usually called quasi-perpendicular, and quasi-parallel if it is smaller than 45° . In the case of parallel shocks the magnetic field does not change, but in the perpendicular case, both plasma pressure and magnetic field strength increase in the post-shock region. For oblique shocks the general description is more complicated, since

they subdivide into further classes of possible solutions. Most astrophysical shocks fall in the fast shock mode, where the field strength increases, but only in the tangential component (since the jump conditions keep the normal component constant across the shock), which effects in the downstream field bending towards the shock surface. This is depicted in Fig. (3.7).

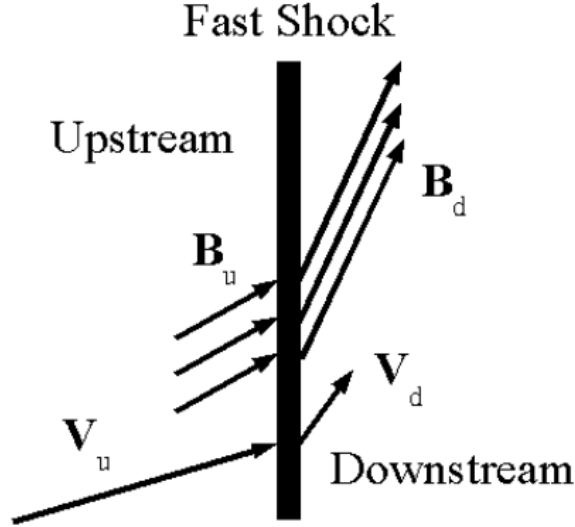


Figure 3.7: Fast shock and its effect of bending the magnetic field toward the shocks surface, as the normal magnetic field component is kept constant. Please refer to the text for more detail.

The most important feature of the shocks might be their capability of accelerating particles, where one considers particles that are being reflected by 'magnetic mirrors' (irregularities, turbulences) between the two sides of the shocks, gaining energy each time they would cross it. The idea was further developed (e.g. [Blandford & Ostriker, 1978](#)) and the mechanism called Diffusive Shock Acceleration (DSA) allowing particles to cross the shock multiple times was introduced. This iterative process produces power law energy spectra of relativistic particles:

$$N(E) \propto E^{-n}, \quad n = \frac{r+2}{r-1}, \quad (3.13)$$

where r is the shock compression ratio: $r = \frac{\rho_d}{\rho_u} = \frac{v_u}{v_d}$.

This mechanism is believed to be the source of cosmic rays, that are accelerated on astrophysical shocks across the Universe. This process can in principle also allow the shocks in CWBs to accelerate particles. As discussed in section 3.2, synchrotron radiation that requires population

of relativistic electrons has already been observed in many massive binaries. That gives us good indication that particle acceleration is in fact taking place in the wind collision region and is not negligible.

The distinction between parallel and perpendicular shocks comes into play when we consider the motion of charged particles within the magnetic field. In particular, the magnetic field orientation should have some influence on the processes of particle acceleration. For instance, the diffusion coefficient depends on the angle between the shock normal and the magnetic field:

$$\kappa = \kappa_{\parallel} \cos^2 \theta_{Bn} + \kappa_{\perp} \sin^2 \theta_{Bn}, \quad (3.14)$$

where κ_{\parallel} and κ_{\perp} are the coefficients parallel and perpendicular to the magnetic field respectively. The energy spectrum to first order does not depend on κ , but the acceleration length scale and time scale do (being $\frac{\kappa}{u}$ and $\frac{\kappa}{u^2}$, where u is the characteristic flow speed). To give some examples of possible effects of magnetic field orientation: quasi-parallel shocks are believed to be able to boost acceleration of low energy particles, while quasi-perpendicular shocks are found overall to be few orders of magnitude faster in particle acceleration (Ostrowski, 1988), but less capable of injecting the particles into the acceleration process (Ellison et al., 1995). Apart from that, recent simulations of particle acceleration at shocks in the solar corona with magnetic fields changing across the shock (e.g. Pomoell et al., 2011; Sandroos & Vainio, 2006) point at much more complicated dependencies and the need of further studies.

In conclusion, investigating both the strength and geometry of the magnetic field in the wind collision region is important for two reasons. It would allow for better estimates of non-thermal radiation and for studies of particle acceleration and possible partaking in cosmic ray production, improving the simulations as e.g. Reitberger et al. (2014a).

Modeling

Before discussing the results of our modeling we present the simulation setup. Here we discuss briefly the tools used and the procedures followed.

4.1 The code

In order to simulate the CWBs we use the CRONOS code (Kissmann et al., 2008; Kleimann et al., 2009), which is solving the equations of ideal magnetohydrodynamics. It uses a one-fluid model and solves the following, dimensionless set of conservation equations:

$$\frac{\partial \varrho}{\partial t} + \nabla \cdot (\varrho \mathbf{v}) = 0, \quad (4.1a)$$

$$\frac{\partial \varrho \mathbf{v}}{\partial t} + \nabla \cdot \left[\varrho \mathbf{v} \mathbf{v} + \left(p + \frac{|\mathbf{B}|^2}{2} \right) \mathbf{1} - \mathbf{B} \mathbf{B} \right] = \varrho \mathbf{f}, \quad (4.1b)$$

$$\frac{\partial e}{\partial t} + \nabla \cdot \left[\left(e + p + \frac{|\mathbf{B}|^2}{2} \right) \mathbf{v} - (\mathbf{v} \cdot \mathbf{B}) \mathbf{B} \right] = \left(\frac{\varrho}{m_H} \right)^2 \Lambda(T) + \varrho \mathbf{f} \cdot \mathbf{v}, \quad (4.1c)$$

$$\frac{\partial \mathbf{B}}{\partial t} + \nabla \times \mathbf{E} = 0. \quad (4.1d)$$

Let us recall all the quantities used in the equations above: ϱ is the mass density, \mathbf{v} is the fluid velocity, \mathbf{B} and \mathbf{E} are the magnetic and electric fields, p is the thermal pressure and e is the total energy density. The source terms on the right side are additional forces that could be applied to the system: in our case \mathbf{f} is the force term that contains the gravitational acceleration and the CAK-approximated radiative acceleration (see section 1.3.2). Moreover we include a radiative cooling term, which is described by function $\Lambda(T)$, which we take from Schure et al. (2009), where detailed tables of $\log T$ - $\log \Lambda$ calculated by plasma emission programs are provided.

The system of equations 4.1 is not sufficient to determine all the physical quantities. Therefore

Table 4.1: Summary of normalization constants for physical quantities used in our simulations.

| Quantity | Symbol | Physical unit | Numerical value |
|--------------------|-------------|---|-----------------------------|
| Mass | m_0 | M_\odot | $1.98855 \cdot 10^{30}$ kg |
| Density | ϱ_0 | - | 10^{-8} kg/m ³ |
| Length | L_0 | R_\odot | $6.955 \cdot 10^8$ m |
| Temperature | T_0 | - | 10^4 K |
| Velocity | v_0 | $c_s = \sqrt{\frac{2k_b T_0}{m_p}}$ | 11.7 km/s |
| Time | t_0 | $\frac{L_0}{v_0} = \frac{L_0}{c_s}$ | 0.7 days |
| Magnetic induction | B_0 | $\sqrt{\varrho_0 \mu_0} v_0 = \sqrt{\varrho_0 \mu_0} c_s$ | 13.1 G |

additional closing relations are provided:

$$e = \frac{\varrho |v|^2}{2} + \frac{|\mathbf{B}|^2}{2} + \frac{p}{\gamma - 1}, \quad (4.2a)$$

$$\mathbf{E} + \mathbf{v} \times \mathbf{B} = 0, \quad (4.2b)$$

$$\nabla \cdot \mathbf{B} = 0. \quad (4.2c)$$

We see that the total energy density consists of a kinetic, a magnetic and a thermal part. We set $\gamma = 5/3$, which is the adiabatic index for a monoatomic gas. The code solves the equations in numerical units, the normalization of which is set by the user. Table 4.1 presents our choice of the four independent normalization constants: mass, density, length and temperature. For all the quantities normalization can be computed directly from these basic four.

The code provides a choice of cylindrical, spherical and Cartesian grids. For a single star a spherical grid is extremely convenient, since functions depend on radius and are therefore easily prescribed. For simulating colliding wind binaries, where we deal with two stars, it is more suitable to use the Cartesian grid. This imposes several technical difficulties, which will be mentioned later on.

On the technical side, CRONOS is an object-oriented, MPI parallel code written in C++. It saves the data to the HDF5 binary data format, which we then process using Python (Hunter, 2007) and its numerous libraries. The user has to define a module file that contains the geometrical set up and the initial conditions, as well as the source terms that will be included in the MHD equations. In the next section we describe this procedure in case of our simulations.

4.2 The setup

In the Cartesian grid we choose the x -axis to be the main axis of the system, on which both stars' centers will lie (meaning that the orbital separation can be expressed in the distance on this particular axis). In order to prescribe the initial conditions, we divide the domain using the stellar parameters and following eq. (3.2) estimate the shocks position based on the momentum flux ratio of the two winds. On each side we prescribe initial velocity, density, magnetic field and temperature respective for a single star. Velocity is initialized as zero inside the stars, and outside using the β -law:

$$v^i(r) = v_\infty^i \left(1 - \frac{\xi R^i}{r} \right)^{\beta^i}, \quad (4.3)$$

where i denotes the star and ξ is a parameter that is adjusted to counteract problems with continuous wind acceleration caused by the finite grid size. An exemplary initial velocity field is presented in Fig. (4.1), where one can also see how the computational domain is divided. The density is initialized as 1 inside both stars and then is assumed to decrease as $\sim \left(\frac{R^i}{r}\right)^2$. The temperature prescribed where the stars are located depends on the stellar parameters we choose (for the ones used in the simulations please refer to Table (4.2)). Everywhere else it is set to the constant value of the temperature normalization. The line-driven winds are not perfectly isothermal, but the order of magnitude of temperature does not change in the undisturbed wind, since we assume it to be coupled to the star's photosphere (e.g. Pittard & Parkin, 2010). This makes it then a reasonable initial condition.

Some amount of grid cells around each star (~ 10) are kept constant during the simulation (meaning no changes in physical quantities) in order for a proper (physical) acceleration of the wind over time.

The most challenging part is prescribing the initial conditions for the magnetic field. It has to be done in a way, that does not produce nonzero divergence and does not lead to numerical (not physical) heating of the gas as the simulation progresses. The first issue can be solved in two ways. The so-called 'divergence cleaning' techniques can be used, which prescribe an artificial non-zero divergence field where the $\nabla \cdot \mathbf{B} \neq 0$ part is subtracted to obtain a divergence-free magnetic field. The methods we have tried to employ have not yielded satisfactory results and were not further investigated.

The issue can be avoided, if we prescribe the magnetic field using a vector potential \mathbf{A} , such that:

$$\mathbf{B} = \nabla \times \mathbf{A}. \quad (4.4)$$

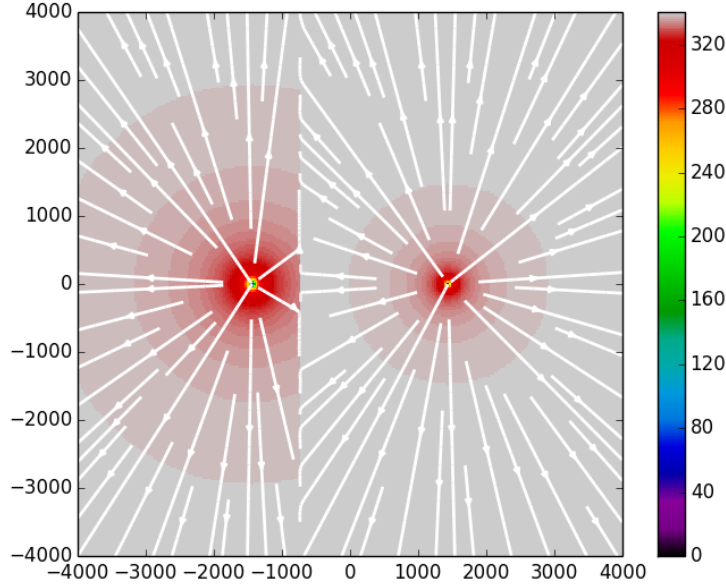


Figure 4.1: Initial conditions for the velocity field in the xz -plane. The star on the left is the B-type star, and the one of the right is the Wolf-Rayet star. Table 4.2 lists their stellar parameters. The colors denote the speed (in the simulation units, cf. Tab. 4.1), and the arrows present the velocity direction. We see a steep acceleration near the stars and a radial outflows from both components. The spatial scales, as explained in Table 4.1, are expressed in solar radii.

This is a nontrivial task, especially since we operate on a Cartesian grid, while the magnetic field of a spherically symmetric star would be prescribed easier in spherical coordinates. For the time-being we restrict ourselves to dipolar magnetic fields, expressed by the following vector potential and resulting field:

$$\mathbf{A}(\mathbf{r}) = \frac{\mu_0}{4\pi} \frac{\mathbf{m} \times \mathbf{r}}{r^3}, \quad (4.5)$$

$$\mathbf{B}(\mathbf{r}) = \frac{\mu_0}{4\pi} \left(\frac{3\mathbf{r}(\mathbf{m} \times \mathbf{r})}{r^5} - \frac{\mathbf{m}}{r^3} \right) \quad (4.6)$$

where m is the dipole moment. We allow for the dipole moments to have arbitrary orientations. The user can prescribe the strength of the dipole by choosing the magnetic induction at the star's surface either on the equator or the pole (for the dipol follows: $B_{pol} = 2 \cdot B_{eq}$). The resulting initial prescription of the magnetic field can be seen in Fig. (4.2). In this particular case both dipoles have the same polar strength of $B_{pol} = 200G$, but the field decrease also scales inversely with stellar

radii, so for the bigger B-star (the left part of the computational domain) it will decrease slower than for the smaller WR star (see Table 4.2 for comparison of stellar parameters).

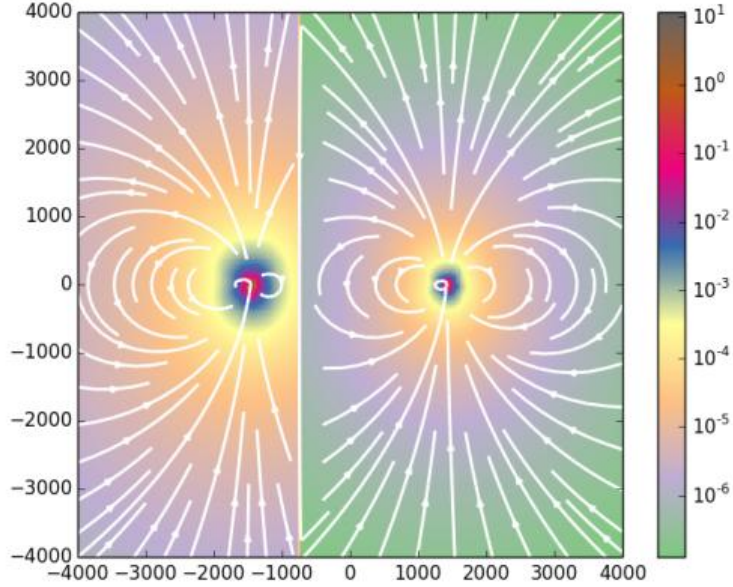


Figure 4.2: Initial conditions for the magnetic field in the xz -plane. The background map depicts magnetic field strength (in numerical units, cf. Table 4.1, also note the logarithmic scale). Both dipole moments are oriented upwards in the z -direction. The arrows follow magnetic field lines, where the dipolar structure is clearly visible in both cases. Again, the spatial scales, as explained in Table 4.1, are expressed in solar radii.

A dipole field and a dipole potential obviously have a singularity in the center of the star. This has been removed by extrapolating the vector potential at the very inner parts of the star. Several schemes were tried out, since this is a highly non trivial case: not only the field's strength should not blow up in the center, but there has to also be a smooth transition of the vector field from the extrapolated region outwards, prescribed by an appropriate vector potential. In the end we adopted a formula following [Low & Tsinganos \(1986\)](#) up to a radius $R_{in} \sim 0.2R$:

$$\mathbf{A}(r) \simeq \frac{\mathbf{m} \times \mathbf{r}}{R_{in}^2} \left[5 \left(\frac{r}{R_{in}} \right) - 9 \left(\frac{r}{R_{in}} \right)^3 + 5 \left(\frac{r}{R_{in}} \right)^4 \right]. \quad (4.7)$$

The second issue is much more severe. The strong gradients (quantity change per cell) of

magnetic field strength cannot be reproduced by a second order code with finite resolution (such as the CRONOS or other currently used codes). Thus, numerical dissipation produces spurious heating, that is unphysical and can lead to the wind having similar temperature as the collision region. This was dealt with by keeping all plasma properties constant close to the star, which however can produce other unwanted effects. Firstly, the effective magnetic field will be much weaker than it would be if we did not prescribe extra fixed cells, because we let it decrease like a dipole ($\sim 1/r^3$) where in the case of the weak field it should decrease much slower (a more extensive discussion is given in the next chapter, in particular Figs. (5.5), (5.4) and (5.6)). Furthermore, we found that such a procedure can produce artificial current sheets. We tried to find a compromise between the occurrence of those numerical errors, being able to prescribe strong magnetic fields and avoiding the artificial, numerical gas heating.

Table 4.2: Stellar parameters for stars used in simulations.

| | $M[M_{\odot}]$ | $R[R_{\odot}]$ | $T[10^4\text{K}]$ | $L[L_{\odot}]$ | $\dot{M}[M_{\odot}/\text{yr}]$ | $v_{\infty}[\frac{\text{km}}{\text{s}}]$ |
|----|----------------|----------------|-------------------|------------------|--------------------------------|--|
| B | 30 | 20 | 2.3 | 10^5 | 10^{-6} | 4000 |
| WR | 30 | 10 | 4 | $2.3 \cdot 10^5$ | 10^{-5} | 4000 |

We chose to run our simulations for the same system as discussed in [Reitberger et al. \(2014b\)](#), which consists of a B and WR star of flux ratio $\eta = 0.1$. In our study we vary the orbital separation, magnetic field strength and spatial orientation of the dipole magnetic moment. Table 4.2 lists the stellar parameters used in this work.

The simulation runs until it converges to a steady state solution. Note that because we did not introduce any motion (stellar rotation or orbital motion), we expect to get a stationary flow.

Results - single simulations

Using the theory behind the stellar winds (Chapter 1), and current observational and computational indications on magnetic fields of massive stars (Sections 2.2.1 and 2.2.2) we now try to simulate the real systems to the best of our knowledge using the tools and methods described in Chapter 4. Here we present the simulations and discuss the quantitative and qualitative results we were able to obtain.

We always prescribe the dipole moments in the xz -plane, therefore all 2D plots are shown for this plane as well, since this is where the magnetic field will have the most diverse structure. All plots are done in the simulation units (cf. Tale 4.1), unless otherwise specified.

5.1 Simulations of a single massive star

We start by investigating a single massive star with a magnetic field, in which case we are not interested in the collision region. Therefore we can use the isothermal equation of state ($\gamma = 1$), which means keeping the temperature constant throughout the numerical domain. As mentioned in the discussion of numerical setup (section 4.2), the line-driven winds are nearly isothermal, making this a good approximation. This allows us not to worry about the artificial, numerical heating anymore.

Let us recall the equatorial magnetic field confinement parameter from Section 2.2.2 (Equation (2.10):

$$\eta_{eq}(r) = \frac{B_{eq}^2 R^2}{\dot{M} v_\infty}. \quad (5.1)$$

For all configurations we use in the binary simulations, this parameter is very small (of the order of $10^{-3} - 10^{-1}$), meaning that the plasma outflow carries the field out with it. Here we perform two simulations for a magnetic field confinement parameter $\eta_{eq} \sim 4$ and $\eta_{eq} \sim 10$ (though the effective parameters are smaller due to the fixed cells around the stars). Such highly magnetized stars are not featured in our current simulations for binary systems, but shall be included in the future work. Results for both setups are presented in Fig. (5.1). Both cases are the same B-type stars, where the left one has a polar magnetic field strength $B_{pol} = 1000\text{G}$ and the right one

$B_{pol} = 1500\text{G}$, which are consistent with observations of magnetic fields in B stars. The resolution (the cell's physical size) is set to be the same as for the simulations of binary systems (which sets the ground for future binary simulations including such stars). The figures represent the magnetic field, the density and the velocity field with respective streamlines. We see that in both cases the magnetic field loses its dipolar character far from the star and creates a current sheet in the equatorial plane. We also see that the density and the velocity are no longer spherically symmetric. For the medium magnetic confinement parameter (left panels) the magnetic field seems to have directed the plasma flow near the equatorial plane, where it is reflected by the increased density and velocity. The strong parameter case increases the velocity only near the equatorial plane, where the density is also increased. Both cases show asymmetries in the wind velocity profiles. We are not sure if this is a physical effect as we see no indications of similarly structured phenomena that could be responsible for that.

It is interesting to look closely at what is going on near the star, as depicted in Fig. (5.2). The strong magnetic field produces closed loops in the vicinity of the star, which are not able though to pull the plasma back on the surface (which is confirmed by examining the velocity direction). In the medium confinement case the plasma has pushed out of the loops, but it does retain higher field strength near the equator, which causes an increase in density and velocity. This seems to be in agreement with simulations by [ud-Doula & Owocki \(2002\)](#) that are discussed in Section 2.2.2, though we did not use as high resolution and explored the confinement parameter space.

In the cases described above we were able to prescribe strong magnetic fields since we were using the isothermal equation of state. In the binary simulations, we do not restrict ourselves like that and thus use lower fields (up to $B_{pol} = 400\text{G}$ only). It is easier to study the properties of only the stellar magnetic fields if we run a single star simulation, for both the B and the WR star. We use the same simulations resolution and physical parameters as in simulations of binary systems, which allows us to compare the magnetic fields they produce with the theoretical predictions and extend the findings to simulations of binary systems.

In some configurations we saw two artificial current sheet-like structures created near the equatorial plane, depicted in Figure (5.3). This problem disappears when we double the resolution. Unfortunately due to high time-costs of large resolution simulations, this solution was not possible to apply for the large computational domains we use for simulating binaries within the duration of this master thesis work. It is yet unclear what exactly causes this issue. Keeping smaller number of cells with fixed magnetic field helps to get rid of the artificial current sheets, but then the artificial heating comes into play even for low dipole strengths. The parameter space of this problem has to be investigated further in order to find a suitable setup allowing for stronger magnetic fields.

In Figures (5.4), (5.5) and (5.6) we compare the magnetic field strength with the theoretical

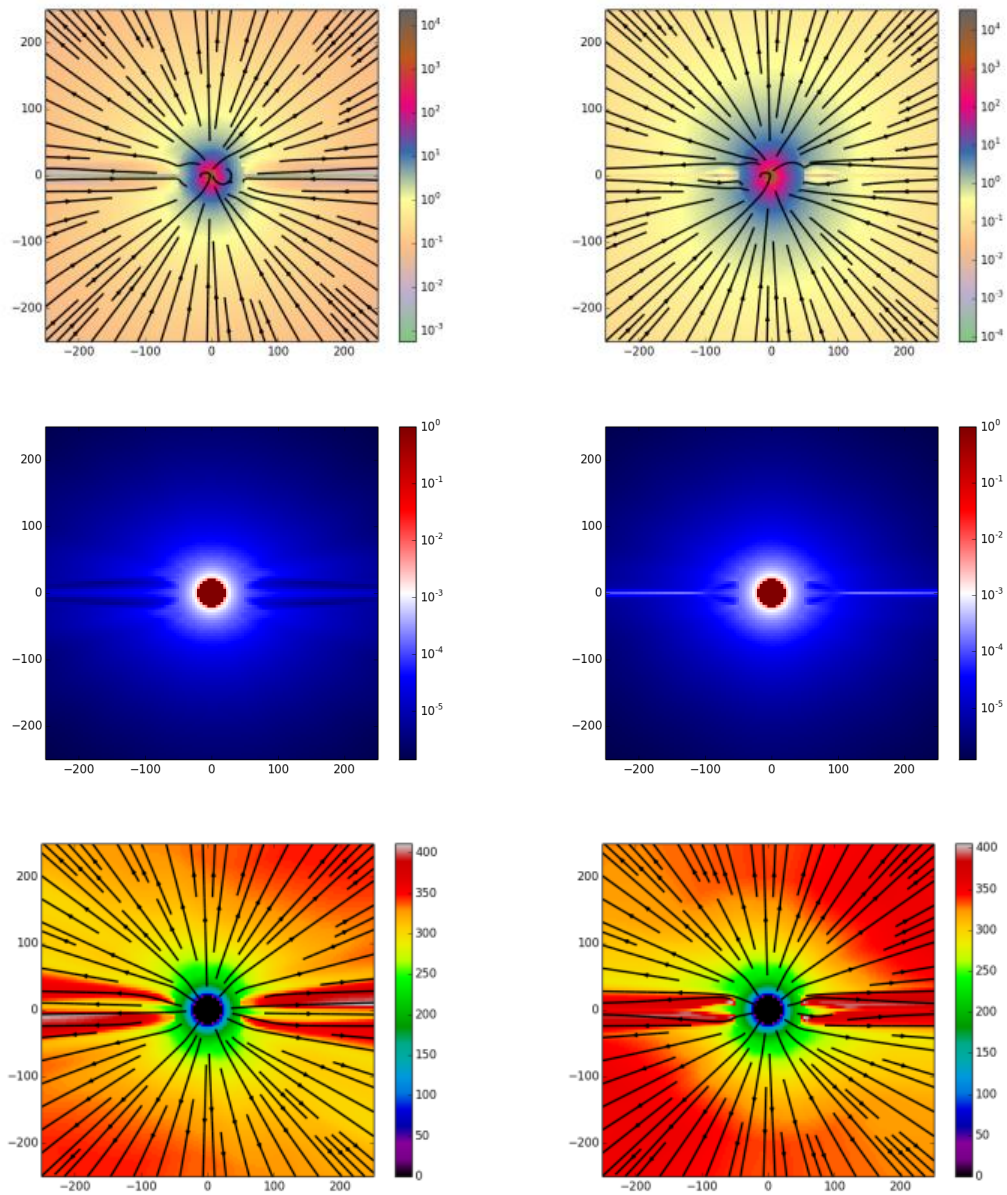


Figure 5.1: Simulation of one massive B star with a magnetic dipolar field and isothermal equation of state. From the top we see: magnetic field strength (log), density (log) and velocity. Left column is for the star of $B_{pol} = 1000G$ and right for $B_{pol} = 1500G$, which corresponds to $\eta_{mag} \sim 4$ and $\eta_{mag} \sim 10$ respectively. Please note that effectively the dipole is weaker than the prescribed one.

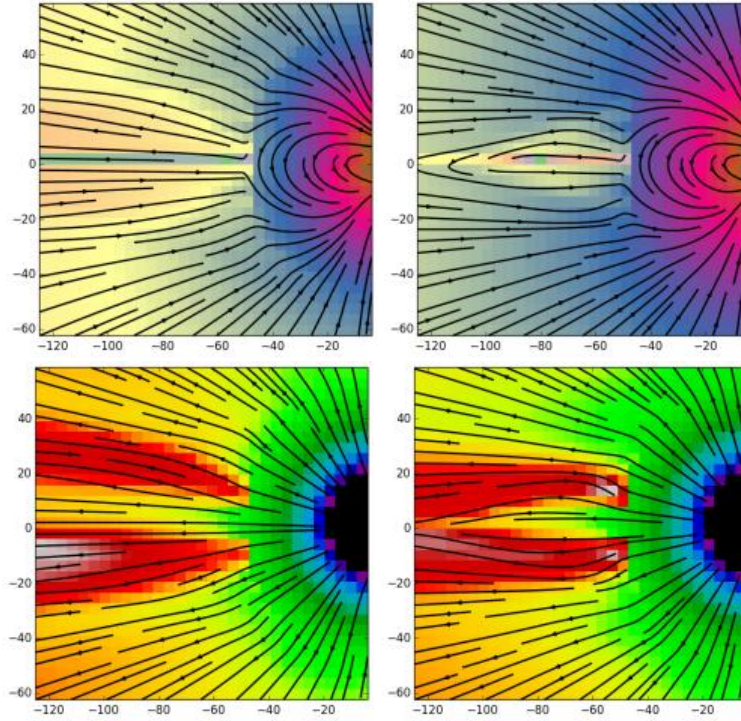


Figure 5.2: Same systems as in Fig. (5.1), but with zoom at the region near the star. The top panels depict the magnetic field, the bottom ones velocity field with respective streamlines.

predictions for the magnetic field from equation 2.6. For our cases (very small Alfvén radii) this means that the field should decrease like a completely radial field (meaning the $\sim 1/r^2$ dependence) outside of the star. We do the comparison for both the B and the WR star, in the direction parallel to the dipole moment, the equatorial plane, and at an angle of 45° between the pole and the equator.

In the direction parallel to the magnetic moment (Fig. 5.4) we see that the B star exhibits stronger field far from the star than what Eichler & Usov (1993) predict (discussed in Section 2.2.2). This simulation was run for $B_{pol} = 500\text{G}$, which the theory predicts to be a strong enough field for the dipolar structure to be preserved on large scales. Thus Usov’s solution follows the dipolar curve. The calculated in our simulation field (green dots) follows the dipolar field only for the number of fixed cells around the star (since this is the region where the initially prescribed field remains), and then starts to decrease almost like radial field (meaning $\sim 1/r^2$ decrease), which we can see by the data points being almost parallel to the plotted $1/r^2$ function (please note that we use logarithmic scales for the field strength. That means that parallel lines have the same exponential dependencies).

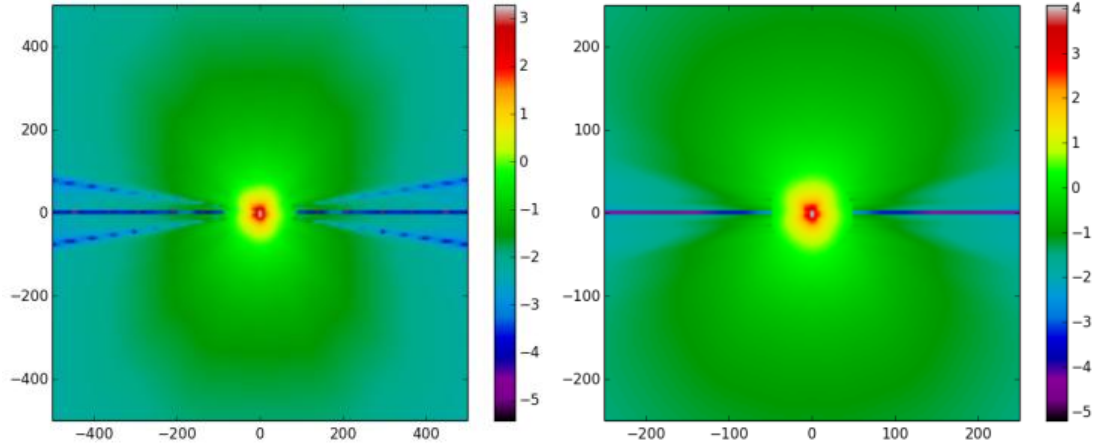


Figure 5.3: B star with surface strength $B_{pol} = 500G$, calculate with two different spatial resolutions (left: $7.8R_{\odot}/\text{cell}$, right: $3.9R_{\odot}/\text{cell}$). We can see the two artificial current sheet-like structures in the equatorial region that are most probably effects of numerical imprecisions. Please note that the higher precision run covers a smaller part of the domain.

The WR star (with $B_{pol} = 250G$) follows the dipole field within the fixed region and then smoothly starts to decrease in the $\sim 1/r^2$ way (slower than a dipole field). Here the effect of the number of fixed cells on the effective field strength is very visible. A large fixed region forces the field to decrease fast, and then when it can start to be of radial type, it has much lower strength than it would have if it had started to be radial closer to the star. In this particular case we see that this behavior makes exactly one order of magnitude difference, which is rather large (we infer this value from the point where the data and the theoretical curve are parallel and meet the axis). Note that the WR star simulation covers larger distances than the B star, for which we are still quite close to the surface. Thus, the B star's field will probably transition into full radial-like structure further away.

The interpretation of the comparison of the field in the equatorial plane is a bit difficult. Close to the star small magnetic loops can exist, and at larger radii an ideally zero field should prevail. The current sheet, that in reality should be very thin, occupies the smallest possible simulation size of one grid cell (few R_{\odot}). In the case of the WR star we see an even faster than dipolar decrease (by examining the slope). For the B star we also see very fast decrease, but then a surprising increase. This might be due to numerical resistivity and possibly magnetic-reconnection like events that we sometimes observe in other simulations as well. Nevertheless, both fields are very weak, 2-3 orders lower than the radial/Ussov's fields. It has to be noted that such drastic behavior is restricted only to the equatorial plane (usually one grid cell size). In this region none of the theoretical

predictions reproduce what is observed, since all of them neglect the formation of current sheet.

Due to the equatorial plane not being very representative, we also calculate the field at the angle of 45° from the equator and compare it with respective theoretical curves. Quantitatively this situation is very similar to the direction parallel to the magnetic dipole. In the B star we see a field stronger than theory predicts, transitioning between the dipolar and radial regimes. In the case of the WR star we see perfect radial-like field, one order of magnitude smaller than the one predicted by theory. This hints again at how influential the number of fixed cells kept around the star is.

5.2 An exemplary simulation of the CWB system

As an illustration for the formation of the wind collision region, we present time snapshots from one particular simulation in Figures (5.7) and (5.8). The size of the domain is $8000 R_\odot$ and the orbital separation between the stars is $720 R_\odot$. The prescribed polar magnetic fields are $B_{pol}^B = 400\text{G}$, $B_{pol}^{WR} = 200\text{G}$. Other parameters follow Table 4.2. The magnetic field strength time evolution is presented in Fig. (5.7) and the velocity field evolution in Fig. (5.8). We can see how the information about "new" magnetic field propagates through the region with a finite speed radially from the stars. In case of the velocity field evolution, we see how the weaker wind of the B-star is being pushed by the stronger outflow from the WR star, as well as the formation of collision region. Fig. (5.9) presents the converged state for the temperature and the density. Both of these quantities experience a clear jump at the shock. We see that especially the temperature conveniently can be used as a tracer for the collision region, being few orders of magnitude higher than the ambient medium (a fact that we will use later in our analysis).

5.3 Analysis of the collision region

This section presents details of our analysis techniques applied the particular simulation. The aim is for the reader to understand how we arrive at our results in the following chapter.

In this study we are mostly interested in the magnetic field in the collision region and in its immediate vicinity. We identify the shock position and the shock normal using the value of the temperature gradient. As mentioned before (and as seen in the left panel of Fig. (5.9)), the shocks surrounding the collision region are able to heat the plasma so that it reaches temperatures orders of magnitude higher than the ambient wind. This means that the biggest change in temperature (so, its gradient) will happen at the shocks. This is very useful since the gradient is a vector, allowing us not only to identify the shock position, but also its normal. Appropriate gradient thresholds are

set empirically (sometimes multiple values for different regions of the shock). We try to keep the approximate shock width of 3 cells, resulting in numerical simulations (Reitberger et al., 2014b). Regions identified with different thresholds are shown in Fig. (5.10). Apparently it is necessary to manually select an appropriate threshold. In some cases, especially for large computational domains (large grid cell size), some additional non-shock related high gradients will occur in the central part of the collision region, as visible in the top left panel. What we can do then is to set different thresholds in the inner and outer parts of the collision region, creating one combined mask that is later used in the analysis.

To check the validity of this procedure, we present a sample identification of the shocks surrounding the collision region in Fig. (5.11). The middle panel presents the density field, where we cut out the region identified as the shock and present it in the left panel. Indeed, the obtained region does correspond to the physical collision region, and we can clearly see the transition of the physical quantity (here: density) within the shock cells. The right panel presents the vector representation of temperature gradient. We see that this vector field is random in the wind region, but highly organized in the shocks and indeed parallel to their normal.

The shock orientation is important since we are interested in knowing the magnetic field orientation just before the shock (i.e. on the side closer to the star). In particular, as discussed in section 3.4, the angle θ_{Bn} between magnetic field and shock normal can have a large influence on particle acceleration. We are thus interested in the angle just before the shock on its upstream side. We identify the regions just before and after the shock employing another boolean mask in our analysis. It is shown in the Fig. (5.12). The employed color map denotes the angles θ_{Bn} and helps to distinguish between the quasi-parallel and quasi-perpendicular parts of both shocks.

The magnetic field lines at the shocks will look different depending on the system's geometry and the dipole strength of both stars. As a part of our study we focus on the mentioned angle θ_{Bn} and the magnetic field strength in the post-shock region, as they have influence on the particle acceleration, synchrotron emission and electron losses in the collision region. Fig. (5.13) shows different magnetic fields in the collision region for three different setups. On the left panel, two current sheets are able to penetrate the collision region, making the shocks parallel in the equatorial plane. In the middle panel we see that the magnetic field on the right side did not create a current sheet or radial-like lines, being nearly perpendicular to the shock normal near the collision region. The left panel shows on the right side the dipole with magnetic moment lying on the x axis, which extends the quasi-parallel region of the right shock (such behavior is discussed in the following chapter). We mention this to qualitatively explain that changes in magnetic field strength or geometry will produce different shock properties. Quantitatively we explore the matter more by examining results for a broad range of setups presented in the next chapter.

Now we can investigate the properties of the shocks (we shall be using the terminology introduced in the previous chapter, where S1 is the shock closer to the B star, and S2 the one closer to the WR star). To measure the compression ratios of the shocks we need to compare the values on both sides of the shock along its normal. This is achieved firstly by identifying the cells on the upstream side of the shock, and then using the temperature gradient vector (c.f. right panel of Fig. (5.11)) to cross the shock and arrive at the appropriate cell on the downstream side.

Fig. (5.14) presents measured compression ratios for the two shocks in our exemplary simulation. Theory predicts the CWBs shocks to be strong with compression ratio of 4. We see that for the shock on the WR-star's side this is almost achieved everywhere for the density ratio, which is almost constant along the shock. The magnetic field ratio for this shock is between 3 and 4 for the outer parts, but exhibits a strong decrease near the equatorial plane. This cannot be explained by the existence of the current sheet alone, since the phenomenon is much wider. We see exactly the same behavior for the magnetic field compression ratio of the S1 shock. What is very interesting is that the density compression ratio also exhibits a drop near the equatorial plane (though not below the value of 3).

To see if this is the result of the magnetic field's influence, we repeated this simulation without the magnetic field. The comparison for the density compression ratios, as seen in Figure (5.15), reveals that the magnetic field does not influence the density compression ratio. Thus we do not calculate them for cases studied later. The comparison between the hydrodynamical and MHD simulations for this case (we repeated it for 3 different setups, not discussed here) does not yield any differences in the overall shock structure and geometry. This might be due to the low values of magnetic fields used. We discuss this issue later in section 6.3.

We also note that the strong decrease in density compression ratio for the S1 shock near the apex is very different from the hydrodynamical results of [Reitberger et al. \(2014b\)](#) who uses the exact same setup, where the compression ratio rises closer to the apex. The observed magnetic field strength compression ratio is weaker than the density compression ratio.

Another quantity that we are interested in is the magnetic field strength in the collision region. This is important for modeling of the synchrotron emission (as observed for multiple objects, c.f. section 3.2) and synchrotron losses of high energy electrons. Fig. (5.16) presents the values for the exemplary simulation. The values vary up to an order of magnitude along the shocks. What is more, they experience a drop to almost zero near the equatorial plane. This means that the current sheet penetrates the collision region, and its influence is bigger than just one grid cell. What is more we see that the fields have very different magnitudes depending on the respective strengths. Here we use stars with the same order of magnitude surface fields, which is not always the case as observations suggest. This means that it is not correct to use just one magnetic field strength

for the whole collision region, as is done in the literature (Eichler & Usov, 1993), especially since there can be a difference of several magnitudes. As we will show later on, the collision region is clearly divided between the two magnetospheres which do not interact with each other (in other words, the information does not cross the contact discontinuity).

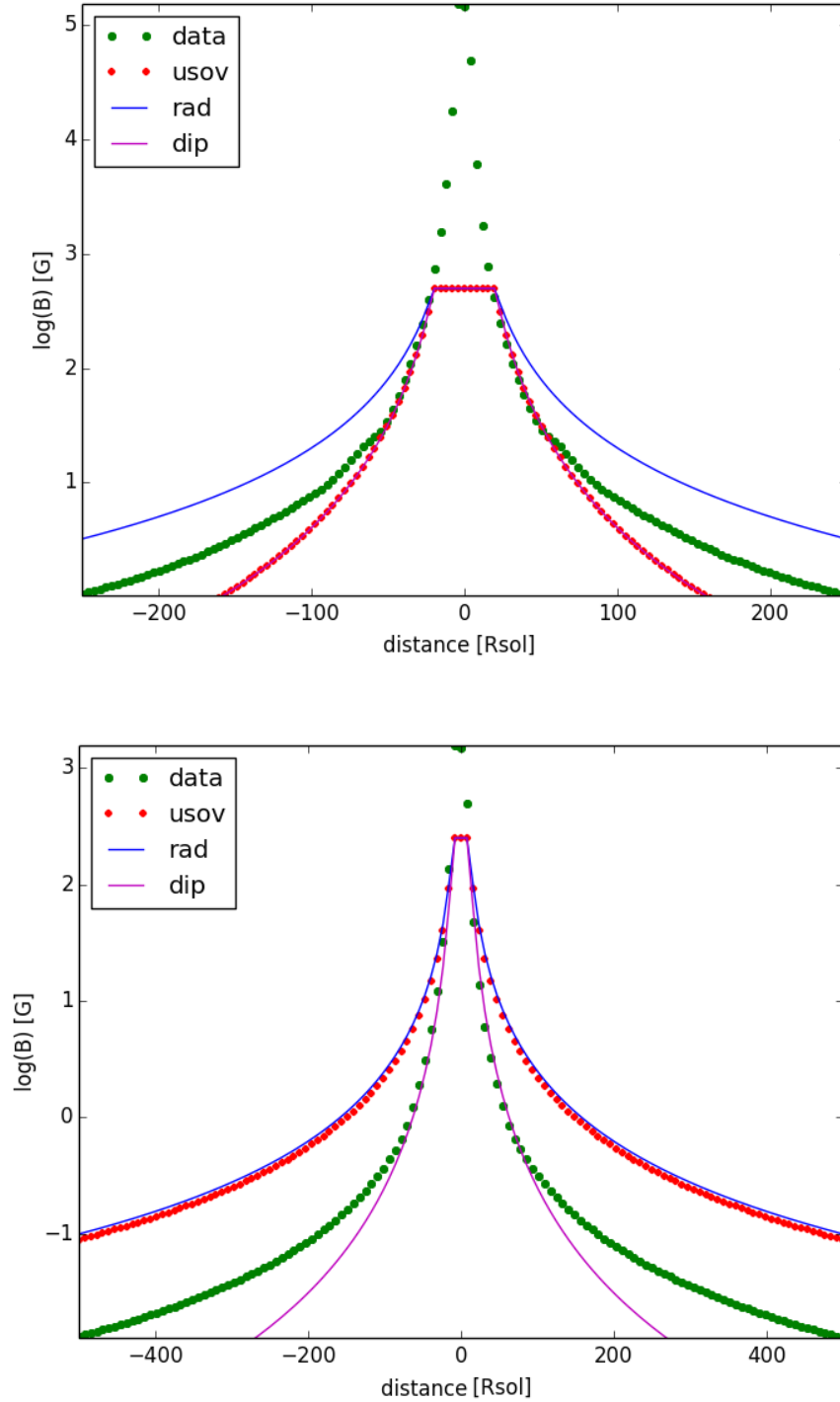


Figure 5.4: Comparison of the numerical and theoretical magnetic field strengths for a single star (top: B star, bottom: WR star) in the plane parallel to the magnetic moment. The green dots are the data points from the simulation, and red ones follow the prescription by [Eichler & Usov \(1993\)](#). We also plot the radial field dependence ($1/r^2$) and the dipole one ($1/r^3$) for reference.

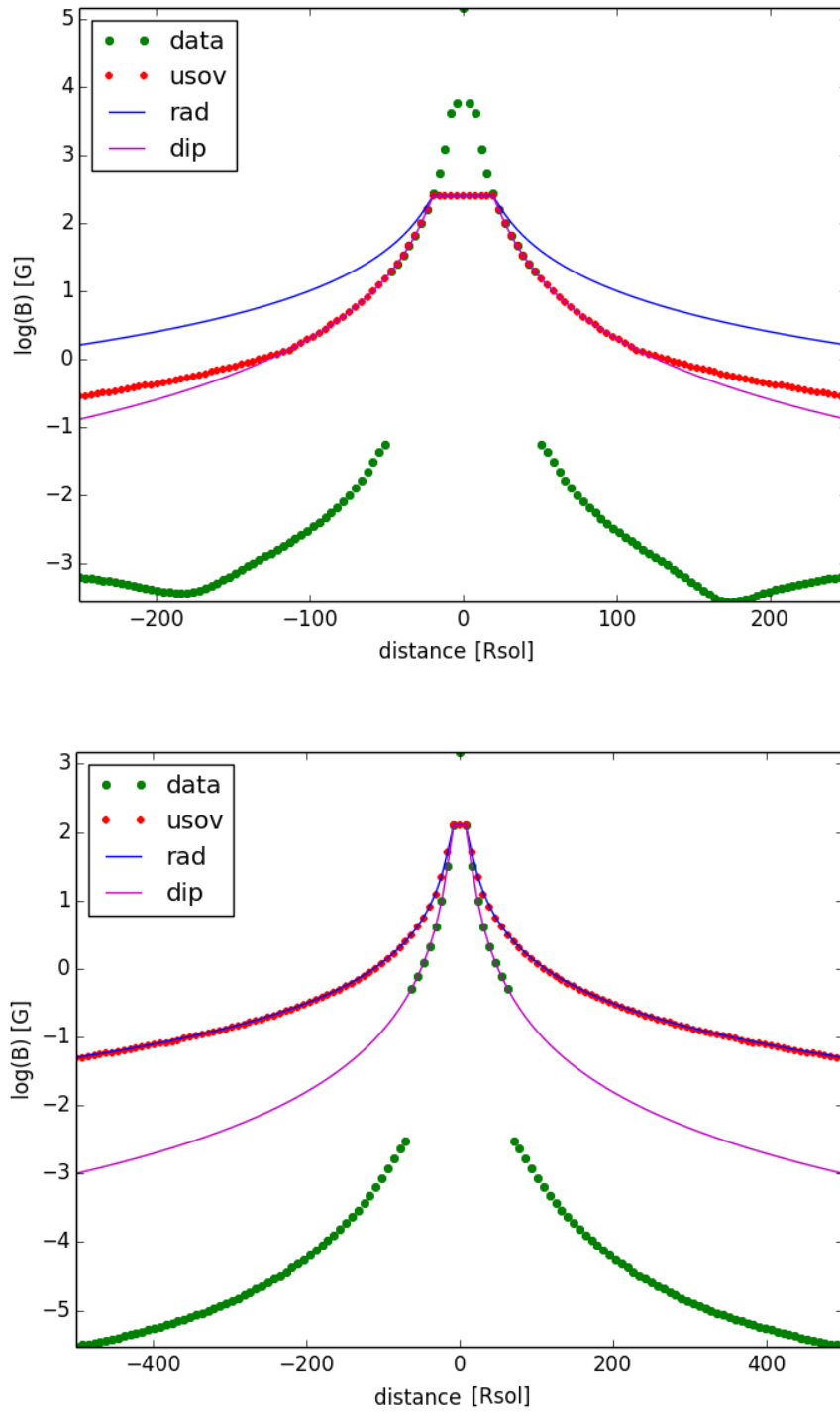


Figure 5.5: Same as Figure (5.4), but in the equatorial plane.

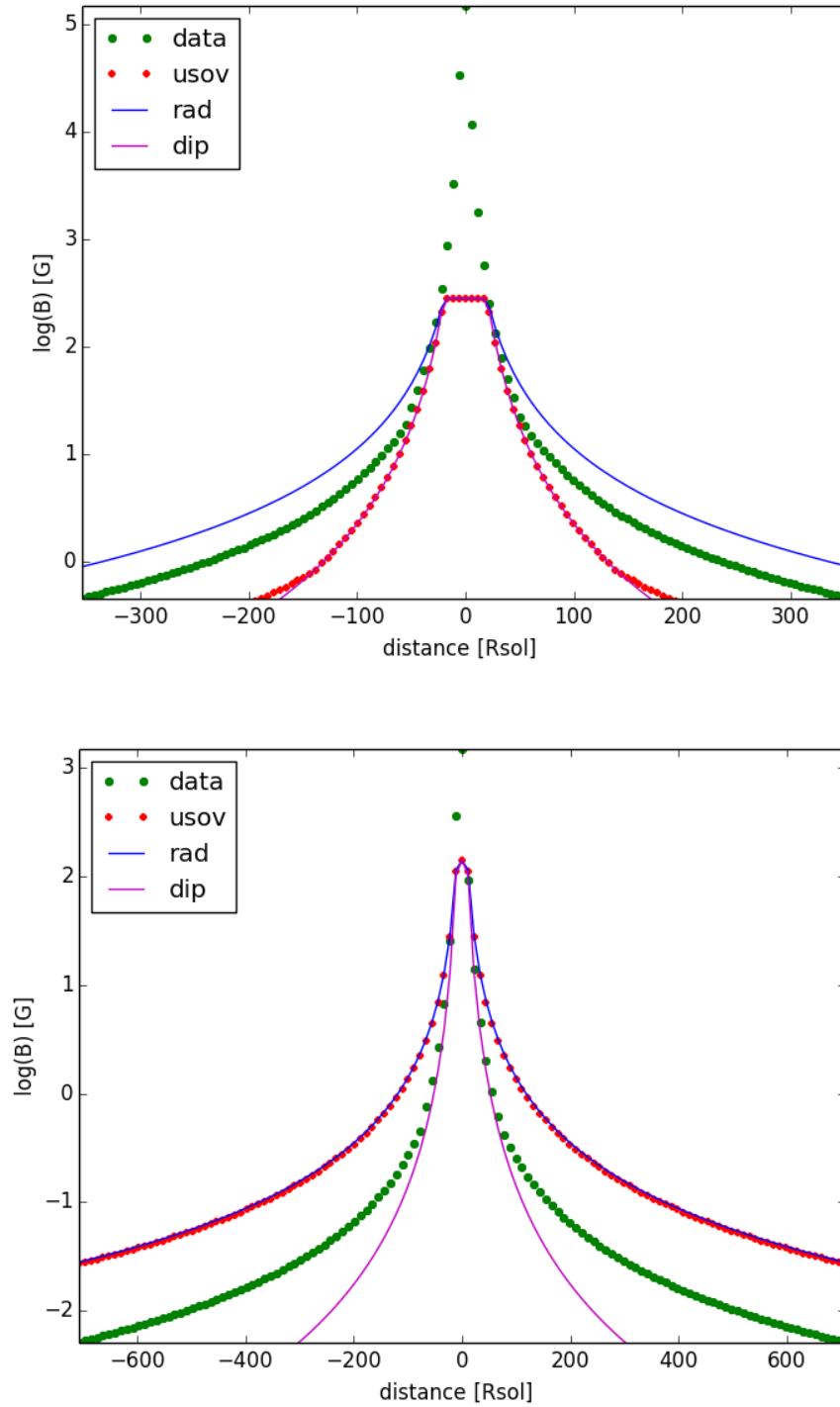


Figure 5.6: Same as Figure (5.5), but in the plane at the angle 45° between the polar and equatorial planes.

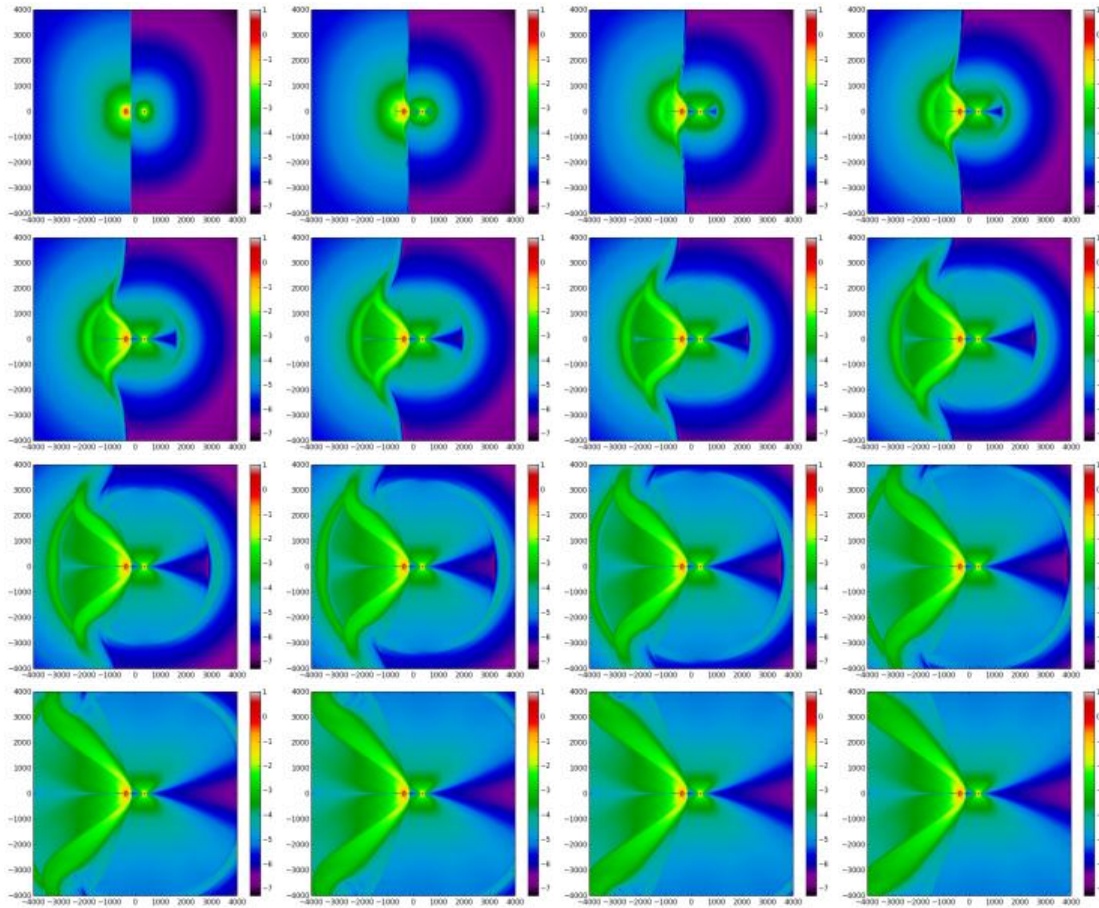


Figure 5.7: Evolution of the magnetic field strength during the formation of the wind collision region. The following timesteps are presented from left to right. Please note the logarithmic scale and the simulation units (cf. Table 4.1)

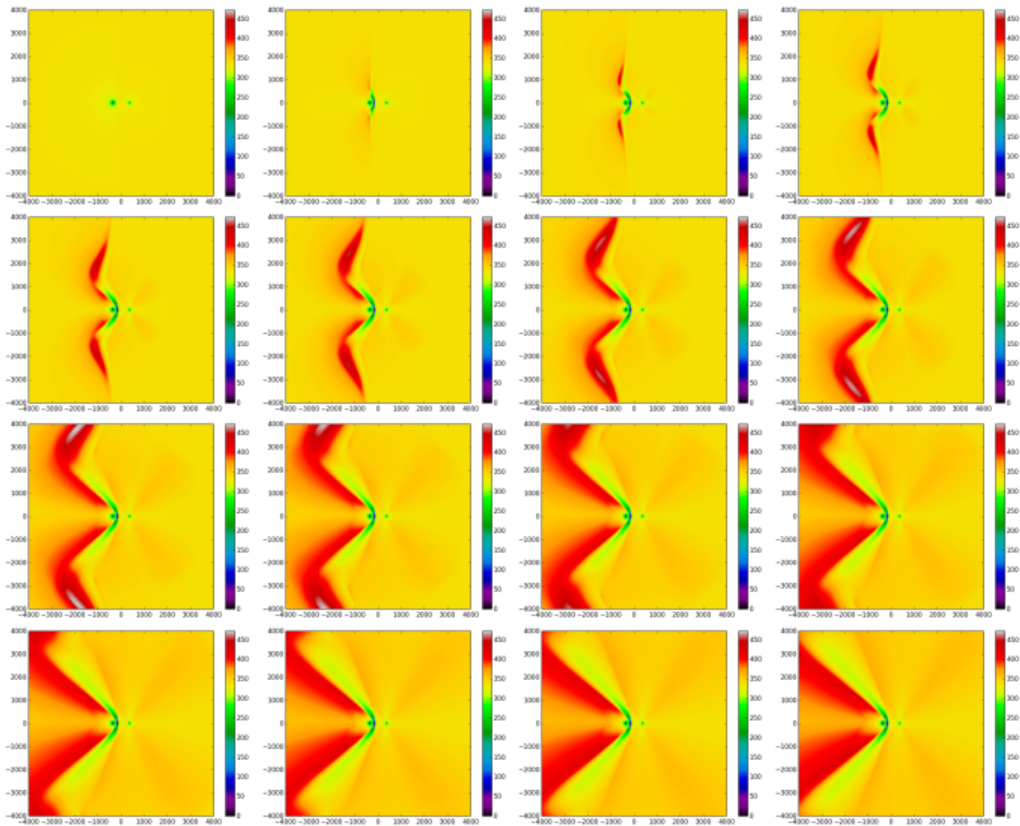


Figure 5.8: Evolution of the flow speed during creation of the wind collision region. The following timesteps are presented from left to right.

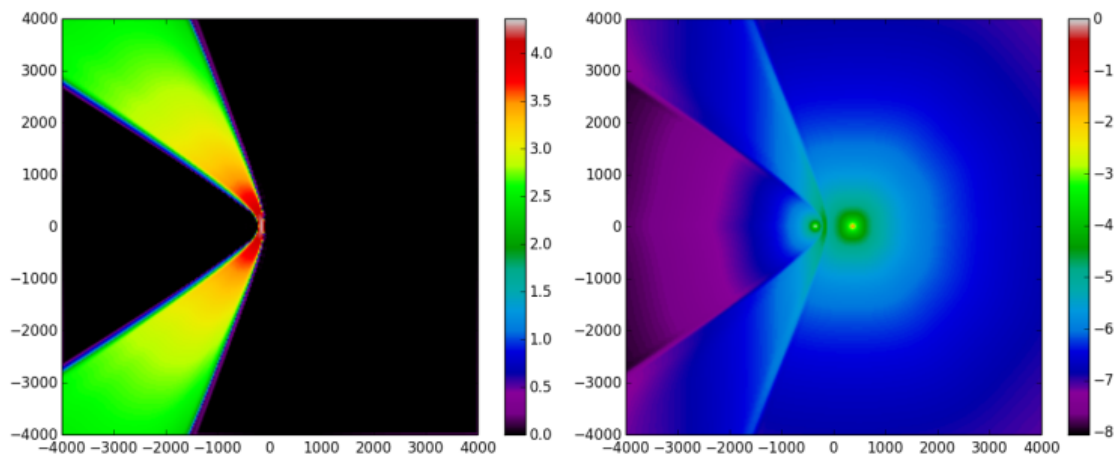


Figure 5.9: The converged state of a simulation. Left panel presents temperature, right panel - density. Both scales are logarithmic.

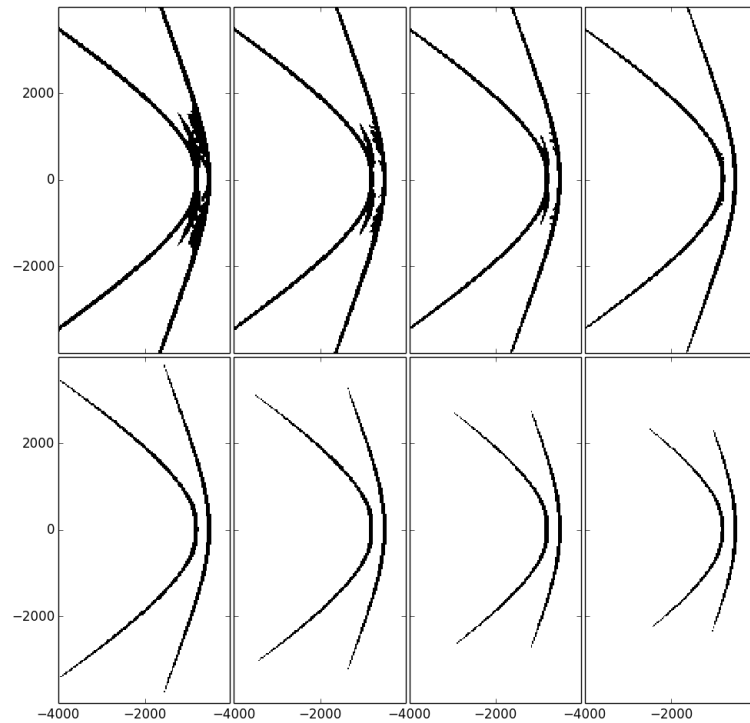


Figure 5.10: Figures present temperature gradient with cells above some arbitrary thresholds marked as black. This is used for obtaining suitable thresholds for shock identification. For the details of the selection procedure please refer to the text.

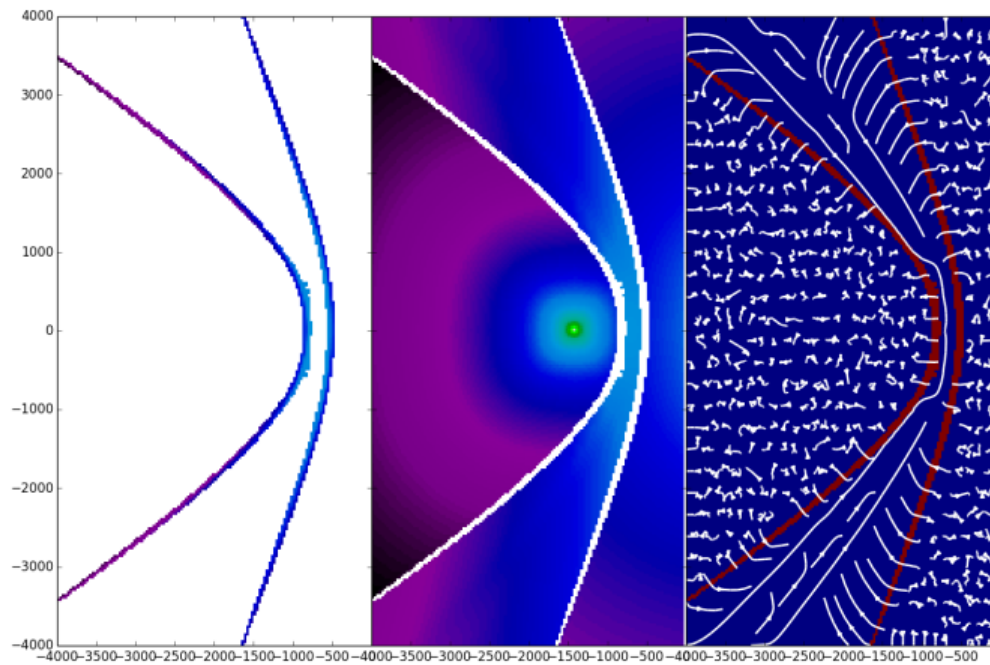


Figure 5.11: The middle panel presents density field without the cells establish as shocks. One can see that we indeed are able to identify clear borders between two physically different regions. On the left panel we present the transition in physical quantity (here: density) that takes place in-between. The right panel presents respective vector field of the temperature gradient.

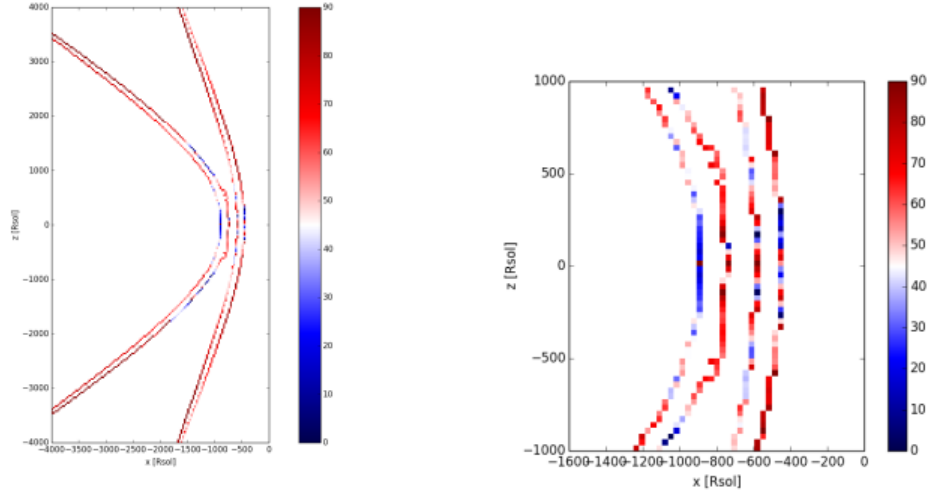


Figure 5.12: The angle θ_{Bn} between magnetic field and shock normal just outside of the shock. Red cells represent quasi-perpendicular shocks, blue - quasi-parallel. We see that the region with parallel magnetic field lies near the equatorial plane and, thus, the current sheet.

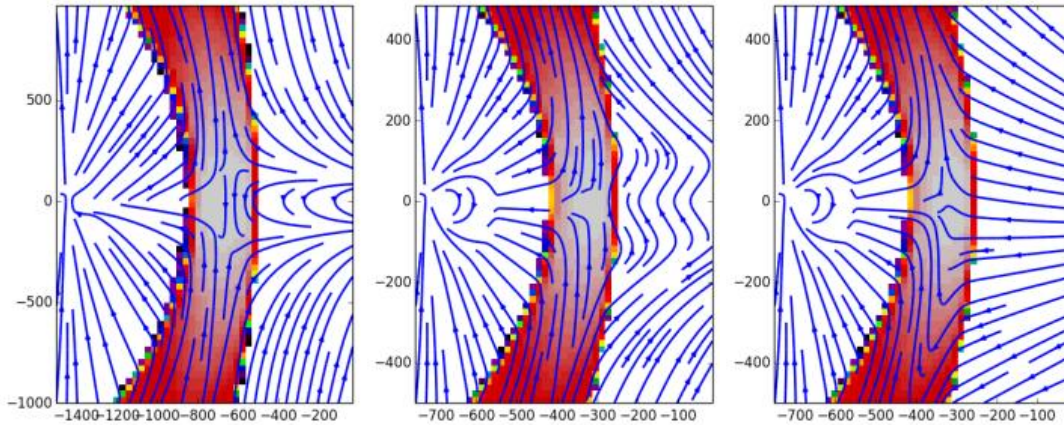


Figure 5.13: Magnetic field lines at the collision region. The left and middle panel show a model with both dipole moments oriented in the z -axis, but with different strength for the left star (middle panel shows the stronger field model). The right panel's right star has a dipole field with the magnetic moment lying on the x -axis. The background map is the temperature (log). Please refer to text for further discussion.

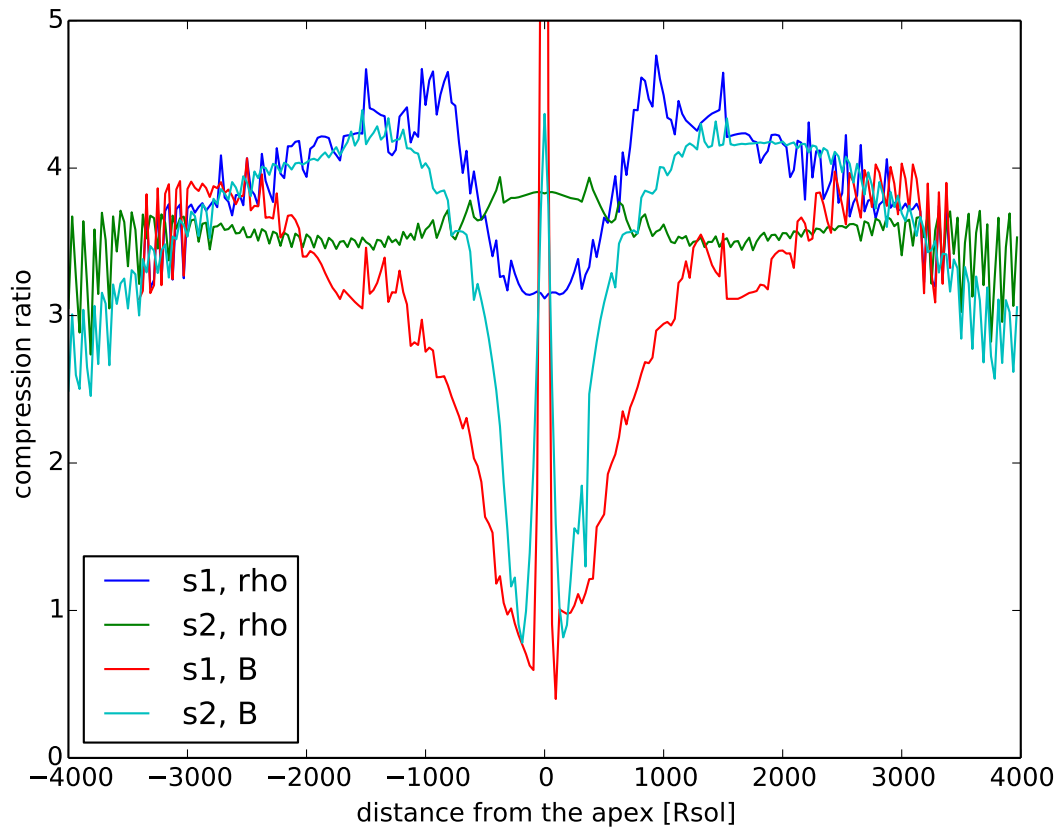


Figure 5.14: Compression ratios for density and magnetic field strengths for both shocks (S1, S2).

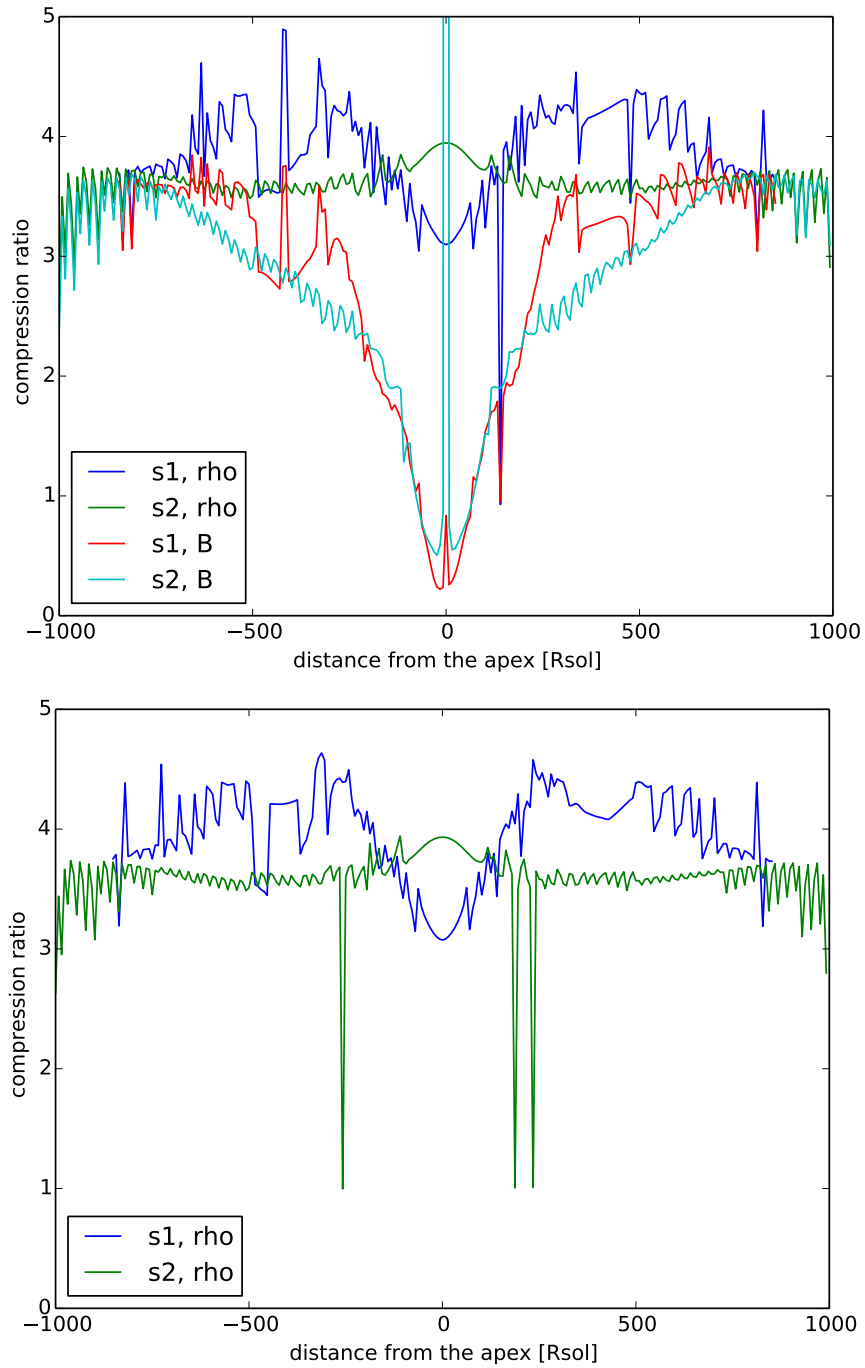


Figure 5.15: Comparison of compression ratios for the same numerical setup with magnetic field (upper figure) and without (bottom figure).

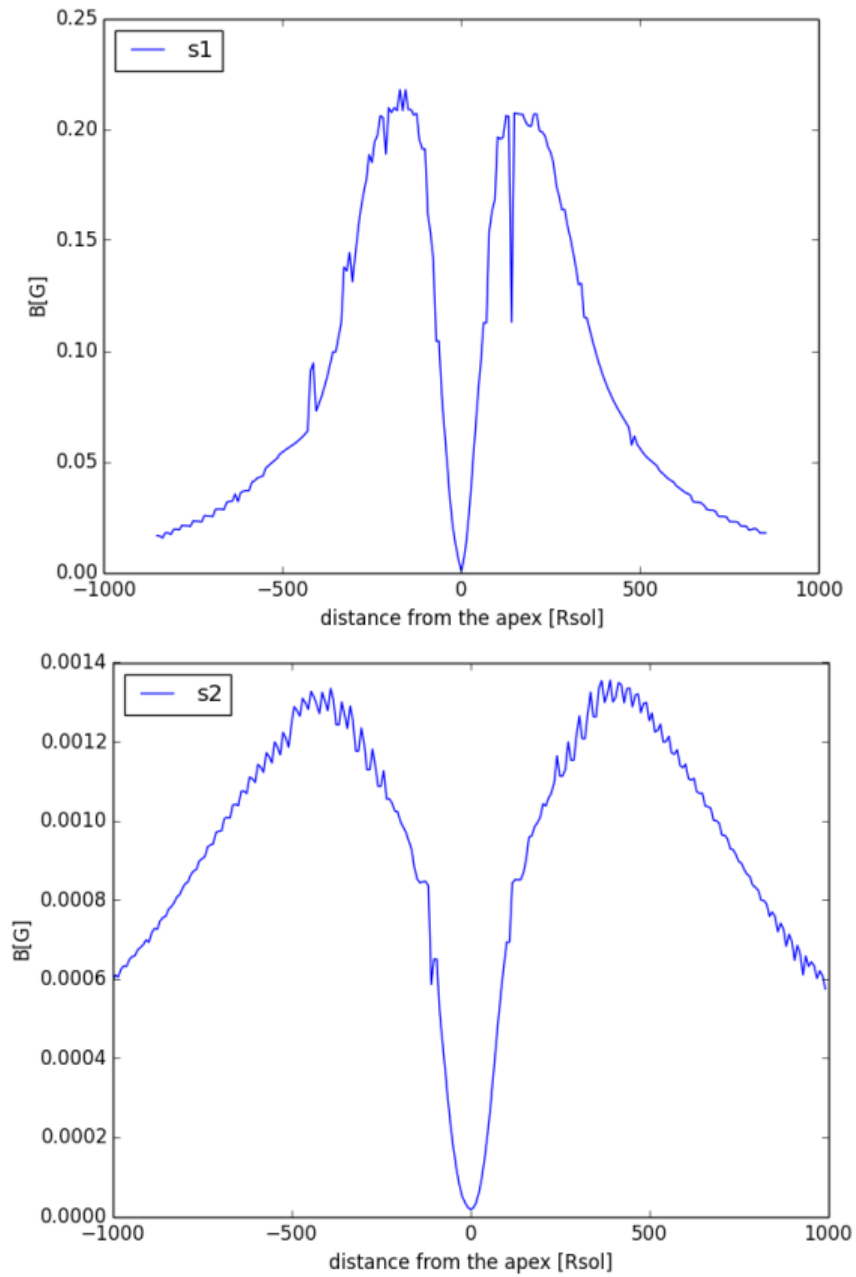


Figure 5.16: Magnetic field strength along the shock normal inside the collision for the S1 shock (upper panel) and the S2 shock (bottom panel).

Results - a parameter study

In the previous chapter we described our analysis techniques based on a single, exemplary simulation where we also illustrated the properties of the collision region that are in the focus of this study. In this chapter we discuss the variations of these properties over a range of parameters for either the magnetic fields' initial strengths or their geometries.

We have to note here that none of variations in the stellar magnetic field configurations have produced any changes in the temperature, density or velocity fields, since we investigate models with rather weak magnetic fields (which most systems probably have, as hinted by observations). For that reason the only maps and quantities we present here are those of the magnetic fields. We emphasize that this does not mean that the magnetic field has no effect at all over the shock structure or other physical quantities in the collision region. For instance we saw in section 5.1 that higher magnetic fields will confine the flow to the equatorial plane. This is also discussed later in section 6.3.

We note that we use the term star's magnetosphere as the region in space with a magnetic field that clearly originates in the star. We also acknowledge that fluctuations seen on shown magnetic field compression ratios, field strengths in the collision regions and angle distributions are caused by our method of calculation that uses the cell values and is therefore subjected to discretization errors.

6.1 Variation of the magnetic field strength

In this first study we investigate how the relative dipole strengths of the two stars change the properties of the magnetic field within the collision region. For this reason we employ a series of nine simulations that vary both stars' fields between 2G, 20G and 200G. We list details of the particular runs in Table 6.1.

The resulting fields are presented in Figure (6.1). We see that the domain is clearly divided by the two magnetospheres, which meet at the contact discontinuity within the collision region. This contact surface always forms at the same position. We conclude that there is no exchange

Table 6.1: Surface polar magnetic field strengths for particular runs. Note that they are arranged to reflect the layout of Fig. (6.1) for an easier comparison.

| Name | B_{pol}^B [G] | B_{pol}^{WR} [G] | Name | B_{pol}^B [G] | B_{pol}^{WR} [G] | Name | B_{pol}^B [G] | B_{pol}^{WR} [G] |
|------|-----------------|--------------------|------|-----------------|--------------------|------|-----------------|--------------------|
| o3 | 200 | 200 | o5 | 20 | 200 | o9 | 2 | 200 |
| o18 | 200 | 20 | o15 | 20 | 20 | o12 | 2 | 20 |
| o21 | 200 | 2 | o24 | 20 | 2 | o27 | 2 | 2 |

of information across the discontinuity. In other words, the two magnetospheres do not influence each other.

This lack of mutual influence is reflected in all the measured parameters. For instance, in Figure (6.2) we depict the magnetic field compression ratio for the whole series. In fact, the individual curves are indistinguishable, meaning that all the fields are equally enhanced at the shocks. A confirmation of this fact is seen in Figure (6.3). We see there three curves that correspond to three different dipole strengths. What is more, they follow linearly the scaling of these prescribed fields (so are exactly an order of magnitude different between each other). The maximal magnetic field strength amplification is ~ 1.8 . We see almost no amplification near the equatorial plane, where the current sheets penetrate the collision region.

A similar behavior is observed for the magnetic field strength (Figure (6.3)). It goes to zero near the equatorial plane. The region that is influenced by the current sheet is wider for the shock S2, since the center of the magnetosphere is further away and the affected region gets wider with the distance. The strength of the post-shock field of the S1 shock decreases much more quickly away from the collision region center than the one from the shock S2.

The distribution of the θ_{Bn} angles is also same for both shocks across all simulations, as seen in Figure (6.4). We see that this configuration produces only small quasi-parallel region for both shocks, located near the equatorial plane. Our simulations show that the size of this region does not depend on the prescribed dipole strength.

6.2 Variation of the field geometry

In the second series of simulations the polar strengths of both stars' fields are fixed to values of $B_{pol}^B=400\text{G}$ and $B_{pol}^{WR}=200\text{G}$. What we vary in this case is the geometry of the fields, by changing the angle θ between the z -direction in the xz plane and respective magnetic dipole moments. The

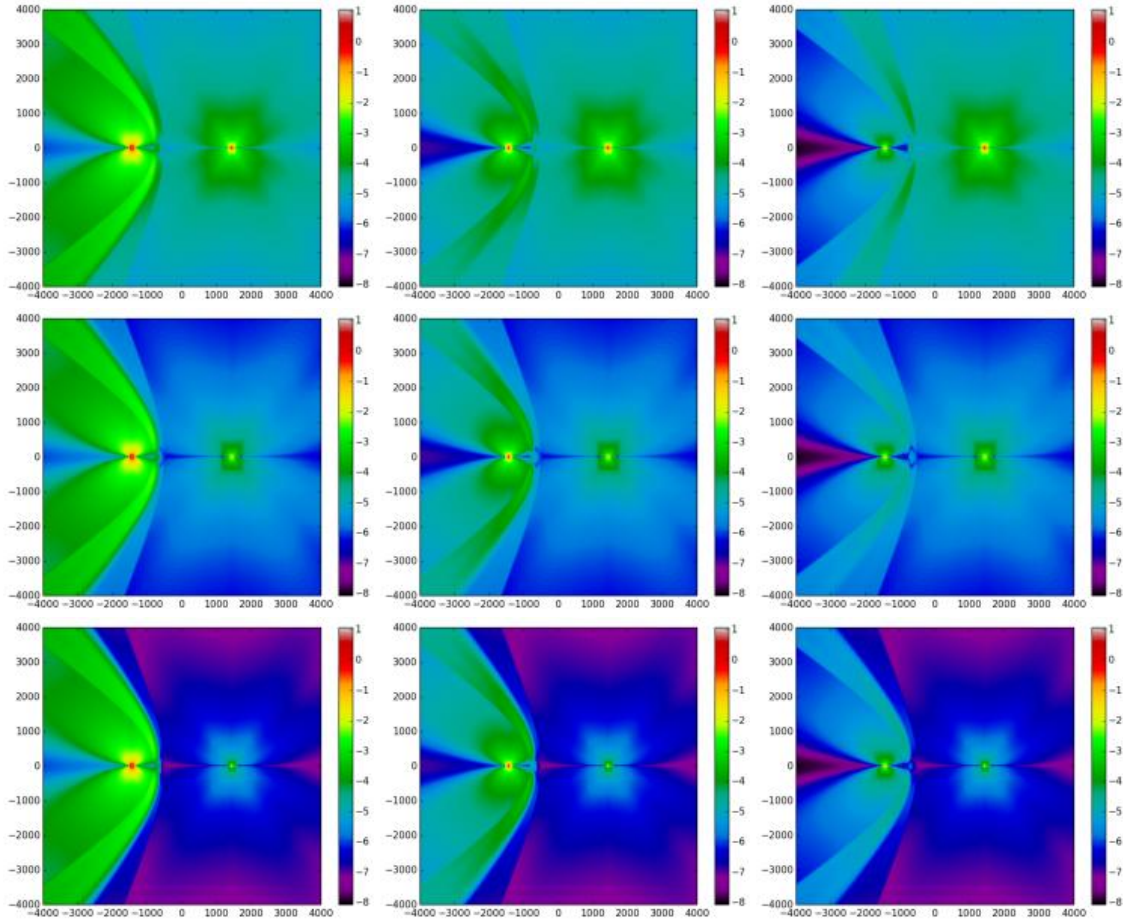


Figure 6.1: Magnetic field strengths for different runs. For respective simulation parameters refer to Table 6.1. Note that this is a logarithmic scale common to all plots to allow easier comparison.

specific setups are listed in Table 6.2. The first two setups are the "standard one" with the dipole moment oriented in the positive direction of the z -axis (m3), and the flipped dipole, where the dipole moment of the WR star is oriented in the negative z direction (m6). Then we examine two simulations in which only one of the stars is tilted, while the other one remains in the standard position (m9 and m12 for the tilted B-star and WR-star respectively). Finally, the last two runs present simulations where both of the star's dipoles are tilted. One is the "head on" setup, in which both dipoles lie in the x -axis directed towards the collision region (mm3). The last one shows both dipoles tilted, but still parallel with respect to each other (mm6).

The resulting fields are shown in Figure (6.5). We conclude that, as in the previous study, the

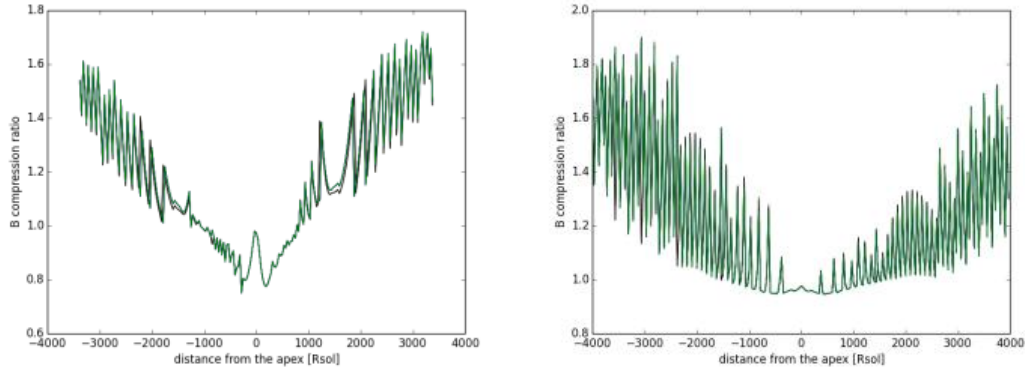


Figure 6.2: Magnetic field strength compression ratio for the S1 shock (left panel) and the S2 shock (right panel).

Table 6.2: The angle θ between the z -direction in the xz plane and respective magnetic dipole moments for particular runs. Note that they are arranged to reflect the layout of Fig. (6.5) for an easier comparison.

| Name | θ_B [°] | θ_{WR} [°] | Name | θ_B [°] | θ_{WR} [°] |
|------|----------------|-------------------|------|----------------|-------------------|
| m3 | 0 | 0 | m6 | 0 | 180 |
| m9 | 30 | 0 | m12 | 330 | 0 |
| mm3 | 90 | 270 | mm6 | 45 | 315 |

magnetospheres do not influence each other. As expected, the oppositely orientated dipoles (simulation m2, upper right panel in Figure (6.5)), create a current sheet at the contact discontinuity. Apparently in all cases of tilted dipoles the magnetic field strength structure in the collision region becomes very non-trivial. For instance we see regions, on respective sides of the contact discontinuity, that have pulled in features of the original field's geometry. It follows that even the region dominated by one of the stars cannot be easily described by one magnetic field strength value or a simple function.

In Figure (6.6) we present the post-shock magnetic field strengths. The m3 and m6 runs follow the well-known behavior of the previous series, and are in practice indistinguishable. In the case of m9 and m12, the untilted component has the same properties as found before. In the runs, where the field was tilted by some angle smaller than 90° (m9, m12 and mm6) we see a global

maximum, and a local minimum that occurs where the current sheet hits the shock, though it does not bring down the field's strength to zero like we observe it to do when it hits the apex. For the 'head on' case, we see a small minimum in the magnetic field strength near the equatorial plane. We believe this to be a numerical effect caused by prescribing the initial dipole on a discrete grid and extrapolating it in the star's center.

The distributions of angles θ_{Bn} , depicted in Figure (6.7), reveals a variety of different behaviors for both shocks in the different runs. We now have many different regions of the quasi-parallel and the quasi-perpendicular regimes. As with the magnetic field strength, all cases where the dipole moment is in the z -axis behave the same. One interesting case is the 'head on' setup, where the dipole moments lie in the x -axis, shown in Figure (6.8). The S1 shock quasi-parallel region is much wider than in the 'standard' case, and it has a very clear transition to the quasi perpendicular regime, that happens when the current-sheet hits the shock. The S2 shock is always quasi-parallel, which can be understood since the WR star's current sheet never reaches the collision region.

6.3 High magnetic fields

All simulations up to now had the highest polar fields of about 200-400G. We have also performed a series with significantly higher magnetic fields in the B star ($B_{pol} = 2800\text{G}$). These, however, were contaminated with the artificial heating that we have discussed before, and therefore cannot be fully trusted and are not further analyzed. Nevertheless, we present here the results of the 'standard' setup with the magnetic dipole parallel to the z -axis and one with a tilted setup.

Figure 6.9 shows the comparison for the magnetic field strength and the density. Firstly, we see that the much stronger magnetosphere of the B-star now dominates the collision region and extends over the contact discontinuity (the position of the contact discontinuity is clearly visible in the density profiles). This means that the stronger magnetosphere is able to actually interact with the other star's wind. However, it is uncertain if this is an actual, physical effect. Furthermore we see higher density near the equatorial plane as well as small structures in the magnetic field strength close to the star, resembling our results for a single, highly magnetized star (section 5.1). The denser regions near the equatorial plane have also higher velocities as the ones seen in Figure (6.10).

Looking at the tilted dipole simulation, we can guess that the denser and faster than the overall wind outflow, which is collimated in the star's equatorial plane, is responsible for actually bending the collision region (as it pushes it further out with respect to the "standard" position). This can happen, because the equatorial outflow will have a higher momentum flux, and as we discussed in section 3.1, the momentum flux ratio decides about the position of the collision region. Then,

it is not the magnetic field directly that changes the geometry of the collision region, but rather its influence on the wind properties (as it becomes not spherical anymore). We see in the velocity profiles that the wind is accelerated everywhere apart from the regions parallel to the magnetic dipole moment. Comparison with the temperature maps suggests that this acceleration might be in fact caused by the additional thermal pressure caused by the artificial heating.

These results, however unreliable, hint that further exploration of the parameter space, especially higher magnetic fields, should yield more interesting results and ways in which the magnetic field can change the collision region's properties. As we discussed in section 2.2.1, less than 10% of massive stars exhibit such strong fields. This hints that such extreme systems, if they exist, are not common.

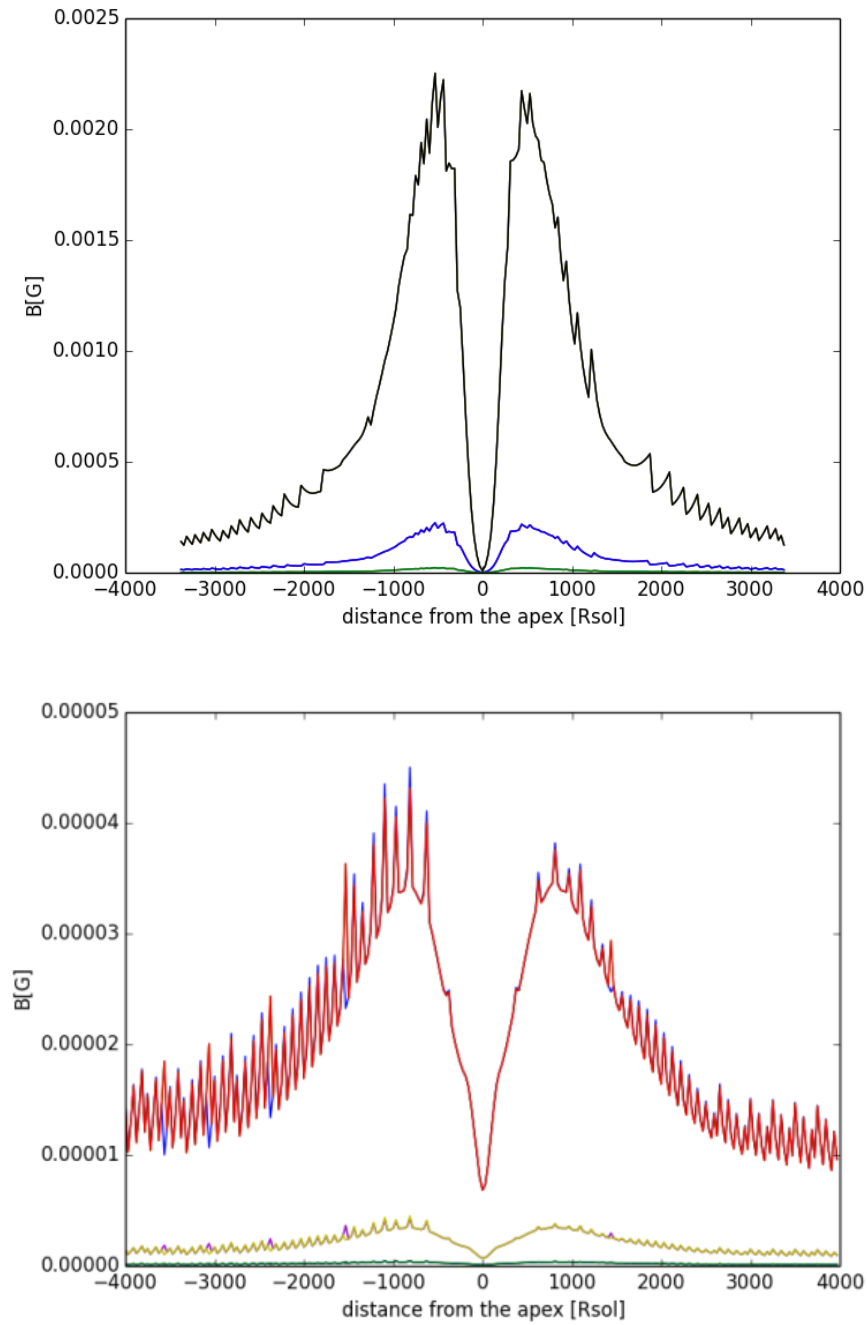


Figure 6.3: Post-shock magnetic field strengths for the S1 shock (upper panel) and the S2 shock (bottom panel) for the simulations with varying magnetic field strengths.

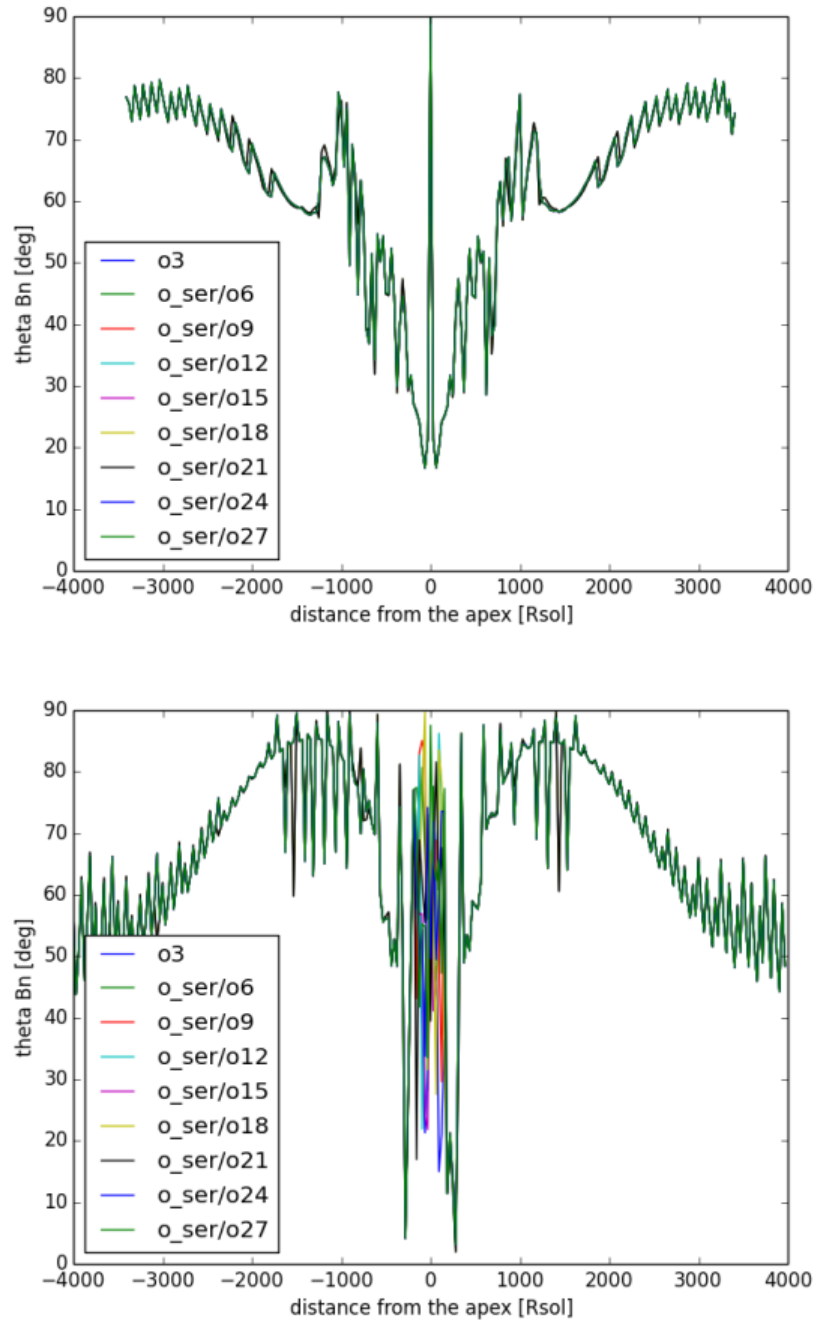


Figure 6.4: The upstream θ_{Bn} angle for the S1 shock (upper panel) and the S2 shock (bottom panel).

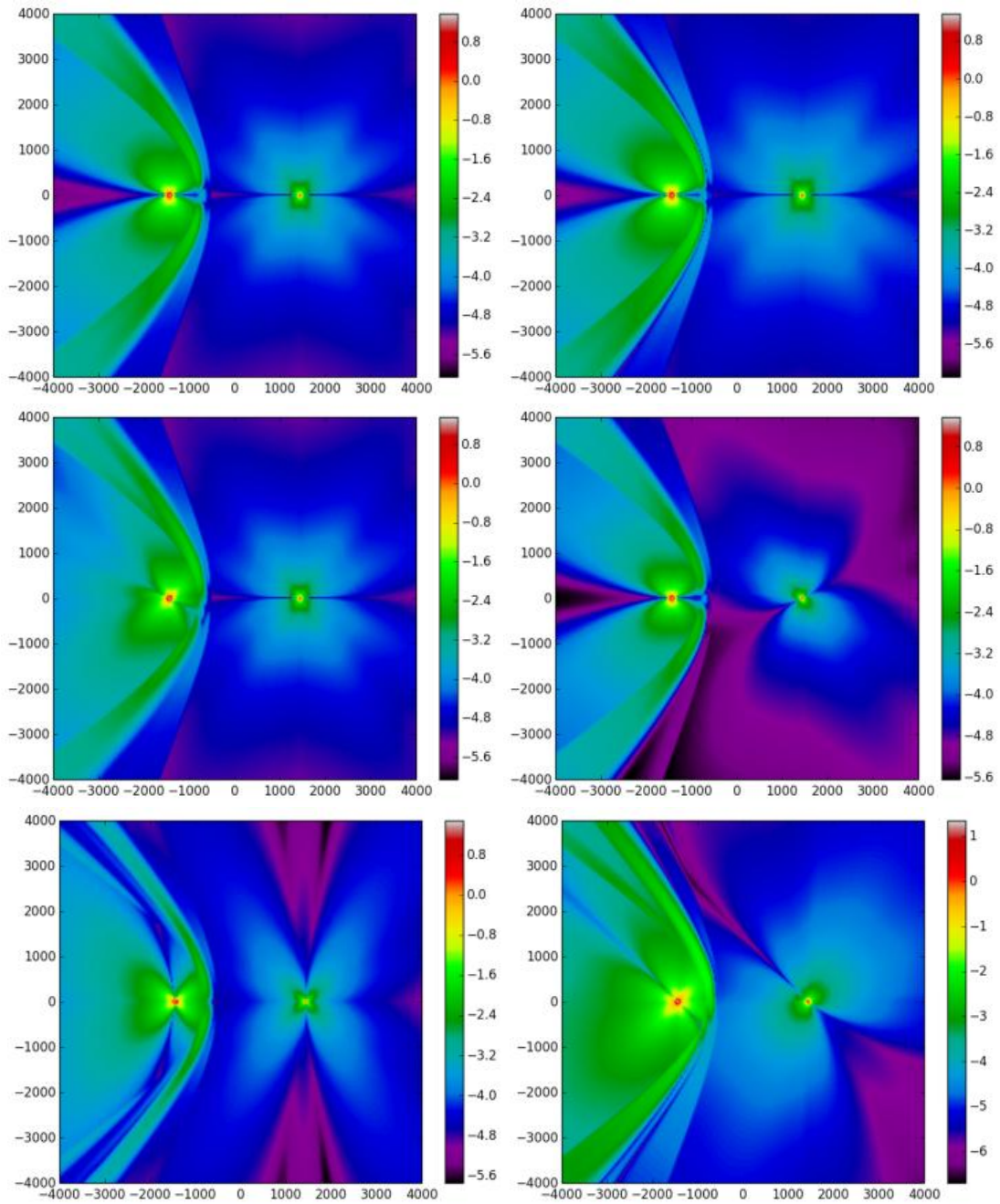


Figure 6.5: Magnetic field strengths for different runs. For respective simulation parameters refer to Table 6.2.

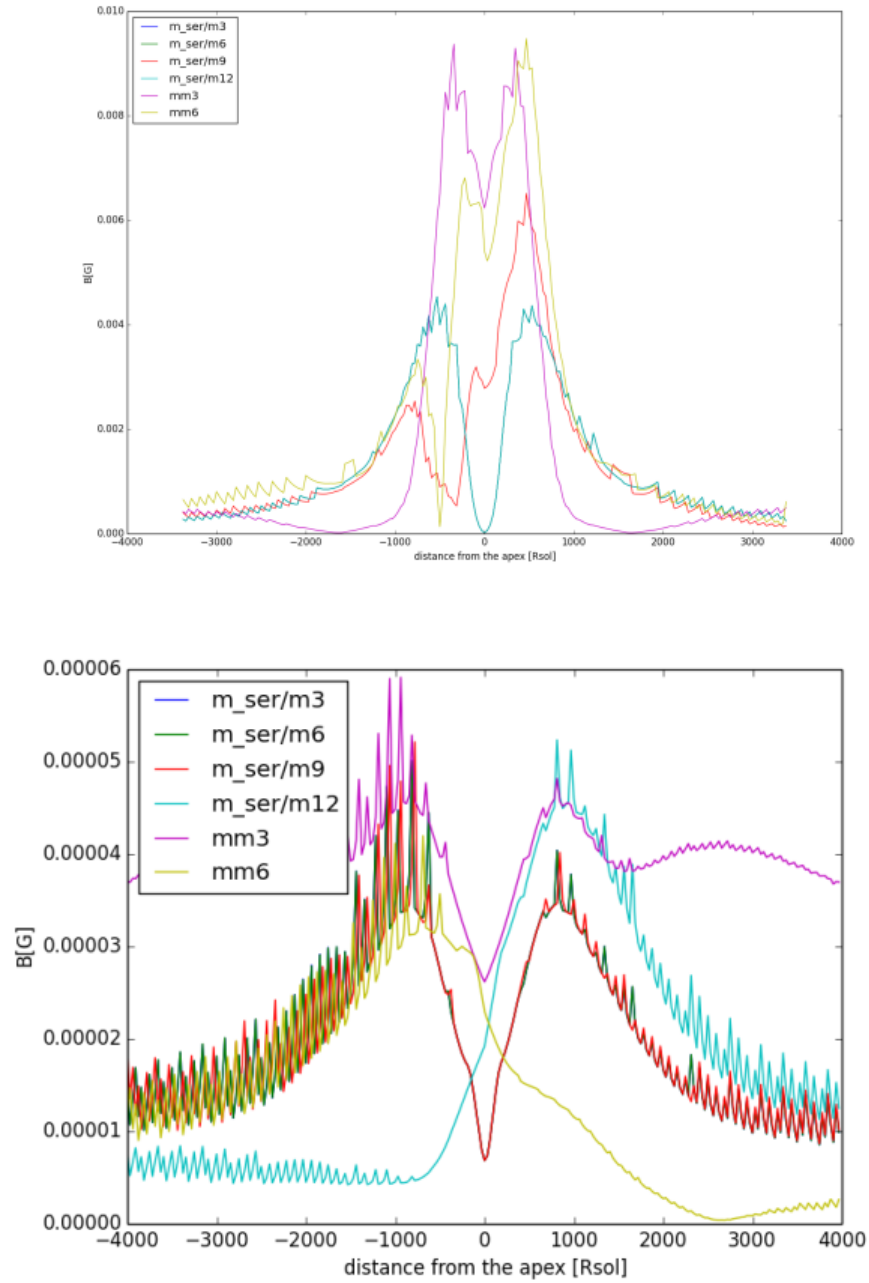


Figure 6.6: Post-shock magnetic field strengths for the S1 shock (upper panel) and the S2 shock (bottom panel).

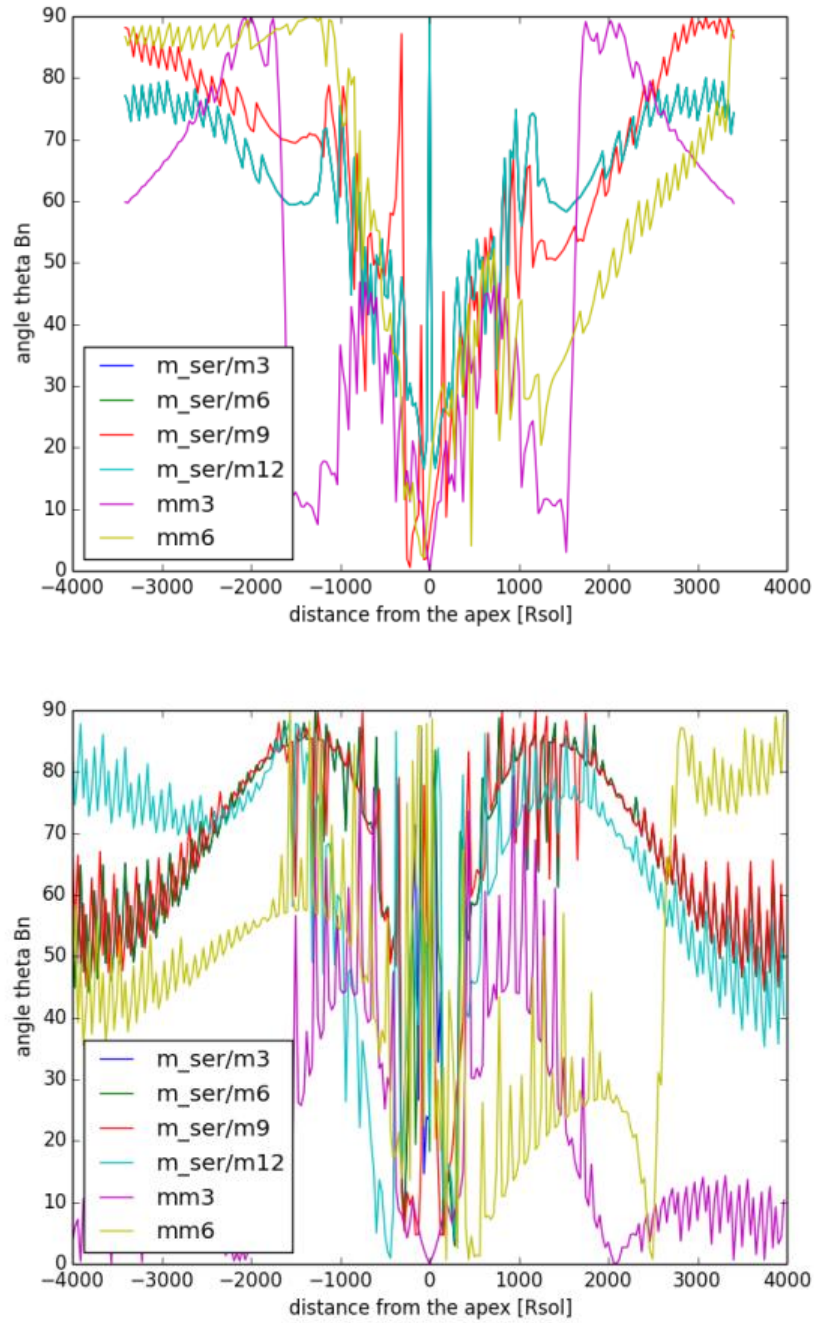


Figure 6.7: The upstream θ_{Bn} angle for the S1 shock (upper panel) and the S2 shock (bottom panel).

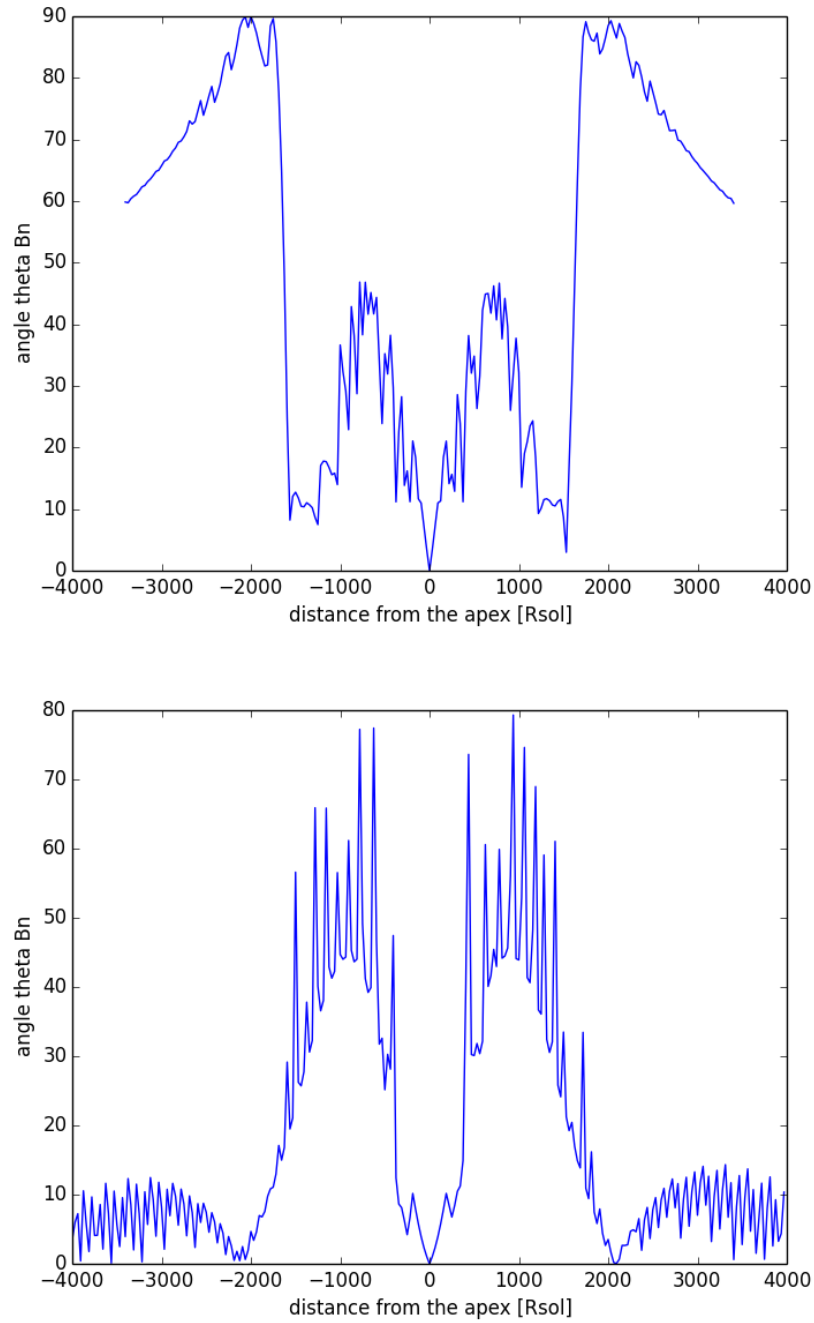


Figure 6.8: The upstream θ_{Bn} angle for the S1 shock (upper panel) and the S2 shock (bottom panel) for the 'head on' simulation (mm3).

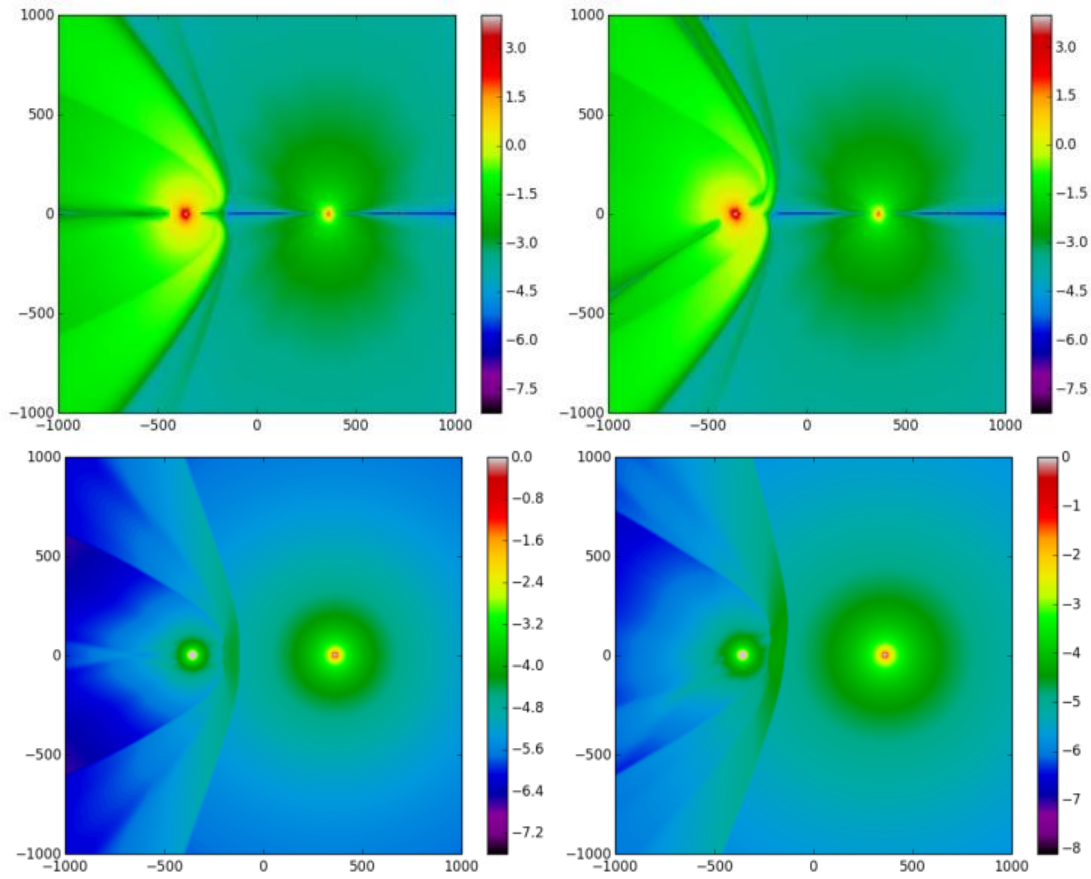


Figure 6.9: Comparison of the magnetic field strength (upper panels) and the density profiles (bottom panels) for two runs with high magnetic fields.

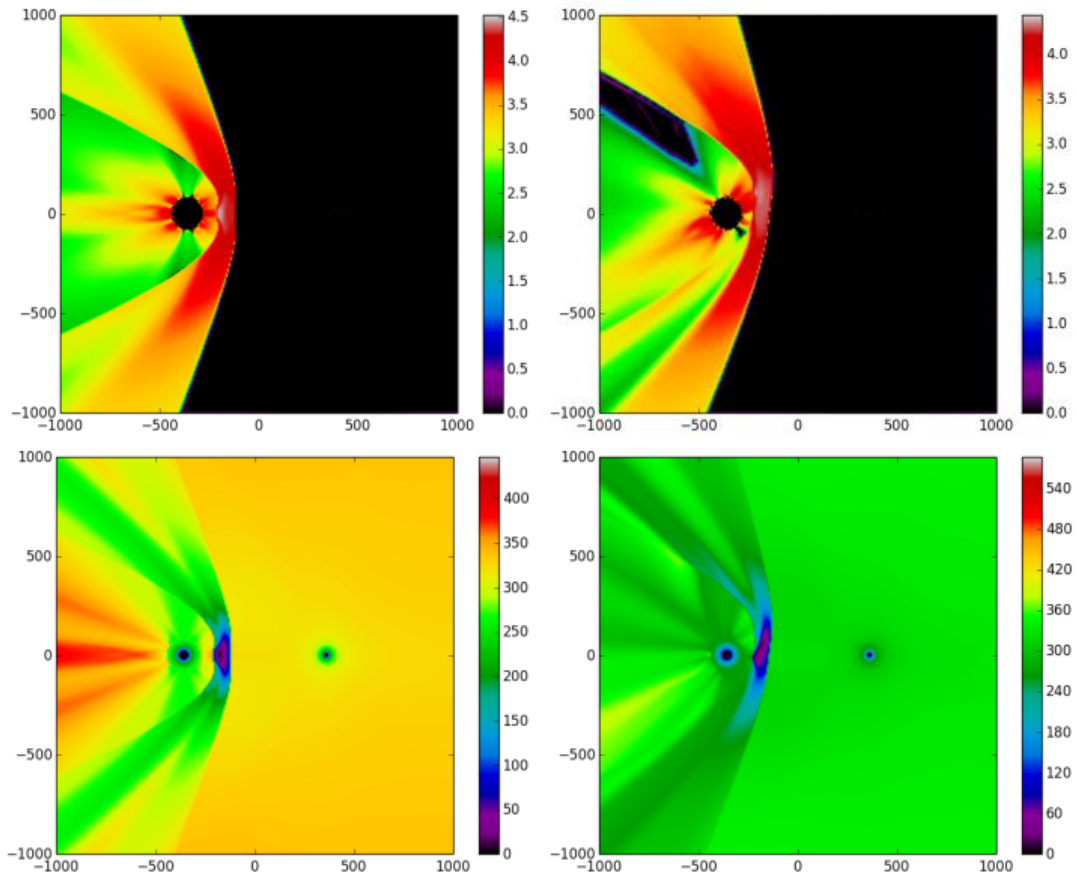


Figure 6.10: Comparison of the temperature (upper panels) and velocity profiles (lower panels) for two runs with high magnetic fields.

Conclusions

In this work we have studied magnetic field properties in the wind collision region of the binary systems of massive stars with strong stellar winds. We have focused our efforts on studying magnetic field strength in the collision region and its orientation at the shock surfaces, since these quantities influence high energy phenomena such as the non-thermal radiation and particle acceleration. We have identified some general trends for the the magnetic field strength and its structure in the collision region.

We study fields of the order of $\sim 100\text{G}$, which are realistic values for most massive stars. In this regime we conclude the following:

- Prescribed magnetic fields did not change the overall properties of the collision region, such as its geometry and compression ratio.
- The magnetospheres do not influence each other and stay on their respective sides of the contact discontinuity. This might not be the case for stronger fields, which could be able to cross the contact discontinuity and interact with the other star's wind.
- For dipole fields oriented perpendicular to the orbital separation there is only a small area near to the collision region's apex, where the shocks are quasi-parallel. This region does not depend on the field's strength, but does only change when we tilt the dipole magnetic moment.
- In the case of dipole fields that are oriented parallel to the system's orbital separation, the whole outer shock (S2) is quasi-parallel, while the inner one (S1) is quasi-parallel near the apex and then undergoes a clear transition into a quasi-perpendicular regime where the current sheet of the star hits the collision region.
- For the 'standard' case of the perpendicular (to the orbital separation) dipole moment we see a clear difference of magnetic field strengths on the opposite sides of the contact discontinuity, that are proportional to star's dipole strength. This means for instance, that more detailed simulations of non-thermal radiation should take this effect into account.

- For the case of tilted dipoles, the magnetic field strength has a complicated structure and changes by the orders of magnitude even within the same magnetosphere.
- Following both isothermal simulations of a single, magnetized star and attempted simulations for stronger magnetic fields, we conclude that such fields can influence the properties of the collision region. For instance, highly magnetized star will not produce a fully spherical outflow, changing the pressure ratio in space and therefore changing the geometry of the collision region.

One of the main results of our study is that the most influential factor over the properties of the magnetic field in the collision region is the orientation of the initial dipole fields. We also determine that using one common magnetic field strength for the whole collision region might be erroneous if the fields of both stars differ greatly.

7.1 Future work

This study is not yet complete and there is a number of improvements and further parameters to be studied. Due to our current numerical capabilities, and more importantly, time constraints of a master's thesis, we were not able to stretch out the studied parameter space to high values of magnetic field strengths. Rotation of stars can change the geometry of the magnetic field and influence the overall wind properties, which will change the properties of the collision region. Thus its role could also be studied with simulations. Then one could also incorporate the orbital motion of the stars, bringing the simulations closer to the real systems.

Acknowledgments

Firstly, I would like to thank my supervisor, Ralf Kissmann, for his brilliant guidance, patience and understanding, and most importantly for encouraging me to learn so much in a short amount of time. I also extend my gratitude to the whole Astro- particle group for providing me with a warm and creative environment here in Innsbruck. In particular I would like to thank Josef Schafer for the kind help he has given me and for making my life much easier.

Above all I thank my dear Parents for their unconditional support and understanding.

I dedicate this work to those, who still look up in perfect silence at the stars, however far they might be.

Bibliography

- Abbott, D. C., Biegging, J. H., & Churchwell, E. 1984, *ApJ*, 280, 671
- Aurière, M., Wade, G. A., Silvester, J., et al. 2007, *A&A*, 475, 1053
- Biermann, L., Brosowski, B., & Schmidt, H. U. 1967, *SolPhys*, 1, 254
- Blandford, R. D., & Ostriker, J. P. 1978, *ApJ*, 221, L29
- Carroll, B. W., & Ostlie, D. A. 1996, *An Introduction to Modern Astrophysics*
- Castor, J. I., Abbott, D. C., & Klein, R. I. 1975, *ApJ*, 195, 157
- De Becker, M., & Raucq, F. 2013, *A&A*, 558, A28
- de la Chevrotière, A., St-Louis, N., Moffat, A. F. J., & the MiMeS Collaboration. 2014, *ApJ*, 781, 73
- Donati, J.-F., & Landstreet, J. D. 2009, *ARA&A*, 47, 333
- Dougherty, S. M. 2010, in *Astronomical Society of the Pacific Conference Series*, Vol. 422, *High Energy Phenomena in Massive Stars*, ed. J. Martí, P. L. Luque-Escamilla, & J. A. Combi, 166
- Dougherty, S. M., Beasley, A. J., Claussen, M. J., Zauderer, B. A., & Bolingbroke, N. J. 2005, *ApJ*, 623, 447
- Dougherty, S. M., & Williams, P. M. 2000, *MNRAS*, 319, 1005
- Eichler, D., & Usov, V. 1993, *ApJ*, 402, 271
- Ellison, D. C., Baring, M. G., & Jones, F. C. 1995, *ApJ*, 453, 873
- Grunhut, J. H., & Wade, G. A. 2013, in *EAS Publications Series*, Vol. 64, *EAS Publications Series*, 67–74
- Grunhut, J. H., Wade, G. A., Leutenegger, M., et al. 2013, *MNRAS*, 428, 1686
- Hunter, J. D. 2007, *Computing In Science & Engineering*, 9, 90
- Kissmann, R., Kleimann, J., Fichtner, H., & Grauer, R. 2008, *MNRAS*, 391, 1577

- Kleimann, J., Kopp, A., Fichtner, H., & Grauer, R. 2009, *Annales Geophysicae*, 27, 989
- Lamers, H. J. G. L. M., & Cassinelli, J. P. 1999, *Introduction to Stellar Winds*
- Low, B. C., & Tsinganos, K. 1986, *ApJ*, 302, 163
- Moss, D. 2001, in *Astronomical Society of the Pacific Conference Series*, Vol. 248, *Magnetic Fields Across the Hertzsprung-Russell Diagram*, ed. G. Mathys, S. K. Solanki, & D. T. Wickramasinghe, 305
- Ostrowski, M. 1988, *MNRAS*, 233, 257
- Parker, E. N. 1958, *ApJ*, 128, 664
- Parkin, E. R., & Gosset, E. 2011, *A&A*, 530, A119
- Petit, V., Owocki, S. P., Wade, G. A., et al. 2013, *MNRAS*, 429, 398
- Pittard, J. M. 2009, *MNRAS*, 396, 1743
- Pittard, J. M., & Dougherty, S. M. 2006, *MNRAS*, 372, 801
- Pittard, J. M., & Parkin, E. R. 2010, *MNRAS*, 403, 1657
- Pomoell, J., Vainio, R., & Kissmann, R. 2011, *Astrophysics and Space Sciences Transactions*, 7, 387
- Prölss, G. W., & Bird, M. K. 2004, *Physics of the Earth's Space Environment: an introduction* (Springer-Verlag Berlin Heidelberg)
- Reitberger, K., Kissmann, R., Reimer, A., & Reimer, O. 2014a, *ApJ*, 789, 87
- Reitberger, K., Kissmann, R., Reimer, A., Reimer, O., & Dubus, G. 2014b, *ApJ*, 782, 96
- Sandroos, A., & Vainio, R. 2006, *A&A*, 455, 685
- Schure, K. M., Kosenko, D., Kaastra, J. S., Keppens, R., & Vink, J. 2009, *A&A*, 508, 751
- Stevens, I. R., Blondin, J. M., & Pollock, A. M. T. 1992, *ApJ*, 386, 265
- Ud-Doula, A., & Owocki, S. P. 2002, *ApJ*, 576, 413
- Ud-Doula, A., Owocki, S. P., & Townsend, R. H. D. 2008, *MNRAS*, 385, 97

ud-Doula, A., Sundqvist, J. O., Owocki, S. P., Petit, V., & Townsend, R. H. D. 2013, *MNRAS*, 428, 2723

Usov, V. V., & Melrose, D. B. 1992, *ApJ*, 395, 575

van der Hucht, K. A., Williams, P. M., Spoelstra, T. A. T., & de Bruyn, A. G. 1992, in *Astronomical Society of the Pacific Conference Series*, Vol. 22, *Nonisotropic and Variable Outflows from Stars*, ed. L. Drissen, C. Leitherer, & A. Nota, 253–268

Weber, E. J., & Davis, Jr., L. 1967, *ApJ*, 148, 217

Williams, P. M., Dougherty, S. M., Davis, R. J., et al. 1997, *MNRAS*, 289, 10

Williams, P. M., van der Hucht, K. A., Pollock, A. M. T., et al. 1990, *MNRAS*, 243, 662